Michael Mayrhofer-Reinhartshuber

Surface Structure and Dynamics of Bi(111) and Sb(111) from Helium Atom Scattering Experiments

DOCTORAL THESIS

for obtaining the academic degree
Doktor der technischen Wissenschaften

Doctoral Programme of Technical Sciences
Technical Physics

Graz University of Technology

Supervisor:
Univ.-Prof. Mag. Dr.rer.nat Wolfgang E. Ernst
Institute of Experimental Physics

Graz, December 2013

Deutsche Fassung:
Beschluss der Curricula-Kommission für Bachelor-, Master- und Diplomstudien vom 10.11.2008
Genehmigung des Senates am 1.12.2008

EIDESSTATTLICHE ERKLÄRUNG

Ich erkläre an Eides statt, dass ich die vorliegende Arbeit selbstständig verfasst, andere als die angegebenen Quellen/Hilfsmittel nicht benutzt, und die den benutzten Quellen wörtlich und inhaltlich entnommene Stellen als solche kenntlich gemacht habe.

Graz, am ……. ……..
(Unterschrift)

Englische Fassung:

STATUTORY DECLARATION

I declare that I have authored this thesis independently, that I have not used other than the declared sources / resources, and that I have explicitly marked all material which has been quoted either literally or by content from the used sources.

……. ……..
date (signature)

Abstract

Surface Structure and Dynamics of Bi(111) and Sb(111) from Helium Atom Scattering Experiments

HAS measurements were performed to investigate the (111)-surfaces of the semimetals bismuth (Bi) and antimony (Sb) with regard to their potential energy surface and their surface dynamics. For both Bi(111) and Sb(111), angular scans show sharp diffraction peaks up to third order, which match well with the predicted positions calculated from the already known surface structure. Intensity measurements of the specular peak as a function of incident energy were analysed to determine the distribution of terraces on the surfaces. The results show quite flat Bi(111) and Sb(111) surfaces and step heights consistent with the heights of bilayers obtained from recent calculations.

The electronic surface corrugation, which is the electron distribution slightly above the surface, was derived by a comparison of the experimental results with theoretical approaches, namely the GR-method and close-coupling (CC) calculations. Best fit results were obtained with peak-to-peak corrugation heights of 10% for Bi(111) and 13% (GR) to 17% (CC) for Sb(111), each value with respect to the corresponding lattice constant. These corrugations are rather large compared to other surfaces with metallic character and may be caused by specific electronic states of the surfaces, e.g. electron pockets at the Fermi level.

The analysis of selective adsorption resonance features, which are located between the purely elastic diffraction peaks, led to three (Bi) and five (Sb) bound-state energies. Based on the energies of these states, helium-surface interaction potentials with well depths of (8.3 ± 0.8) meV (Bi), respectively (4.4 ± 0.1) meV (Sb) were determined.

The vibrational dynamics were investigated by measurements of the Debye-Waller attenuation of the elastic diffraction peaks while varying the surface temperature between 98 and 447 K. Therewith, surface Debye temperatures of (84 ± 8) K (Bi) and (155 ± 3) K (Sb) were determined. In HAS measurements from Sb(111), occurring kinematic focusing effects were in good agreement with surface phonon dispersion curves from already published DFPT calculations.

Kurzfassung

Struktur und Dynamik der Bi(111) and Sb(111) Oberflächen aus Helium-Atom-Streu-Experimenten

Zur Charakterisierung von Struktur und Dynamik der (111)-Oberflächen der Halbmetalle Bismut (Bi) und Antimon (Sb) wurden Streuexperimente mit Helium (He) Atomen durchgeführt. Aus den scharf zuordenbaren Positionen der Beugungspeaks konnten die Gitterkonstanten der Oberflächen ermittelt werden. Die erhaltenen Werte stimmen mit der bereits bekannten Struktur der Oberfläche überein. Mithilfe von Messungen der Modulation der Intensität des spekulären Peaks als Funktion der Strahlenergie konnten Terrassen und Stufenhöhen auf den Oberflächen analysiert werden. Die Ergebnisse offenbaren relativ flache Bi(111) und Sb(111) Oberflächen, die ermittelten Stufenhöhen befinden sich in guter Übereinstimmung mit aktuellen Berechnungen.

Unter Verwendung der GR-Methode und Close-Coupling (CC) Berechnungen konnten die Oberflächenkorrugationen aus den relativen Peakhöhen der Messungen extrahiert werden. Die Amplituden der resultierenden Korrugationen befinden sich im Bereich von 10% für Bi(111), beziehungsweise 13% (GR) bis 17% (CC) für Sb(111), jeweils relativ zur Gitterkonstante der Oberflächen. Diese, im Vergleich zu anderen metallischen Oberflächen relativ großen Korrugationen, könnten auf die elektronischen Strukturen am Fermi-Niveau der Oberflächen zurückzuführen sein.

Zwischen den rein elastischen Beugungspeaks konnten Resonanzeffekte beobachtet werden, deren Analyse zu drei (Bi), beziehungsweise fünf (Sb) gebundenen Zuständen der He Atome in den Interaktionspotentialen führte. Aufgrund der Energieniveaus dieser Zustände konnten Interaktionspotentiale zwischen He und Oberfläche mit Tiefen von (8.3 ± 0.8) meV (Bi) und (4.4 ± 0.1) meV (Sb) bestimmt werden.

Intensitätsmessungen der Beugungspeaks als Funktion der Oberflächentemperatur im Bereich zwischen 98 und 447 K wurden dazu verwendet, Debye-Waller Faktoren und somit Informationen über Gitterschwingungen der Bi(111)- und Sb(111)-Oberflächen zu gewinnen. Aus den Analysen dieser Messungen konnten die Oberflächen-Debye-Temperaturen zu (84 ± 8) K (Bi) beziehungsweise (155 ± 3) K (Sb) bestimmt werden. Weiters konnten aufgrund von "kinematic focusing" auftretende Resonanzeffekte unlängst veröffentlichten Berechnungen von Phononenmoden auf Sb(111) zugeordnet werden.

Articles related to this Work

(1) *Elastic and inelastic scattering of He atoms from Bi(111)*
A. Tamtögl, **M. Mayrhofer-Reinhartshuber**, N. Balak, W.E. Ernst, and K.-H. Rieder
J. Phys.: Condens. Matter **22**, 304019 (2010)

(2) *Vibrational dynamics and surface structure of Bi(111) from helium atom scattering measurements*
M. Mayrhofer-Reinhartshuber, A. Tamtögl, P. Kraus, K.-H. Rieder, and W.E. Ernst
J. Phys.: Condens. Matter **24**, 104008 (2012)

(3) *Surface and subsurface phonons of Bi(111) measured with helium atom scattering*
A. Tamtögl, P. Kraus, **M. Mayrhofer-Reinhartshuber**, D. Campi, M. Bernasconi, G. Benedek, and W. E. Ernst
Phys. Rev. B **87**, 035410 (2013), Erratum: 159906(E) (2013)

(4) *Resonance-enhanced inelastic He-atom scattering from subsurface optical phonons of Bi(111)*
P. Kraus, A. Tamtögl, **M. Mayrhofer-Reinhartshuber**, G. Benedek, and W.E. Ernst
Phys. Rev. B **87**, 245433 (2013)

(5) *Helium atom scattering investigation of the Sb(111) surface*
M. Mayrhofer-Reinhartshuber, A. Tamtögl, P. Kraus, and W. E. Ernst
J. Phys.: Condens. Matter **25**, 395002 (2013)

(6) *Surface Debye temperature and vibrational dynamics of Antimony(111) from helium atom scattering measurements*
A. Tamtögl, **M. Mayrhofer-Reinhartshuber**, P. Kraus, K.-H. Rieder, and W.E. Ernst
Surf. Sci. **617**, 225-228 (2013)

(7) *The Helium-Surface Interaction Potential of Sb(111) from Scattering Experiments and Close-Coupling Calculations*
M. Mayrhofer-Reinhartshuber, P. Kraus, A. Tamtögl, S. Miret-Artés, and W.E. Ernst
Phys. Rev. B **88**, 205425 (2013)

Note: Articles (2) and (5)-(7) are contained within this work. The interested reader is referred to the PhD thesis of Anton Tamtögl[1], in which the contents of articles (1)-(4) are summarised and the used HAS apparatus H.Å.N.S. is described in detail. Further studies of the antimony(111) surface, especially results from inelastic HAS including the surface phonon dispersion, will be published in the PhD thesis of Patrick Kraus, which is expected to be published until end 2014.

Contents

List of Figures

List of Tables

List of Abbreviations

$\hbar$	reduced Planck constant $\hbar = \frac{h}{2\pi}$
λ_{i}	*de Broglie* wavelength of incident beam
$\hat{\mathbf{e}}_{\mathbf{x}}, \hat{\mathbf{e}}_{\mathbf{y}}, \hat{\mathbf{e}}_{\mathbf{z}}$	unit vectors
$\mathbf{G}$	2D reciprocal lattice vector
Θ_{i},Θ_{f}	incident and final angle
E_{i},E_{f}	energy of incident/final beam
E_n	energy of n^{th} bound state
h	Planck constant
k_{B}	Boltzmann constant
m	mass of particle (He)
p	momentum
T_{S}	surface temperature
Bi	Bismuth
CC	close-coupling
HAS	Helium Atom Scattering
He	Helium
KF	Kinematic(al) Focusing
SAR	Selective Adsorption Resonance
Sb	Antimony
UHV	ultra-high vacuum

1 Introduction

1.1 Motivation

With the recent focus on nano-scale materials, the study of physical as well as chemical properties of surfaces has become more and more important. There exists a broad variety of surface sensitive techniques (LEED, HREELS, ARPES, XPS, AES, ...) which promise an investigation of surfaces under different aspects. Unfortunately, most methods exhibit a certain penetration depth into the bulk and the measured observables may be contaminated by bulk properties. Furthermore, some techniques are restricted to obtain only static or long time-scale characteristics.

In contrast, in Helium Atom Scattering (HAS) the impinging atoms of a supersonic helium (He) beam are scattered approximately 2-3 Å above the first atomic layer by the electron density. Therefore, this technique offers the advantage of an exclusively surface sensitive method and has proven its merits within the scientific community of surface science. Especially if the interest of research lies in the dynamics of surfaces, this special technique unfolds its full power. Although HAS has been a very well developed method, new technical efforts towards better signal intensity and resolution yielded considerable improvements during the last years[2].

Since 2009, the Institute of Experimental Physics at the Technical University in Graz is operating a new HAS apparatus[3]. After its characterisation, first HAS measurements from the (111)-surface of the semimetal bismuth (Bi) were performed. The obtained results were summarised in the thesis of Anton Tamtögl[1].

The first part of the present thesis is based on this work and provides supplementary information on the results of HAS from Bi(111). After the completion of the investigation of Bi(111), HAS was used to characterise the antimony Sb(111) surface. The choice of Sb(111) was motivated by the interesting findings of the HAS studies on Bi(111), like the high surface corrugation[4,5], detectable subsurface phonon modes[6,7] or distinctive effects from selective adsorption resonances[8]. Both Sb and Bi belong to the group of semimetals, they have the same crystal structure and appear as building blocks in the interesting group of topological insulators[9]. Hence, the experimental investigation of HAS from Sb(111) represents an opportunity to prove and improve theoretical models, e.g. the recently calculated surface phonon dispersion of Sb(111)[10], as well as to support efforts towards a complete understanding of the group of semimetals and topological insulators.

1.2 Helium Atom Scattering

The technique of HAS has several advantages compared to other methods, as for example X-ray-, neutron- or electron-diffraction. For momenta and de Broglie wavelengths of interest in surface studies, He atoms require only low kinetic energies between 10 and 200 meV and will not penetrate deeply into the bulk material.

Hence, they are strictly sensitive to the electronic corrugation arising from the very first layer of surface atoms. Due to the periodicity of this corrugation, diffraction peaks of the He intensity can be observed. The relative heights of these peaks together with resonance effects due to temporarily bound He atoms provide information on the shape of the He-surface interaction potential[11].

The energy-wavevector relation of He atoms is located in a region close to neutrons. Although both probing particles are well suited for the interaction with phonons, in contrast to the surface sensitive He atoms, neutrons penetrate deeply into the bulk and are used for the investigation of bulk phonons[12,13].

Furthermore, He atoms are chemically, magnetically and electrically inert, hence the method of HAS is a completely non-destructive technique. The electrically neutral He atoms also allow the investigation of insulating surfaces. In conclusion, HAS opens the possibility for the investigation of surface structures and dynamics for various materials[11,12,14].

1.3 Organisation of this Thesis

The present work is organised as a cumulative thesis, i.e. the main scientific results are included as published articles in peer-reviewed journals (chapters 5 - 8). Each of these parts starts with a short description of the experimental work and analysis and set out those parts of the publication written by the author of this thesis. Prior to this, a short description of the used method of HAS and an introduction into the investigated surfaces of bismuth and antimony are presented. Improvements and further characterisation of the experimental setup is presented in chapter 3. Finally, the novel findings of this work are summarised in chapter 9.

2 Theoretical Background

2.1 The Helium Beam

As a prerequisite for HAS experiments, a beam of helium (He) atoms has to be generated. To achieve accurate measurements, its velocity distribution has to be as narrow as possible. For that purpose a supersonic expansion is used to create a nearly monoenergetic He beam[15]. The He gas is expanded through a nozzle from a high-pressure region (p_{He}) into a low-pressure region (p_1). If these pressures have a ratio p_{He}/p_1 large enough, sonic speed of the gas flow is obtained (Mach number $M_{\mathrm{a}} = 1$). Further increase of the ratio leads to a supersonic expansion ($M_{\mathrm{a}} > 1$). Due to the fast expansion through a short converging nozzle, heat conduction and friction can be neglected and the process is approximately adiabatic. Hence an adiabatic cooling of the gas occurs and most of its internal energy is converted into translational kinetic energy of the atoms. Passing through a continuum flow regime just after the nozzle, the He atoms reach a region of molecular flow at a distance d_{s} behind the nozzle[15,16]. There, a special aperture with conical shape (*skimmer*) is used to select a part of the beam in which the atoms move along a very well defined direction. By using equilibrium thermodynamics, it can be shown that the energy E_{i} of the He beam approximately depends only on the internal (thermal) energy of the He atoms given by the temperature T of the high-pressure He gas,

$$E_{\mathrm{i}} = \frac{5}{2} k_{\mathrm{B}} T, \tag{2.1}$$

with k_{B} the Boltzmann constant. Compared to the Maxwell-Boltzmann distribution of a beam generated by an effusive source, the supersonic beam has a much smaller energy spread and usually a much higher intensity[1].

It has to be noted that the basics of the supersonic expansion have been described in a simplified form. A more complete description of the process as well as occurring effects can be found e.g. in the books by Pauly[15,17] . In the experiments of this thesis, He gas with a purity $> 99.9999\%$ was used, the nozzle diameter was $d = 10$ µm, typical pressure values were $p_{\mathrm{He}} = 50$ bar and $p_1 \leq 1 \cdot 10^{-6}$ mbar and the distance between nozzle and skimmer $d_{\mathrm{s}} \approx 10$ mm ($M_{\mathrm{a}}(T = 65\ \mathrm{K}) \approx 100$, energy spread $\frac{\Delta E}{E} \approx 1.5\%$)[1].

2.1.1 Kinematic Parameters of the Helium Beam

The principle of wave-particle duality postulates that every particle is treatable as a wave with the *de Broglie* wavelength λ_i,

$$\lambda_\mathrm{i} = \frac{h}{p} \tag{2.2}$$

with p the momentum of the particle and h the Planck constant. In terms of the kinetic energy $E_\mathrm{i} = \frac{p^2}{2m}$ of the atoms with mass m, their wavelength is given by

$$\lambda_\mathrm{i} = \frac{h}{\sqrt{2mE_\mathrm{i}}}. \tag{2.3}$$

By using the wavevector $\mathbf{k}_\mathrm{i}$ ($k_\mathrm{i} = |\mathbf{k}_\mathrm{i}|$) of the atoms and the relation $\lambda_\mathrm{i} = 2\pi/k_\mathrm{i}$, the energy may be expressed as

$$E_\mathrm{i} = \frac{\hbar^2 k_\mathrm{i}^2}{2m} \tag{2.4}$$

with $\hbar = \frac{h}{2\pi}$.

2.2 Surface Description

Throughout the work of this thesis, HAS was used to investigate the structures and dynamics of crystal surfaces. Hence, a short introduction into the framework of crystal description is given in this section. Further and more detailed information can be found in solid state physics textbooks (e.g.[18,19]).

2.2.1 Crystal Structure

In an ideal crystal, the atoms are arranged in a periodic lattice, which is a three-dimensional arrangements of points. All necessary information of the crystals structure is included in the *unit cell*, which is a subunit of this lattice. In the bulk, the unit cell is defined by three vectors: $\mathbf{a}$, $\mathbf{b}$, $\mathbf{c}$. When these unit cells are stacked together to fill the whole space, the crystal lattice is obtained. The crystal fulfils translational invariance along all three space coordinates. Hence, it looks exactly the same at the points $\mathbf{r}$ and $\mathbf{r}'$ as long as they fulfil

$$\mathbf{r}' = \mathbf{r} + h \cdot \mathbf{a} + k \cdot \mathbf{b} + l \cdot \mathbf{c} \tag{2.5}$$

with the integers h, k and l. If equation (2.5) is fulfilled for *every* point at which the lattice looks the same, $\mathbf{a}$, $\mathbf{b}$ and $\mathbf{c}$ are defining a *primitive unit cell* of the lattice.

One popular choice of a primitive unit cell is given by the *Wigner-Seitz cell*, which can be constructed by the following steps:

- Construct straight lines from an arbitrarily chosen lattice point to all neighbouring lattice points.
- Construct perpendicular planes (in 2D: lines) through the centres of these lines.
- The Wigner-Seitz cell is the smallest volume (in 2D: area) enclosed by these planes (in 2D: lines).

In addition to the lattice of the crystal, a *basis* defines the positions of the atoms within the unit cell, hence also within the whole lattice[18,19].

2.2.2 Surface Structure

By cutting a three-dimensional crystal along a certain plane, a surface of this crystal is obtained. The surface is usually indicated with the three *Miller indices* of the corresponding bulk plane[20]. Again, points for translational symmetry within the surface plane exist. Due to the reduction of dimensions, equation (2.5) is reduced to

$$\mathbf{R}' = \mathbf{R} + h \cdot \mathbf{a} + k \cdot \mathbf{b}, \tag{2.6}$$

where all occurring vectors lie in the plane of the surface. The coordinate system is chosen in a way, that the z-axis with its unit vector $\hat{\mathbf{e}}_\mathbf{z}$ is perpendicular to the surface. In surface science, capital letters typically indicate vectors parallel to the surface ($\mathbf{R}, \mathbf{R}'$). Note that in contrast to the symmetry points, the atoms of the surface do not necessarily lie within one plane[19]. In the two-dimensional case of a surface, only five basically different lattice structures (*Bravais lattices*) exist[1,20,21].

2.2.3 Reciprocal Space

In diffraction experiments usually the *reciprocal lattice* is used. To obtain the basis vectors $\mathbf{a}^*, \mathbf{b}^*$ in a two-dimensional reciprocal space, the following equations have to be applied[18,19]:

$$\mathbf{a}^* = 2\pi \frac{\mathbf{b} \times \mathbf{n}}{\mathbf{a}(\mathbf{b} \times \mathbf{n})} \tag{2.7}$$

$$\mathbf{b}^* = 2\pi \frac{\mathbf{n} \times \mathbf{a}}{\mathbf{a}(\mathbf{b} \times \mathbf{n})} \tag{2.8}$$

This is equal to the definition in three dimensions, except that the third basis vector ($\mathbf{c}$ in equation (2.5)) is replaced with $\mathbf{n}$, which is the unit vector normal to the surface. In this reciprocal space, a general translation vector is given by

$$\mathbf{G}_{hk} = h \cdot \mathbf{a}^* + k \cdot \mathbf{b}^*, \tag{2.9}$$

where the integer numbers h and k are denoted as *Miller indices*. These Miller indices are also used to specify a particular direction, e.g. in scattering experiments. In reciprocal space, a primitive unit cell, which is constructed in the same way as the Wigner-Seitz cell, is referred to as *Brillouin zone*[18].

2.3 Surface Phonons

In the quantum-mechanical treatment of lattice vibrations, the quasiparticles of these vibrations are called *phonons*. Each material gives rise to different phonon modes and their specific properties are expressed by their dispersion relation, in which the phonon energy/frequency is given as a function of their wavevector for the entire Brillouin zone. The energy and number of occupied phonon states often determine the characteristics, e.g. the heat capacity or the thermal conductivity of a material[18].

Phonons localised at the surface are referred to as *surface phonons*. Their amplitudes decay drastically into the bulk due to the crystals broken translational invariance at its surface. Hence, surface phonons exhibit a propagation direction parallel to the surface[22]. The influence of surface phonons on HAS measurements can be taken into account by including the Debye-Waller factor in the analysis of the measurements (see section 2.5.3).

Basic introductions as well as detailed descriptions of bulk and surface phonons can be found in solid state physics textbooks[18], or in specialised literature[1,23]. For theoretical predictions of surface phonon modes, density functional perturbation theory (DFPT) is often used. By using this method, the surface phonon modes had been calculated for the Bi(111)[6] and Sb(111)[10] surfaces.

2.3.1 Surface Phonon Measurements

Since HAS has a high cross section for the creation and annihilation of surface phonons, it is the most popular technique for the measurement of the surface phonon dispersion[11]. In the early times of atom scattering, surface phonon dispersion curves had been extracted from angular distributions of He and Ne scattered from LiF and NaF crystals. In these studies, small peaks in the surrounding of the elastic peaks had been analysed and associated with one-phonon scattering processes[24,25]. Exploitation of kinematic focusing effects improved the results of the analysis of these measurements[26]. Because of higher He beam intensities due to improved creation and detection techniques, during the last decades time-of-flight (TOF) measurements became the method of choice for phonon measurements with a resolution of about 0.1 meV[11,27]. The He atoms gain or lose energy due to the annihilation or creation of (surface) phonons at the sample surface. Although multiphonon-processes are present in every HAS measurement with finite sample temperatures, for simplification usually only single-phonon events are taken into

account. Thus, the energy ΔE of a created or annihilated phonon is given by

$$\Delta E = E_\mathrm{f} - E_\mathrm{i}. \tag{2.10}$$

The energy of the detected He atoms E_f and hence their energy gain compared to their initial energy E_i are determined by a measurement of their flight-time along a well-defined path (chopper-sample-detector) at constant velocities in each section. The multiphonon contribution mentioned above creates a small, but rather broad peak superimposed to the relevant TOF or angular HAS measurements. To obtain comparable and reasonable data, it has to be subtracted from the measured signals. In addition the sample surface may be cooled down (e.g. with liquid nitrogen) to suppress this perturbing influence as much as possible.

To obtain even better resolution, HAS with ^{3}He and the spin-echo technique made it possible to analyse the dynamics on a surface with neV resolution[2,28,29].

2.3.2 Scancurve

With the HAS apparatus used during the work of this thesis, surface phonons can be measured with the TOF technique. Due to kinematic conditions, i.e. the conservation laws for energy and parallel momentum, at each angular position only phonons with a specific wavevector ΔK and energy ΔE can be detected. This is expressed by the so-called *scancurve*, which is given by[11,12]

$$\frac{\Delta E}{E_\mathrm{i}} + 1 = \frac{\sin\Theta_\mathrm{i}^2}{\sin\Theta_\mathrm{f}^2}\left(1 + \frac{\Delta K}{K_\mathrm{i}}\right)^2. \tag{2.11}$$

Examples for scancurves are illustrated in figure 2.1. To obtain phonons throughout the whole dispersion curve, the incident angle of the He beam has to be varied.

The measurement of surface phonon modes was not subject of the work for this thesis, but the scancurve is also important for the analysis of angular HAS scans since resonance effects in form of Kinematic Focusing (KF) may occur (see section 2.6.2).

2.4 The Atom-Surface Interaction Potential

In contrast to other particles such as electrons or neutrons, which are scattered from the ion cores of the atoms, in the scattering process of He, the atoms are scattered by the charge density distribution slightly above the surface. Hence, the scattering process is mainly influenced by the shape of the He-surface interaction potential, which is composed of interaction potentials of the He atom with every surface atom of the crystal. This total interaction potential $V(\mathbf{r})$ depends on the lateral position $\mathbf{R}$ of the He atom (parallel to the surface) and its distance perpendicular to the surface z with

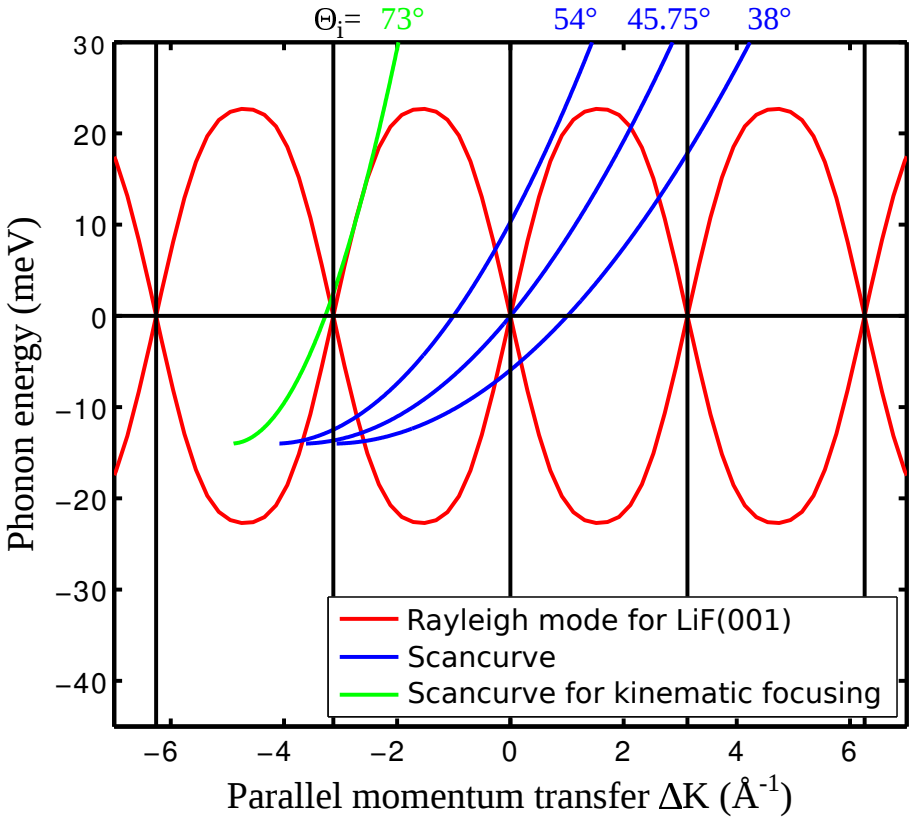

Figure 2.1: Illustration of scancurves (blue and green lines) for $E_\mathrm{i} = 14$ meV and different incident angles Θ_i for a HAS apparatus with a fixed angle $\Theta_\mathrm{SD} = 91.5°$ between source and detector. The red line depicts the surface phonon dispersion curve for LiF(001) along the $\langle 10 \rangle$ direction as determined by Brusdeylins et al.[30]. At the intersections between the scancurves and the dispersion curve, phonons can be detected. The green curve depicts the scancurve for an angle, at which kinematical focusing occurs, i.e. the scancurve is tangent to a surface phonon mode.

$\mathbf{r} = (\mathbf{R}, z)$. In general $V(\mathbf{r})$ is also a function of time $V(\mathbf{r}, t)$, but for the theoretical treatment of elastic scattering, the surface atoms can be assumed to be fixed at their equilibrium positions at a certain temperature. Therefore, the time average $\langle V(\mathbf{r}, t)\rangle_t$ is sufficient for further analysis[1,11].

Two different forces which originate from the interaction with each individual surface particle act on the approaching He atoms. London dispersion (van der Waals) forces, resulting from instantaneously induced dipoles, accelerate the He atom towards the surface. The interaction between electrons of the surface and the closed-shell of the He atom causes a short-range counterpart, the Pauli repulsion[1,8,31,32].

Although the approach fits best for solids with a closed-shell character (e.g. ionic crystals), usually also for other materials such as metals or semiconductors, gas phase two-body potentials are summed up to obtain an atom-surface interaction potential[33,34]. These two-body potentials are only known for a few systems, hence approximate models have to be used to find an estimation for the interaction[11,31]. One of the most popular choices for such a two-body model potential is the Lennard-Jones (12-6) potential:

$$V_{\mathrm{LJ}}(r) = 4\epsilon\left[\left(\frac{\sigma}{r}\right)^{12} - \left(\frac{\sigma}{r}\right)^{6}\right] \tag{2.12}$$

with ϵ the well depth of the potential, σ the distance at which the potential is zero and r the distance between the two particles[35].

2.4.1 The 9-3 Potential

Since each He atom interacts with all atoms of the surface, all individual Lennard-Jones potentials (2.12) have to be combined. Thereto, the discrete lattice is replaced with a continuum, which allows to use integrals instead of sums. By the successive integration over the space coordinates of the whole semi-infinite lattice of these individual potentials, the atom-surface potential as a 9-3 potential,

$$V(z) = \frac{\sqrt{27}}{2} D\left[\left(\frac{\sigma}{z}\right)^{9} - \left(\frac{\sigma}{z}\right)^{3}\right], \tag{2.13}$$

is obtained[8]. The well depth of the attractive part is given by D, z denotes the normal distance from the surface and σ is the distance at which the potential is zero.

The distorted wave Born approximation[36] can be used to obtain the eigenvalues E_n (energy of the n^{th} bound-state) for this potential:

$$E_n \simeq -D\left[1 - \frac{\pi\hbar}{3.07}\frac{n+\frac{1}{2}}{\sigma\sqrt{2mD}}\right]^6 \tag{2.14}$$

Although the asymptotic form of the attractive part of the potential is reflected very well with the 9-3 potential, the repulsion term is a sub-optimal approximation for an interatomic interaction[1,31]. However, it was shown recently that the bound states of semimetal surfaces can be described very well by using this approximation[8].

2.4.2 The Corrugated Potential

Note that in equation (2.13) the potential is only a function of z. This approximation is strictly valid only for surfaces with a flat corrugation, e.g. for metal surfaces, at which the Smoluchowski effect smooths out the charge density corrugation[37]. For ionic or semimetallic surfaces, the potential follows the corrugation of the surface atoms, which are arranged periodically. Hence, it can be written as a Fourier series

$$V(\mathbf{r}) = V(\mathbf{R}, z) = \sum_{\mathbf{G}} V_{\mathbf{G}}(z) \cdot e^{i\mathbf{G}\cdot\mathbf{R}} \tag{2.15}$$

with a sum over the surface reciprocal lattice vectors $\mathbf{G}$[11,31]. Since in HAS experiments the He beam is illuminating a rather large area on the sample surface, it is not possible to distinguish between He atoms impinging on different lateral positions. Thus, from HAS experiments only the lateral average of the interaction potential can be determined. This lateral average is expressed by the first term $V_{00}(z)$ of equation (2.15)[1]:

$$V(\mathbf{R}, z) = V_{00}(z) + \sum_{\mathbf{G}\neq 0} V_{\mathbf{G}}(z) \cdot e^{i\mathbf{G}\cdot\mathbf{R}} \tag{2.16}$$

2.5 Elastic HAS

Usually HAS is used to study surfaces with periodic structures. Due to their periodicity diffraction occurs. The so-called Laue equations act as a description and give three conditions for this diffraction. They state that the change from the incident wavevector $\mathbf{k}_\mathrm{i}$ to the final wavevector $\mathbf{k}_\mathrm{f}$ of the atoms has to be equal to a reciprocal lattice vector $\mathbf{g}$. Together with the condition for elastic scattering, where the energy of the incident atoms E_i and the outgoing atoms E_f stays the same, they form the following four equations[1,35,38]:

$$\mathbf{k}_\mathrm{f} = \mathbf{k}_\mathrm{i} + \mathbf{g} \tag{2.17}$$

$$E_\mathrm{f} = E_\mathrm{i} \tag{2.18}$$

These equations have to be fulfilled for diffraction peaks in elastic HAS.

In surface science, a wavevector $\mathbf{k}$ is usually split into two components $\mathbf{k} = (\mathbf{K}, k_z)$, where k_z denotes the component perpendicular to the surface (the unit vector $\hat{\mathbf{e}}_z$ of the coordinate system points outward) and $\mathbf{K}$ is the component parallel to the surface. The unit vectors $\hat{\mathbf{e}}_x$ and $\hat{\mathbf{e}}_y$ lie in the plane of the surface. Together with $\hat{\mathbf{e}}_z$, they form a right-handed (standard) Cartesian coordinate system. The direction of incidence of a certain wavevector is defined with two angles: The azimuthal angle ϕ is defined as the angle between the wavevector and $\hat{\mathbf{e}}_x$, whereas the polar angle Θ is measured towards $\hat{\mathbf{e}}_z$.

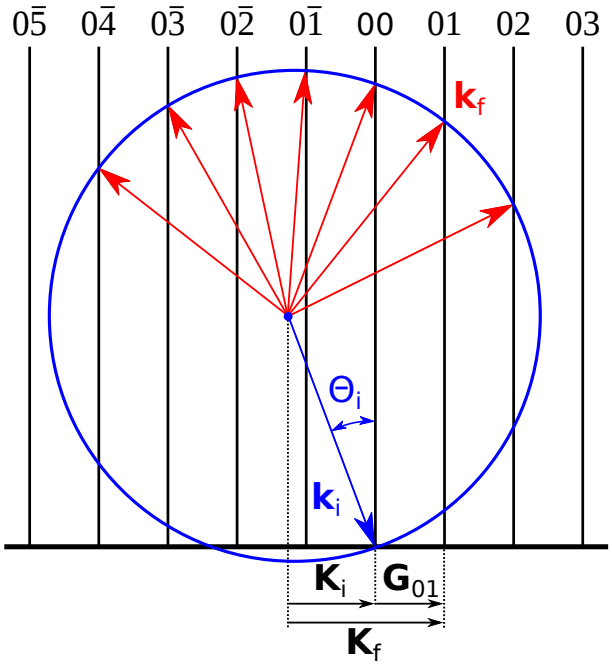

Figure 2.2: The Ewald construction for diffraction from surfaces illustrates the Bragg condition (2.19). At a particular angle Θ_i, diffraction peaks can be observed at the directions of $\mathbf{k}_f$. The vertical lines represent the periodicity of the surface. Vectors are shown for $\mathbf{G}_{hk} = \mathbf{G}_{01}$.

Scattering from a surface, which is defined by the reciprocal lattice vectors $\mathbf{G}_{hk}$, occurs if the Bragg condition

$$\mathbf{G}_{hk} = \mathbf{K}_f - \mathbf{K}_i \tag{2.19}$$

is fulfilled[35,38]. As an illustration for this condition, the *Ewald construction* for $\mathbf{G}_{hk} = \mathbf{G}_{01}$ is shown in figure 2.2[11].

2.5.1 Calculation of HAS Peak Positions

For the special case of *in-plane* diffraction, where the incident wavevector $\mathbf{k}_i$, the final wavevector $\mathbf{k}_f$ and the z-axis ($\mathbf{e}_z$) are all lying in one plane,

$$\mathbf{K}_f = |\mathbf{k}_f| \sin \Theta_f \tag{2.20}$$
$$\mathbf{K}_i = |\mathbf{k}_i| \sin \Theta_i \tag{2.21}$$

holds. Together with the conservation of energy equation (2.18) and a fixed angle between source and detector of the apparatus

$$\Theta_{SD} = \Theta_i + \Theta_f, \tag{2.22}$$

the Bragg condition (2.19) yields[1]

$$\Theta_{\mathrm{i}} = \frac{\Theta_{\mathrm{SD}}}{2} - \arcsin\left[\frac{G_{hk}}{2 \cdot |\mathbf{k}_{\mathrm{i}}| \cdot \cos\frac{\Theta_{\mathrm{SD}}}{2}}\right]. \tag{2.23}$$

This equation provides the incident angles of the He beam ($|\mathbf{k}_{\mathrm{i}}|$), at which diffraction peaks can be detected with an apparatus having a fixed source-detector angle (Θ_{SD}) and a sample crystal with a known surface structure G_{hk}. Equation (2.23) may either be used to determine an unknown surface structure from diffraction peaks measured at Θ_{i} or to calculate the positions of the diffraction peaks (h, k) for given surface reciprocal lattice vectors G_{hk} lying in the plane of $\mathbf{k}_{\mathrm{i}}$ and $\mathbf{k}_{\mathrm{f}}$. Since the HAS apparatus used for the measurements of this thesis has its source and detector arm fixed in one plane, in-plane diffraction measurements were the method of choice in the presented experiments.

2.5.2 Surface Corrugation

As described in section 2.4, in HAS experiments the He atoms are scattered by the charge distribution at the surface. The periodicity of this electronic corrugation gives rise to the occurrence of diffraction (Bragg) peaks. Furthermore, the shape of the distribution, e.g. its peak-to-peak values influences the height of the Bragg peaks.

Usually a mathematical function $\xi(\mathbf{R})$ is used to model this shape and is referred to as electronic *surface corrugation*. The common procedure is to use the surface corrugation as a model for the investigated surface and calculate expected diffraction probabilities, i.e. the heights of the diffraction peaks, by theory. In order to find the best fitting function, ξ has to be optimised by comparing theoretically and experimentally obtained peak heights.

Schrödinger Equation

If the beam energy is in a low energy range, like in the experiments presented in this thesis, quantum theory can be used to describe the scattering process. Hence, the Schrödinger equation

$$\left[-\frac{\hbar^2}{2m}\nabla^2 + V(\mathbf{r})\right]\Psi(\mathbf{r}) = E\Psi(\mathbf{r}) \tag{2.24}$$

has to be solved[35,39,40]. Thereto, the helium-surface interaction potential $V(\mathbf{r})$ has to be specified. Since the complexity and therewith the possibility of solving the Schrödinger equation, depends on the choice of $V(\mathbf{r})$, several different approaches and approximations exist and will be discussed in the following sections. In the diffraction from a crystal surface, i.e. a structure with a two-dimensional periodicity, parallel to the surface the wavefunction $\Psi(\mathbf{r})$ can be described by *Bloch waves*[11]:

$$\Psi(\mathbf{r}) = \Psi(\mathbf{R}, z) = e^{\mathrm{i}\mathbf{K}_{\mathrm{i}}\cdot\mathbf{R}} + \sum_{\mathbf{G}} e^{\mathrm{i}\mathbf{G}\cdot\mathbf{R}}\Psi_G(z) \tag{2.25}$$

HCW Model

As a first simple approximation of an atom-surface interaction potential $V(\mathbf{r})$, a hard corrugated wall (HCW) model is often used[35,39]. Three main assumptions are made in this model[11]:

- The potential has no attractive part.
- The repulsive part has an infinitely steep slope.
- The surface atoms are motionless.

Hence, the potential is defined as

$$V(\mathbf{r}) = V(\mathbf{R}, z) = \begin{cases} 0 & \text{for } z > \xi(\mathbf{R}) \\ \infty & \text{for } z \leq \xi(\mathbf{R}) \end{cases} . \tag{2.26}$$

In the HCW model, the wavefunction Ψ has to vanish inside the hard hard corrugated wall to fulfil the boundary condition (2.26):

$$\Psi[\mathbf{R}, z \leq \xi(\mathbf{R})] = 0 \tag{2.27}$$

Rayleigh Ansatz

The *Rayleigh ansatz* is an approximate approach for the calculation of the intensities of HAS diffraction peaks[39]. Far away from the surface ($z >> \xi(\mathbf{R})$), the He beam can be treated as a plane wave. In the assumption developed by Lord Rayleigh, this description for the incident and final beams is used for the whole range $z > \xi(\mathbf{R})$[41]. Thus, the wavefunction $\Psi(\mathbf{r})$ from equation (2.25) becomes[11]

$$\Psi(\mathbf{r}) = \Psi(\mathbf{R}, z) = e^{\mathrm{i}(\mathbf{K}_\mathrm{i}\cdot\mathbf{R} \, - \, k_{\mathrm{i},z}\cdot z)} + \sum_{\mathbf{G}} A_{\mathbf{G}} e^{\mathrm{i}[(\mathbf{K}_\mathrm{i}+\mathbf{G})\cdot\mathbf{R} \, + \, k_{G,z}\cdot z]}. \tag{2.28}$$

The incident beam is represented by the first term, whereas the sum is over all reciprocal lattice vectors $\mathbf{G}$, i.e. all scattered beams. $k_{\mathrm{i},z}$ and $k_{G,z}$ denote the perpendicular components of the wavevectors for the incoming and outgoing beams. The coefficients $A_{\mathbf{G}}$ give the scattering amplitudes, which are proportional to the scattered intensities (see equation (2.38)).

On the way to solve the scattering problem, the boundary condition for the wavefunction $\Psi[\mathbf{R}, z = \xi(\mathbf{R})] = 0$ is applied to obtain

$$\sum_{\mathbf{G}} A_{\mathbf{G}} e^{\mathrm{i}[\mathbf{G}\cdot\mathbf{R} \, + \, k_{G,z}\cdot\xi(\mathbf{R})]} = -e^{-\mathrm{i}(k_{\mathrm{i},z}\cdot\xi(\mathbf{R}))}. \tag{2.29}$$

This equation has to be fulfilled for every $\mathbf{R}$ throughout the unit cell. Therewith the scattering amplitudes $A_{\mathbf{G}}$ can be determined theoretically for a given surface corrugation

$\xi(\mathbf{R})$. Usually $\xi(\mathbf{R})$, as a representation of the surface, is adjusted until the best fit between theoretical and experimental data is obtained. Although the convergence of the Rayleigh hypothesis seems to be restricted to corrugation with a maximum amplitude of 18.8% of the lattice constant (in two dimensions)[35], alternative methods for valid solutions beyond this limit exist[42].

GR Method

Based on the Rayleigh assumption, the *GR method* converts equation (2.29) by multiplying both sides with $\exp[\mathrm{i}k_{\mathrm{i},z} \cdot \xi(\mathbf{R})]$ into[43,44]

$$\sum_{\mathbf{G}} A_{\mathbf{G}} M_{\mathbf{GR}} = -1 \tag{2.30}$$

with

$$M_{\mathbf{GR}} = e^{\mathrm{i}[\mathbf{G}\cdot\mathbf{R} \, + \, (k_{G,z}+k_{\mathrm{i},z})\xi(\mathbf{R})]}. \tag{2.31}$$

The equations (2.30) can be seen as an interpolation problem with a condition for a unique solution to exist that is given by

$$|M_{\mathbf{GR}}| \neq 0. \tag{2.32}$$

For all lattice points $\mathbf{R}$ and reciprocal lattice points $\mathbf{G}$, the amplitudes $A_{\mathbf{G}}$ have to fulfil equations (2.30) and (2.31). It can be shown that equation (2.32) is automatically satisfied if

$$\mathbf{R}' \neq \mathbf{R} + m\mathbf{a} + n\mathbf{b}, \tag{2.33}$$

with m and n integers and any two (different) points $\mathbf{R}$ and $\mathbf{R}'$[43]. Hence, the solution has to be calculated for all points $\mathbf{R}$ within the unit cell and can thereafter be extended to all points of the surface due to the translational symmetry of the crystal. Although these equations have to be solved for all points $\mathbf{R}$ and $\mathbf{G}$, in practice a "large enough" number N of points is chosen to discretise the problem. Convergence is achieved, if the solutions only change negligible for a further increase of N[43,44]. Stoll et al.[45] improved the stability of the GR method by introducing further conditions for the selection of the $\mathbf{R}$ and $\mathbf{G}$ vectors, even beyond the Rayleigh limit.

Beeby Correction

As an improvement for the strict HCW model, a slightly better approximation can be obtained by applying the *Beeby correction*. For this correction the always existent attractive part of the potential, which is neglected in the standard HCW-approach, is included in a simple way[39,46]: The attractive well is assumed to have a spatially uniform well depth D, which is added to the energy of the incident beam energy. Hence, the

incident wavevector k_i as well as Θ_i have to be replaced in the calculations with an effective k'_i given by

$$k'_\mathrm{i} = \sqrt{\frac{2m(E_\mathrm{i}+D)}{\hbar^2}} = k_\mathrm{i}\sqrt{1+\frac{D}{E_\mathrm{i}}} \tag{2.34}$$

and a smaller effective angle of incidence Θ'_i with

$$sin(\Theta'_\mathrm{i}) = \frac{sin(\Theta_\mathrm{i})}{\sqrt{1+\frac{D}{E_\mathrm{i}}}}. \tag{2.35}$$

These corrections have to be also applied to the final wavevector k_f and the final angle Θ_f. Therefore, the perpendicular momentum transfer k_z is replaced by[39,47]

$$\Delta k'_z = k_\mathrm{i}\left[\sqrt{\cos^2(\Theta_\mathrm{f})+\frac{D}{E_\mathrm{i}}} + \sqrt{\cos^2(\Theta_\mathrm{i})+\frac{D}{E_\mathrm{i}}}\right]. \tag{2.36}$$

Close-Coupling Method

Beyond the HCW approach, e.g. for large surface corrugations, the scattering problem has to be treated fully quantum mechanically. Thereto, the attractive part of the potential as well as a non-infinitely steep slope have to be taken into account. The inclusion of this attractive well gives also rise to the occurrence of bound-states, in which the impinging He atoms get trapped for a short time (see section 2.6.1), which also influences the scattering process significantly[40]. In the close-coupling (CC) formalism, the Fourier expanded wavefunctions (2.25) and the Fourier expanded atom-surface interaction potential (2.16) are inserted into the Schrödinger equation (2.24). Therewith, for the diffracted waves the following set of coupled equations is obtained:[48]

$$\left[\frac{\mathrm{d}^2}{\mathrm{d}z^2} + \mathbf{k}^2_{\mathbf{G},z} - V_0(z)\right]\Psi_\mathbf{G}(z) = \sum_{\mathbf{G}'\neq\mathbf{G}} V_{\mathbf{G}'-\mathbf{G}}(z)\Psi_{\mathbf{G}'}(z) \tag{2.37}$$

$V_0(z)$ denotes the laterally and thermally averaged atom-surface interaction potential.

Wolken[49,50] had been the first to apply the CC method, namely he investigated He and H_2 scattering from LiF. In this as well as in the following applications of the CC approach in atomic and molecular scattering from surfaces[51–53], the boundary conditions for the wavefunction $\Psi_\mathbf{G}(z)$ are now defined by a vanishing wavefunction deep inside the crystal ($z \to -\infty$) and an outgoing scattered wave far away from the crystal ($z \to \infty$). While in theory the coupled equations have to be solved for an infinite number of $\mathbf{G}$ vectors, for computation they are limited to a number large enough for numerical accuracy[11]. In CC calculations it is important to include not only energetically accessible $\mathbf{G}$ vectors (diffracted waves, *open channels* with $\mathbf{k}^2_{\mathbf{G},z} > 0$), but also evanescent waves (*closed channels* with $\mathbf{k}^2_{\mathbf{G},z} < 0$).

Calculation of HAS Intensities

With the previously described methods it is possible to calculate the scattering amplitudes $A_{\mathbf{G}}$. However, in HAS experiments peak intensities $P_{\mathbf{G}}$ are measured, which are related to these amplitudes via[39]

$$P_{\mathbf{G}} = \frac{k_{\mathbf{G},z}}{k_{\mathrm{i},z}} |A_{\mathbf{G}}|^2. \tag{2.38}$$

For this equation to be true, the experiment must be set up in a classical Rutherford configuration, in which the acceptance angle of the detector is large enough to "see" the whole illuminated He beam spot on the surface[54]. As a check for validity of the performed calculations, the unitarity condition (incoming intensity has to equal to outgoing intensity) can be used[35]:

$$\sum_{\mathbf{G}} P_{\mathbf{G}} = 1 \tag{2.39}$$

Turning Points

In addition to the aforementioned methods, the corrugation function is assumed to be the equipotential surface

$$V(\mathbf{r}) = V(\mathbf{R}, z) = E_{\mathrm{i},z} \tag{2.40}$$

at the coordinates of the classical *turning points* of the He atoms, with $E_{\mathrm{i},z}$ the component of the incident energy perpendicular to the surface[39].

It is obvious that for different incident energies of the He beam, different corrugation functions are obtained. He atoms with higher incident energy will have their turning points nearer to the surface than atoms with less energy[40]. Furthermore, vibrations of the surface influence the measured peak intensities. Although measurements at temperatures up to 300 K yield results accurate enough for certain applications[55], temperature corrections should be applied. To minimise these effects, the surface corrugation $\xi(\mathbf{R})$ should be determined for a surface temperature $T_{\mathrm{S}} = 0\ K$. Since real-life experiments are performed at finite temperatures, Bragg peak intensities have to be measured at different T_{S} and extrapolated to zero surface temperature with the inclusion of the Debye-Waller factor[39].

2.5.3 Debye-Waller Factor

In the scattering process from a real surface at non-zero temperature T_{S}, the measured Bragg peak intensities are attenuated due to the thermal vibrations of the atoms. Compared to the theoretically predicted intensities, the measured peaks have less intensity because of more inelastically scattered He atoms at higher values of T_{S}. To account for this temperature dependency of the intensities, the calculated intensities I_0 for a surface

at rest have to be multiplied with the *Debye-Waller factor* to obtain intensities $I(T_\mathrm{S})$ comparable to the experiment[39]:

$$I(T_\mathrm{S}) = I_0 \cdot e^{-2W(T_\mathrm{S})} \tag{2.41}$$

The exponential function denotes the Debye-Waller factor and is given by

$$2W(T_\mathrm{S}) = \left\langle (\mathbf{u} \cdot \Delta\mathbf{k})^2 \right\rangle_{T_\mathrm{S}} \tag{2.42}$$

with $\mathbf{u}$ the displacement vector of a crystal lattice atom out of its equilibrium position. The transfer of momentum during the scattering process is given by $\Delta\mathbf{k}$. For the scalar product the thermal average has to be taken, which is indicated by the outer brackets[39]. If there is no momentum transfer parallel to the surface, equation (2.42) yields

$$2W(T_\mathrm{S}) = \left\langle u_z^2 \right\rangle \cdot (\Delta k_z)^2, \tag{2.43}$$

with $\langle u_z^2 \rangle$ the average displacement of a surface atom along the z-direction.
If a classical harmonic oscillator (frequency ω) is assumed, the average displacement is related to the temperature T via[18]

$$\frac{1}{2} M\omega^2 \left\langle u^2 \right\rangle = \frac{3}{2} k_\mathrm{B} T \quad \Rightarrow \quad \left\langle u^2 \right\rangle = \frac{3k_\mathrm{B}T}{M\omega^2}. \tag{2.44}$$

The mass of a surface atom is given by M for a monoatomic surface. For non-monoatomic surfaces, an effective mass has to be used instead[56]. In the Debye model the Debye-temperature Θ_D is related to the Debye frequency ω_D via[18]

$$\frac{\hbar\omega_\mathrm{D}}{k_\mathrm{B}T} = \frac{\Theta_\mathrm{D}}{T} \quad \Rightarrow \quad \omega_\mathrm{D} = \frac{k_\mathrm{B}\Theta_\mathrm{D}}{\hbar}. \tag{2.45}$$

The combination of this relation with equation (2.44) yields

$$\left\langle u^2 \right\rangle = \frac{3\hbar^2 T}{M k_\mathrm{B} \Theta_\mathrm{D}^2}. \tag{2.46}$$

By inserting this result into equation (2.43), the Debye-Waller factor

$$W(T_\mathrm{S}) = \frac{3\hbar^2 T_\mathrm{S}}{2M k_\mathrm{B} \Theta_\mathrm{D}^2} \Delta k_z^2 \tag{2.47}$$

is obtained.
The Beeby correction can be applied to the Debye-Waller factor to account for the attractive part of the atom-surface interaction potential with a particular well depth D. For scattering at the specular position ($\Theta_\mathrm{i} = \Theta_\mathrm{f}$), Δk_z is corrected with equation (2.36), which yields

$$\Delta k_z = 2k_\mathrm{i}\sqrt{\cos^2(\Theta_\mathrm{i}) + \frac{D}{E_\mathrm{i}}} \quad \Rightarrow \quad \Delta k_z^2 = 4k_\mathrm{i}^2 \left(\cos^2(\Theta_\mathrm{i}) + \frac{D}{E_\mathrm{i}} \right). \tag{2.48}$$

By replacing k_i with $E_\mathrm{i} = \frac{\hbar^2 k_\mathrm{i}^2}{2m}$,

$$\Delta k_z^2 = \frac{8m}{\hbar^2}[E_\mathrm{i}\cos^2(\Theta_\mathrm{i}) + D] \tag{2.49}$$

with m the mass of an impinging particle is obtained.
Equation (2.47) can then be written as

$$W(T_\mathrm{S}) = \frac{12m[E_\mathrm{i}\cos^2(\Theta_\mathrm{i}) + D]}{Mk_\mathrm{B}\Theta_\mathrm{D}^2} T_\mathrm{S}. \tag{2.50}$$

This expression for the Debye-Waller factor can be also used for geometries, in which the incident and final angles are not too different. In the experiment, $W(T_\mathrm{S})$ can be determined by measuring the He intensity of the Bragg peaks as a function of the surface temperature T_S. From the semi logarithmic plot of the intensity versus the surface temperature, the slope of a linear fit is used to calculate the Debye Waller factor and the Debye temperature. Although the considerations of the thermal attenuation with an application of the Debye-Waller and the potential well depth with the Beeby correction are good approximations, for an exact theoretical model further attenuation effects, e.g. due to multiphonon processes have to be taken into account[39].

2.5.4 Surface Steps and Terrace Height

In contrast to the ideal case of completely flat surfaces, real surfaces often have steps and terraces, e.g. due to the sample preparation process. The spot size of the He beam on the investigated surface may be larger than the typical area of these terraces. Interference effects can be used to examine their heights and distributions with HAS. Constructive and destructive interference occur due to the interaction of He beams scattered from different terrace levels[39]. When the phase shift $\Delta\varphi$ between He beams emerging from different levels is an integer $n \cdot 2\pi$, they interact constructively (*in-phase* scattering). On the other hand, destructive (*antiphase*) scattering appears with a phase shift of a half-integer $n \cdot 2\pi$.

To obtain the best signal-to-noise ratio, usually the specular peak ($\Theta_\mathrm{i} = \Theta_\mathrm{f}$) is monitored while changing the phase-shift between the He beams from different terraces with changing experimental parameters. The position of the specular beam is not only used to simplify the mathematical description, but also because the interference effects influence the narrow, coherent diffraction peaks while the broad diffuse elastic and multiphonon contribution remains mostly constant. The phase difference $\Delta\varphi$ of beams from different terraces at the measurement position of the specular peak is given by[57]

$$\Delta\varphi = 2hk_\mathrm{i}\cos\Theta_\mathrm{i} \tag{2.51}$$

where h denotes the step height. The wavevector component perpendicular to the surface is given by $k_{\mathrm{i},z} = k_\mathrm{i}\cos\Theta_\mathrm{i}$. Equation (2.51) can also be given in terms of the wavevector

transfer $\Delta k_z = 2k_{\mathrm{i},z}$ perpendicular to the surface and then reads

$$\Delta\varphi = h\Delta k_z. \tag{2.52}$$

In the experiment, $\Delta\varphi$ can be varied by changing either Θ_i or k_i, while keeping the other fixed. In the first case also the final angle Θ_f and hence the total scattering angle Θ_SD have to be changed in order to stay on the measurement position of the specular peak. Due to the need of changing the total scattering angle, this type of measurement, which is also called *rocking curve*, is not possible with the fixed source-detector geometry of the apparatus used for this study. Hence, the second type of measurement was performed by varying the nozzle temperature. As can be seen from equations (2.1) and (2.4), therewith the wavevector of the incident He beam can be tuned.

In the presence of terraces, the phase shift (2.51) "runs" through constructive and destructive interference in the experiment, fulfilling periodically *in-phase* and *antiphase* conditions. Hence, a periodic change in the intensity of the monitored specular peak is observable.

With increasing k_i, the measured He intensity of the narrow coherent specular peak decreases due to the higher nozzle temperature (less intensity of the He beam) and the *Debye-Waller effect*[58]. Because of these attenuations, the modulations due to different terrace levels produce less distinct features with higher k_i.

To find the height of the steps on the surface, a theoretical model is used to calculate the expected modulations of the intensity and compare them to the actual measurement. As a first attempt, plane waves can be assumed. By considering a coherent overlap of these waves, the expected intensity $I(\Delta k_z)$ can be calculated with[57,59]

$$I(\Delta k_z) = I_0 e^{-2W} \left| \sum_{j=0}^{\infty} a_j e^{-ij\varphi(\Delta k_z)} \right|^2 . \tag{2.53}$$

I_0 denotes the specular peak intensity for a completely flat surface without steps and $\varphi(\Delta k_z)$ is the phase shift as defined in equation (2.52). The coefficient a_j is the visible fraction of a terrace at level j. Assuming that the He beam "illuminates" a representative region of the surface, the values for a_j give the distribution of the terraces. To account for the aforementioned attenuation due to the Debye-Waller effect, the exponential prefactor e^{-2W} is included in this model.

Although it has been shown that this model is a good approximation[57,59,60], it has to be mentioned that it neglects the possible occurrence of selective adsorption resonances (see section 2.6.1). Their influence gives rise to various fine peaks and dips superimposed onto the signal originating from the different terraces, especially for low values of k_i[8]. In the theoretical model for the prediction of the He intensity signal, they are included by using close-coupling calculations (see section 2.5.2), as was done in the present study (see section 8). Beside the terrace height and distribution, a measurement of the intensity variation may also be used to determine growth modes in deposition processes[61].

2.6 Resonances in HAS Measurements

In addition to above considerations, several resonance effects may affect HAS measurements. Due to the attractive part of the He-surface interaction potential, He atoms may get trapped in bound-states and produce detectable signals in angular as well as TOF measurements. These effects are summarised under the term *Selective Adsorption (Desorption) Resonances* (SAR). Furthermore, signals may arise because of special kinematic conditions, in which the scan curve of the experiment is tangent to the dispersion curve of a surface phonon mode. This effect is referred to as *Kinematic(al) Focusing* (KF).

2.6.1 Selective Adsorption Resonances

With an energy E_i of the incident He atoms in the range of the well depth D of the He-surface interaction potential, impinging atoms may get trapped temporarily in bound states of this potential[31,39].

After a short lifetime of approximately 10^{-12} s, the He atoms leave the bound state because of interactions with the lattice[62,63]. During this process, the quantum-mechanical phases of the atoms get changed. Hence, these He atoms have a phase shift compared to atoms which have been reflected directly. Due to their otherwise indistinguishability, interference effects result in a modulation of the measured He intensity at certain angular positions[31,64]. Different possibilities for the above mentioned interaction with the lattice when entering or leaving the bound state exist and are described in detail in literature[1,64–66]. Two of them were analysed during the work of this thesis, hence they are specified in the following paragraphs.

In the first case, the trapped He atom interacts with a **G**-vector of the lattice. Then it leaves the surface and interferes with atoms that have been scattered elastically without any temporary bonding to the surface. This process results in intensity modulations of the Bragg diffraction peaks[64]. To measure these effects, usually the incident energy of the He beam is scanned through by varying the nozzle temperature. The kinematic conditions for the occurrence of SAR effects is "moving" through the positions of the Bragg peaks, resulting in the described modulation of intensity. In the experiment, mostly the intensity of the specular peak is probed since higher order diffraction peaks change their angular position when the beam energy is changed.

In the second case, the trapped He atom interacts with a surface phonon before leaving the surface. Subsequently, it interferes with atoms that have been scattered inelastically without any temporary bonding to the surface. The interfering atoms have to be again indistinguishable. Hence, in their interactions they have to create (or annihilate) surface phonons with the same wavevectors and energies. This process results in intensity modulations at angular positions in-between the positions of the Bragg peaks[67,68]. SAR of this type are usually probed with angular HAS scans, where the energy of the impinging

He atoms is held constant while their incident angle is changed.

Although phonons are involved in the second case, their energies and wavevectors are not affecting the kinematic conditions for the resonances. Hence, both effects are referred to as *elastic SAR* or the latter also as *phonon assisted SAR*.

In the described processes, usually a laterally averaged potential in the limit of zero-corrugation (free atom approximation) is assumed and the energy and momentum balance is given in the following way[8,31,39]: The impinging He atom has a wavevector $\mathbf{k}_\mathrm{i}$, which can be split into two components, one parallel ($\mathbf{K}_\mathrm{i}$) and one normal ($k_{\mathrm{i},z}$) to the surface. Due to an interaction with a **G**-vector of the lattice, the kinetic energy of the He atom parallel to the surface is increased from $\frac{\hbar^2}{2m}\mathbf{K}_\mathrm{i}^2$ to $\frac{\hbar^2}{2m}(\mathbf{K}_\mathrm{i}+\mathbf{G})^2$. Having in mind the conservation of energy, the kinetic energy perpendicular to the surface is decreased by the same value from $\frac{\hbar^2}{2m}k_{\mathrm{i},z}^2$ to the energy of the bound state $-|E_n|$. In this model of a laterally averaged potential with zero-corrugation, SARs can be observed if[1,69]

$$E_\mathrm{i} = \frac{\hbar^2\mathbf{k}_\mathrm{i}^2}{2m} = \frac{\hbar^2}{2m}(\mathbf{K}_\mathrm{i}+\mathbf{G})^2 + E_n. \tag{2.54}$$

An illustration for this condition is shown in figure 2.3. If the condition for SAR is fulfilled in the experiment, sharp peaks or dips may be detectable. The appearance of maxima or minima depends on whether the atoms interfere constructively or destructively[31,66]. Although equation (2.54) is accurate enough for most applications, one has to keep in mind that it is an approximation for freely moving atoms. But in fact the He atoms are interacting with the charge density distribution slightly above the surface, which has a non-zero corrugation. Hence, the resonances (bound state energies) are described by a band structure[70,71]. Vargas and Mochán showed, that the free atom model usually results in higher energies than calculations which include a full three dimensional potential[70]. To take this into account, the so called Celli diagrams[72] or full close-coupling calculations[69] may be useful approaches .

However, since for a reasonable consideration of these noteworthy, but rather small influences the necessary resolution is beyond the abilities of the HAS apparatus used, they were neglected in the work of this thesis. Nevertheless, the laterally averaged potential can be determined from the measured bound-state energies and was proven to be a significant and useful result[8,31,69].

2.6.2 Kinematic Focusing

In the angular distribution of a HAS measurement, inelastic peaks in-between the positions of the Bragg peaks may not only arise from SAR effects, but also due to *Kinematic(al) Focusing* (KF). This effect appears if the experimental conditions (k_i, Θ_i) position the scan curve (equation (2.11)) on analytically critical points of the surface dispersion relation, namely on *Van Hove singularities* of the surface phonon density[73,74].

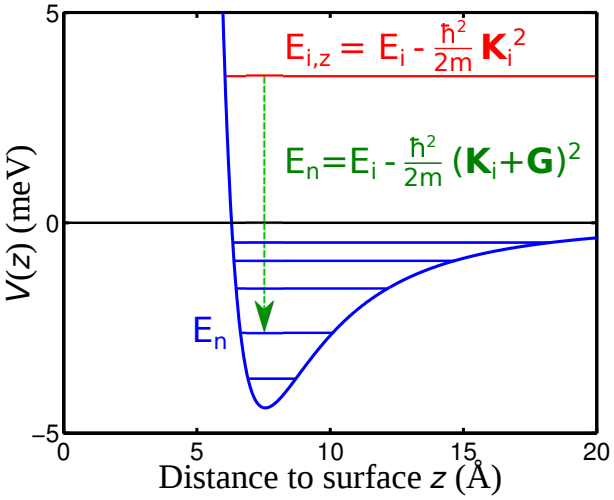

Figure 2.3: Illustration of the condition for SAR within the free-atom approximation. If equation (2.54) is fulfilled, i.e. the normal energy of the He atom matches a bound state (energy E_n), He intensity modulations due to SAR appear. The potential is usually taken to be the lateral average.

Enhanced He beam intensity due to the KF effect is detectable for kinematic conditions in which the scancurve and the dispersion curve are approximately tangent, i.e. they have about the same curvature at their contact point. In the distribution of an angular scan, the inelastic part of the He intensity I is obtained by an integration of the differential reflection coefficient $\frac{d^2R}{d\omega d\Omega}$ along the scancurve (see equation (2.11), $\Delta E = \hbar\omega$, $\omega = \omega_s(K)$)[26]:

$$I = \frac{dR}{d\Omega} = \int_{\omega=\omega_s(K)} \frac{d^2R}{d\omega d\Omega} d\omega \tag{2.55}$$

with $d\Omega$ the acceptance angle of the detector. If only one-surface-phonon processes are considered, equation (2.55) becomes

$$I = \int_{\omega=\omega_s(K)} \frac{\partial\omega_s}{\partial K} A(K)\delta(\omega_s(K) - \omega_d(K))dK. \tag{2.56}$$

$A(K)$ describes the dynamic coupling of the atoms to single surface phonons with energies $E_d = \hbar\omega_d$. By using an expansion of ω_s and ω_d around the point $\overline{K}$ ($\Theta_f = \overline{\Theta}_f$), at which the scancurve is tangent to the dispersion curve, the δ-function in equation (2.56) can be rewritten and

$$I(\Theta_f) = \frac{\overline{v}_d A(K) \tan^{\frac{1}{2}}(\Theta_f)}{\left[\omega_f(1+\frac{k_i}{k_f})(\overline{\Theta}_f - \Theta_f)(\overline{w}_d - \overline{w})\right]^{\frac{1}{2}}} \tag{2.57}$$

is obtained for a fixed $\theta_{SD} \approx 90°$ apparatus[26]. ω_f is the final energy ($E_f = \hbar\omega_f$) and $\overline{v}$ denotes the first, $\overline{w}$ the second derivative of ω with respect to K. Equation (2.57)

shows the inverse square-root singularity. When the scancurve and the dispersion curve have approximately the same curvature ($\overline{w} \approx \overline{w}_{\mathrm{d}}$) at their contact point, the KF effect has a large influence on the intensity in the angular distribution. A scancurve for a special incident angle, at which KF occurs, is plotted as a green curve in figure 2.1. In the analysis of angular HAS measurements, it is important to distinguish between peaks originating from SAR and KF effects. Furthermore, in the early times of HAS, KF effects instead of TOF measurements had been used to determine surface phonon dispersion curves[26]. Although this is not the most practical method, KF effects may still be used as a rough estimation for the surface phonon dispersion or as a verification of theoretically calculated values (see e.g. section 8.4.4).

3 Experimental Setup

All HAS experiments of this thesis were performed on the apparatus H.Å.N.S. (Helium Atom Nondestructive Scattering), which is depicted as a 3-dimensional illustration in figure 3.1. It had been constructed at the FU Berlin, then transfered to Graz, where it was remounted[3]. To characterize the apparatus, first measurements of LiF were performed in 2009[1,3] Several improvements and adaptions[75] succeed in first measurements of the Bi(111) surface[4] and a thorough analysis of its surface dynamics[1,5,6,8,76].

In the following, a short description of the apparatus is given. Further information, a detailed overview of the construction (CAD), the vacuum system and the beam-defining geometry were documented by Anton Tamtögl[1].

3.1 The Source Arm

In the first chamber of the source arm, the He beam is generated by using a supersonic, adiabatic expansion (50 bar $\rightarrow \approx 10^{-6}$ mbar) through a nozzle with a diameter of 10 µm. A skimmer between the first and the second chamber is used to select the central part of the beam. Different skimmers with orifices between 310 and 380 µm were used throughout the work of the present thesis. In the second chamber, a chopper disc can be moved into the beam to perform TOF experiments. As an advantage compared to regular single-slit TOF systems, a pseudo-random chopper disc may be used[75]. Furthermore, in this chamber different apertures with diameters between 0.2 and 3.0 mm can be used to manipulate the spot size of the He beam. To provide the necessary mean free path for the He atoms of the beam, there is a maximum pressure in the region of high-vacuum ($p < 5 \cdot 10^{-6}$ mbar) in all parts of the HAS apparatus.

3.2 The Main Chamber

In the main chamber, the crystal is placed on a six-axes manipulator, which can be used for positioning and rotation of the sample. To avoid contamination of the sample surface, the pressure in the main chamber is in the ultra-high vacuum (UHV) region, namely $p < 2 \cdot 10^{-10}$ mbar. To obtain clean sample surfaces, an Ar^+-ion sputtering system is mounted at the main chamber. Furthermore, the crystal can be heated electrically with a thermocoax and an electrical button heater (HeatWave Labs, UHV Button Heater)

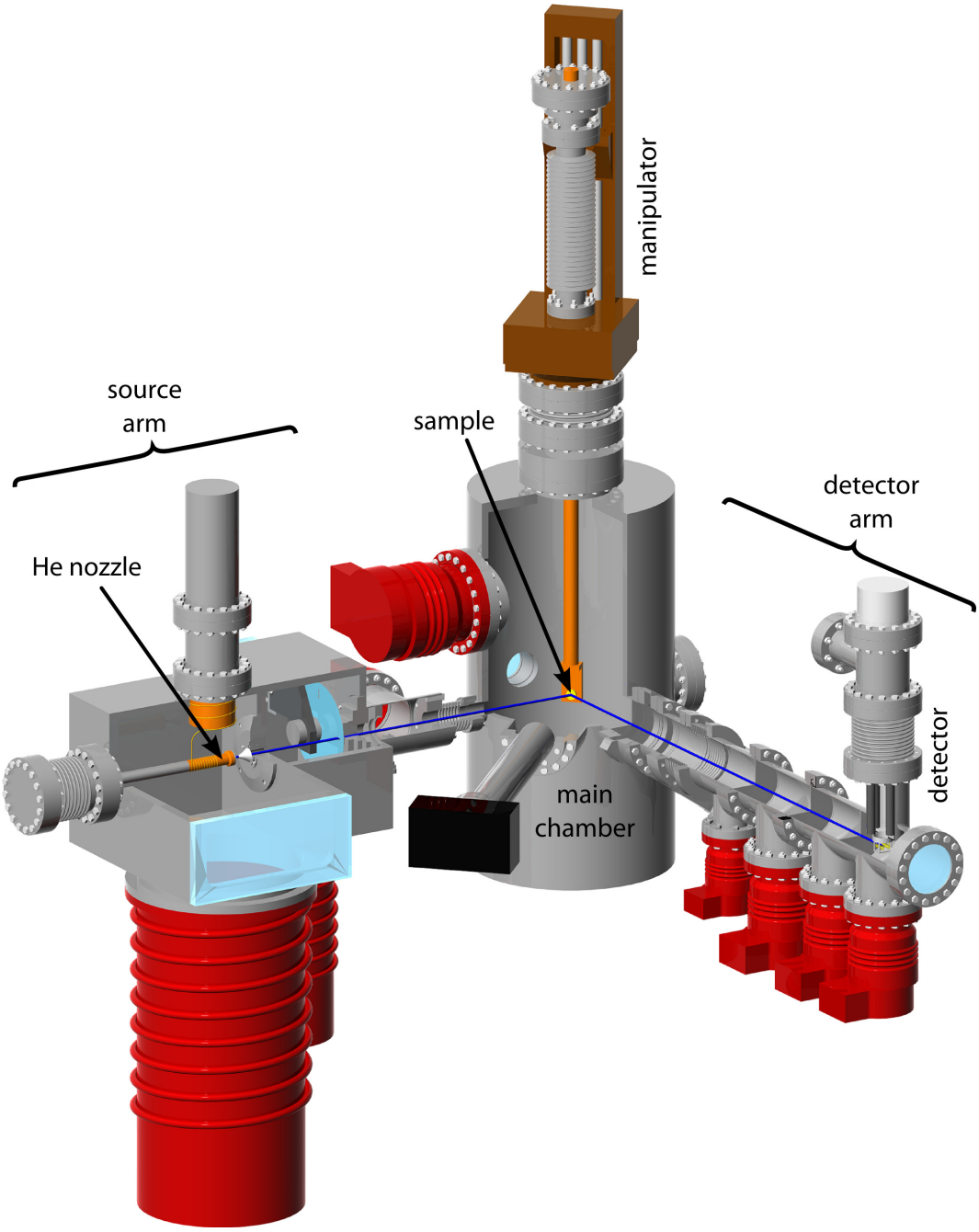

Figure 3.1: 3-dimensional illustration of the HAS apparatus H.Å.N.S., which was used during the work for this thesis. Image taken from[1].

placed directly behind the sample. Cooling of the sample can be achieved by using liquid nitrogen.

The composition of the residual gas can be checked with a quadrupole mass spectrometer. In this chamber, a LEED as well as an AES system are installed to adjust the orientation of the sample and to prove the quality of the surface, respectively. The construction of the apparatus is optimised for *in-plane* scattering measurements, in which the surface normal and the wavevectors of the incident and the detected beam are in one plane. As an important value for the analysis of HAS measurements, the angle Θ_{SD} between source arm and detector arm is fixed, having a value of $\Theta_{SD} = 91.5°$.

3.3 The Detector Arm

To detect the He atoms which are scattered in the direction of the detector arm, a quadrupole mass analyser (QM) is used. It is placed at the end of a differentially pumped vacuum system, which is necessary to distinguish between He atoms scattered directly from the sample surface and particles in the background. For TOF experiments, the QM is also equipped with a multi-channel analyser (MCA) system. To have a very well-defined path length for TOF measurements, the QM-MCA is mounted in cross beam geometry (90° angle between beam and acceleration path of the QM-MCA).

3.4 Additional Characterisation and Monitoring of the Apparatus

In addition to the thorough characterisation documented by Anton Tamtögl[1], in the following supplementary information about the HAS apparatus H.Å.N.S. is provided.

3.4.1 Cool-Down of the Nozzle

The energy of the He beam can be adjusted with the temperature of the He nozzle (see equation (2.1)). A coldhead, which uses the Gifford McMahon-process, is used to cool down the nozzle via oxygen-free copper braids. To obtain a particular nozzle temperature, the nozzle is heated resistively as a counterpart to the cooling. After switching on the coldhead (Leybold RGD510) for the cooling of the nozzle, it takes several hours until the final temperature of the nozzle is reached. The characteristics of the cooling process are shown in figure 3.2. While the second stage of the coldhead reaches a final temperature of 25 K (Si-diode and LTC 60 temperature controller), the minimum achievable nozzle temperature is 47 K (Pt100 resistance thermometer), corresponding to a beam energy of $\approx$ 10 meV. If the temporal characteristics differ significantly from the shown figure, a service of the coldhead should be considered.

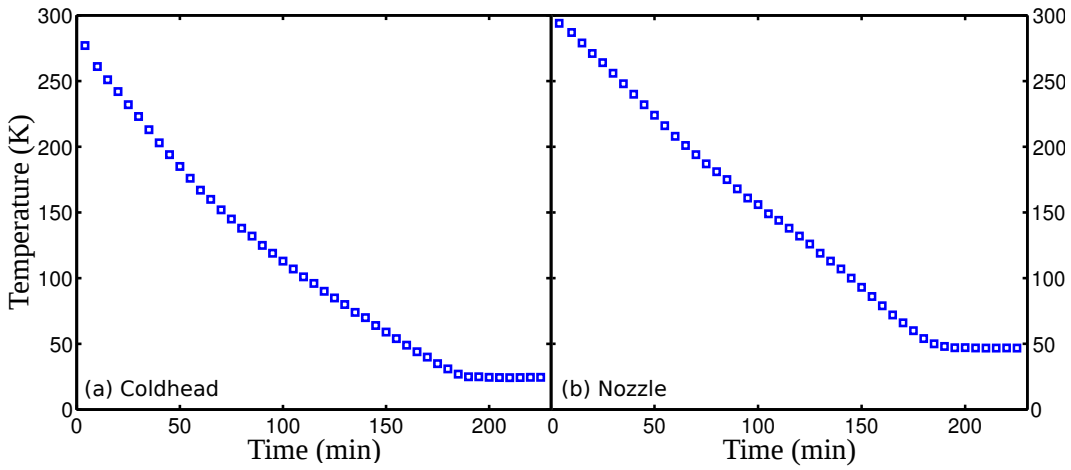

Figure 3.2: Cool-Down of the Nozzle with the installed coldhead. While at the top of the coldhead a final temperature of 25 K is achievable (a), the minimum nozzle temperature is 47 K (b).

3.4.2 Determination of L_{CD}

Since the documentation of the characteristics of the HAS apparatus in[1], the coldhead described in section 3.4.1 was renewed. Hence, it was possible to achieve lower nozzle temperatures, i.e. lower energies of the atoms in the He beam, than documented so far. To experimentally obtain a more accurate path length L_{CD} between chopper and detector, TOF measurements were performed, including these lower temperatures of the nozzle. The velocity v of the He atoms can be calculated by dividing L_{CD} by the flight-time TOF. Furthermore it is given by the temperature of the nozzle T_{N} via the kinetic energy $E_{\mathrm{i}} = \frac{mv^2}{2} = \frac{5}{2}k_{\mathrm{B}}T_{\mathrm{N}}$ (see eq. (2.1)). However, the therewith obtained velocity may have a large error due to the inaccuracy of the temperature measurement. Thus, the exact positions of diffraction peaks in angular HAS measurements were used to calculate v by using eq. (2.23) and eq. (2.4). The flight-time was obtained from Gaussian fits of the detected intensities from elastically scattered He atoms.

These relationships can be used to determine L_{CD} with plotting v over TOF^{-1} as depicted in figure 3.3. The slope of the best linear fit through this data yields the value for L_{CD}:

$$L_{\mathrm{CD}} = (1650 \pm 3)\ mm \tag{3.1}$$

This result is somewhat larger than the length determined in[1] ($L_{\mathrm{CD},1} = (1643 \pm 5)$ mm).

3.4.3 Web Monitoring

The operation and maintenance of a HAS apparatus is often challenging because different influences, such as leakages or power blackouts may affect the UHV, the cooling

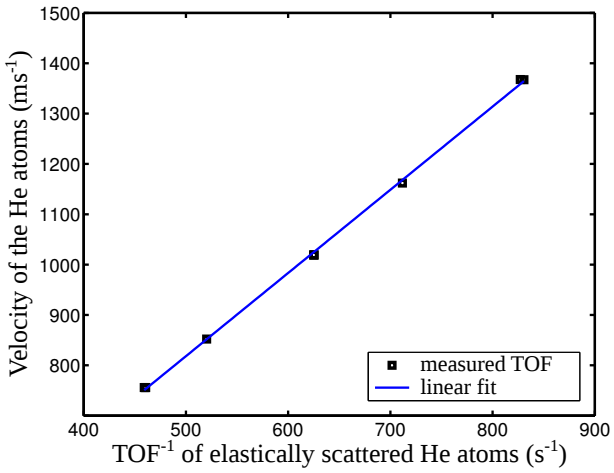

Figure 3.3: Determination of L_{CD} with TOF measurements.

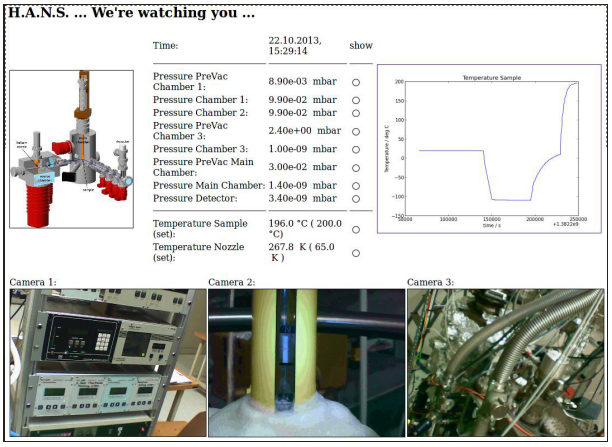

Figure 3.4: Screenshot of the web monitoring interface. The most important pressures and temperatures of the HAS apparatus can be checked on this site.

of the vacuum pumps, the He nozzle or the sample. Furthermore, each TOF measurement during the determination of surface phonon dispersions lasts at least several hours. Therefore, a web monitoring based on an Apache Webserver[77] was developed. All critical pressure values as well as temperatures are recorded every 10 minutes via RS232 and USB interfaces of the controllers. This data and the corresponding graphs can be accessed via the URL http://heliumstreuung.tugraz.at (see figure 3.4) and act as a valuable improvement, especially for measurements with a long duration.

4 Sb(111) and Bi(111)

Both antimony (Sb) as well as bismuth (Bi) belong to the same group 15 (group-V) of the periodic table. Having atomic numbers of 51 (Sb) and 83 (Bi), respectively, spin-orbit interaction has major influence on their (electronic) properties[78–80]. Especially when looking at nanoscale structures, interesting features such as superconductivity or tunable band gap and spin polarisation had been observed recently[81–83]. Furthermore, both materials appear in the compounds of topological insulators, which are promising candidates for applications in future electronics[9,84–86].

In the following sections, an introduction into the main properties of these surfaces with regard to HAS measurements is given. Furthermore, the used cleaning procedures as well as the methods used for the characterisation of the surfaces are presented.

4.1 Structure and Properties of Sb(111)

The structure of bulk antimony (Sb) under standard conditions was investigated for the first time by W. H. Bragg and W. L. Bragg with the technique of X-ray diffraction[87]. R. W. James, N. Tunstall and A. Ogg analysed these results more carefully and were able to number interatomic distances correctly[88,89]. In the second half of the twentieth century, refined investigations improved the accuracy of the lattice constants[90–92]. Nowadays it is known that antimony crystals are built in the rhombohedral A7 (space group $R\bar{3}m$) structure with two atoms per unit cell. In the hexagonal notation, which is the most intuitive choice when focusing on the (111) surface, the lattice constants are a=(4.3084± 0.0002) Å and c=(11.2740± 0.0005) Å at a temperature T=298 K and a pressure p<1 bar[91,92]. Each atom has three nearest neighbours, the distance to the three next nearest neighbours is slightly higher. The main features of this formation are puckered bilayers of atoms with an orientation perpendicular to the ⟨111⟩ direction. Within these bilayers the bonding is of a covalent type whereas the inter-bilayer bonding is of van der Waals character. Due to these weaker inter-bilayer bonds, Sb easily cleaves between two bilayers along the (111) planes[93]. This type of bilayer stacking is a main structural characteristic of the group-V semimetals[6,10,94].

In figure 4.1 a model of the geometric structure of the Sb(111) surface is shown. The corresponding Wigner-Seitz cell and the two high-symmetry directions for the first layer are depicted in figure 4.3. Recent measurements based on photoelectron diffraction[95]

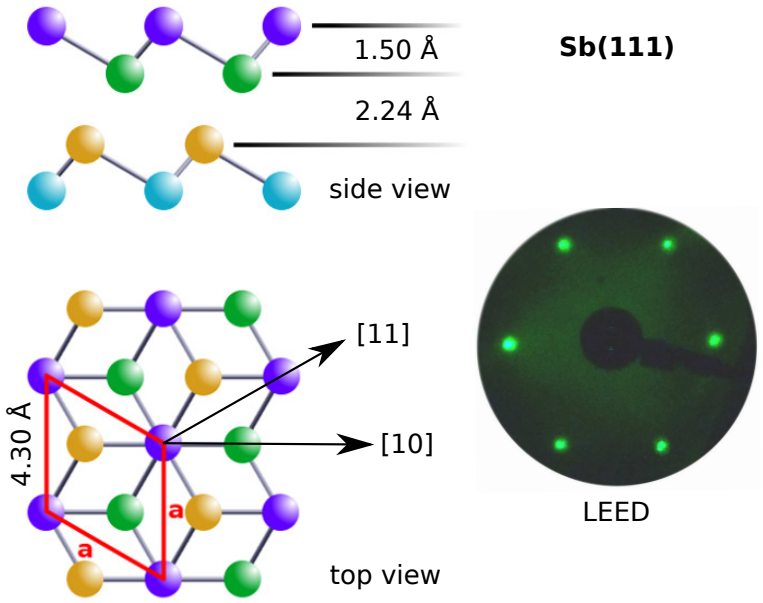

Figure 4.1: Structure of the Sb(111) surface with lattice constants as determined by Bengió et al.[95]. After the cleaning procedure, a LEED beam energy of 38 eV was used to show sharp spots, which exhibit the symmetry of the first layer atoms.

and scanning tunnelling microscopy[93] yielded no substantial relaxations with respect to the bulk. A clear LEED pattern shows the very first layer atoms and is in good agreement with the LEED measurements of Sb(111) reported by Jona[96]. Furthermore, the sharp and intense diffraction spots in the LEED picture are a first indication for the cleanliness of the surface. For scattering experiments, the lattice in reciprocal space is of high importance, hence the bulk Brillouin zone of Sb is depicted in figure 4.2.

The LEED spots also show the arrangement of the surface atoms in reciprocal space, in which Sb(111) also has a hexagonal structure. Figure 4.3 depicts the first Brillouin zone of this surface structure. Furthermore, the two high-symmetry directions are indicated with arrows. All angular HAS scans in this study were performed along one of these directions.

Although bulk Sb has semimetallic properties, there are metallic states on the Sb(111) surface[97,98]. ARPES measurements revealed a central hexagonal-shaped electron pocket in the electronic band structure near the Fermi level. Furthermore, six hole pockets with ellipsoidal shape encircle this electron pocket[97,99].

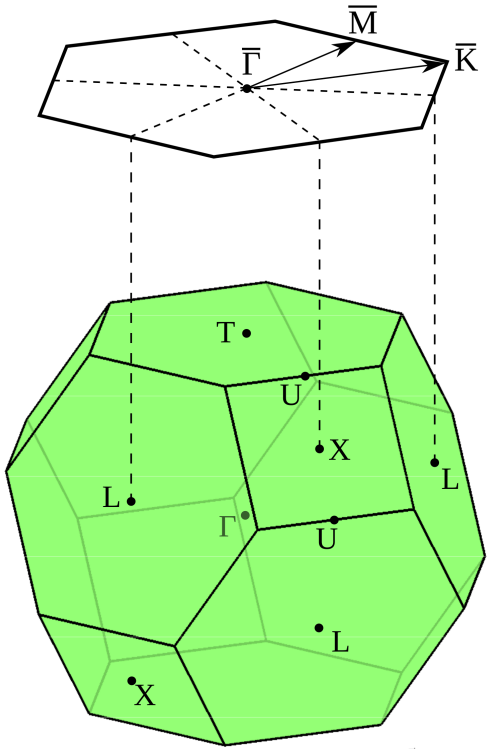

Figure 4.2: Bulk Brillouin zone of Sb in three-dimensional reciprocal space. At this orientation of the crystal, the (111)-surface lies in the horizontal plane. The depicted Brillouin zone is also valid for Bi.

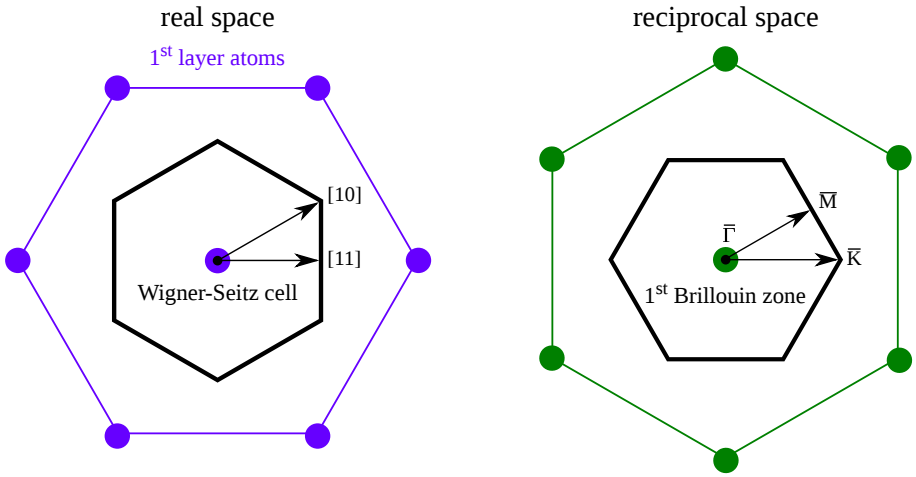

Figure 4.3: Surface Wigner-Seitz cell and Brillouin zone of Sb(111) in two-dimensional real and reciprocal space together with the two high-symmetry directions. The direction $\overline{\Gamma M}$ in reciprocal space is equivalent to the direction [10] in real space, $\overline{\Gamma K}$ corresponds to [11]. The depicted illustration is also valid for Bi(111).

4.1.1 Characterisation of the clean Sb(111) Surface

In HAS measurements, the cleanliness of the sample surface is of high importance, since impurities distort the detected signal significantly. While a first indication of a clean surface are the sharp LEED spots as depicted in figure 4.1, a more thorough characterisation of the clean Sb(111) surface was obtained with AES measurements.

Due to the manufacturing process, the antimony sample crystal is initially contaminated by carbon. In figure 4.4(a) the AES result for the as-received Sb crystal is shown. In addition to the carbon signal at 272 eV, a peak originating from an intrinsic oxygen layer is clearly visible at 510 eV. The found contaminations are in agreement with an investigation by Shan et al.[100], who investigated the adsorption of water on Sb(111) and preliminarily performed AES measurements of their samples.

Ar^+-ion sputtering (1.7 kV, 3 μA/cm^2, 15 min) and annealing at 470 K for up to twelve hours was used to obtain a clean sample surface. Although the oxygen peak vanished after just one application of the cleaning procedure (see figure 4.4(b)), for a chemically clean surface at least three repetitions of the cleaning cycle are indispensable (see figure 4.4(c)). The positions of the measured dips (334, 342, 388, 440, 454, 462, 492 and 499 eV) are in good agreement with the data from an AES standard handbook[101].

4.1.2 Surface Steps and Terrace Height of Sb(111)

The investigations of the height of surface steps and the terrace distribution were part of the publication presented in chapter 6 and can be found in detail in section 6.3.3.

4.2 Structure and Properties of Bi(111)

Bismuth (Bi) crystallises in the same rhombohedral A7 structure as antimony[80]. The structural parameters of the Bi(111) surface had been determined by Mönig et al. with LEED measurements and *ab-initio* calculations[103]. In figure 4.5, the Bi(111) surface with the most important lattice constants is shown, figure 4.3 shows the Wigner-Seitz cell and the first Brillouin zone with the two high symmetry directions. Due to the weaker inter-bilayer bonding, Bi easily cleaves between two bilayers along the (111) planes[80].

A more detailed description and investigations of the Bi(111) surface can be found in the PhD thesis of Anton Tamtögl[1] and the corresponding publications[4–8]. Additionally, the results of the investigation of the surface step height and distribution at Bi(111) is presented in the following section.

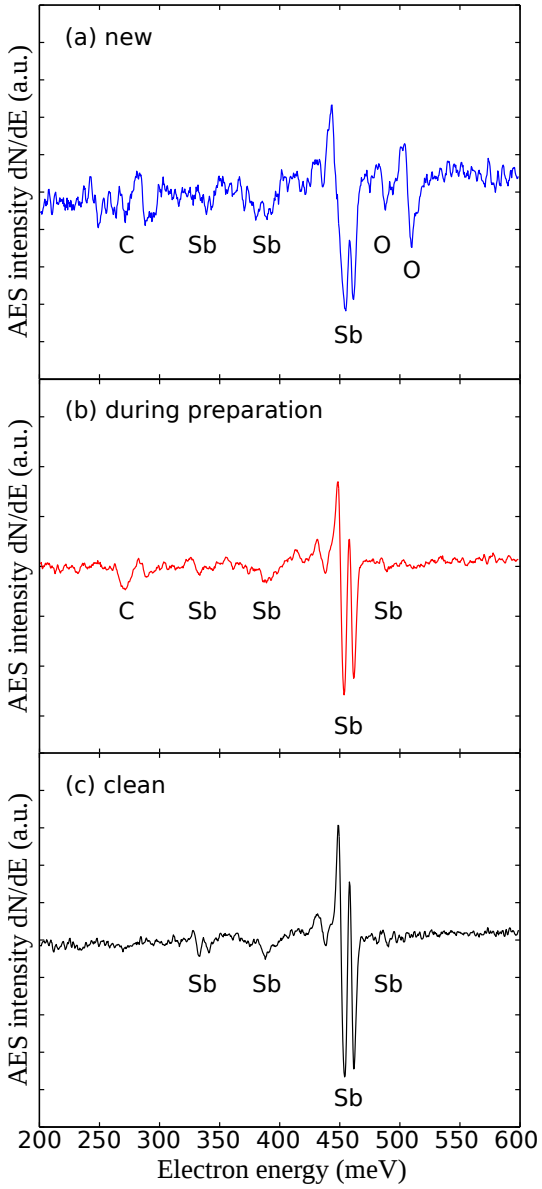

Figure 4.4: AES spectra of the Sb(111) sample crystal. (a) Spectrum of the crystal as received from Metal Crystals & Oxides Ltd[102]. Oxygen and Carbon contaminations are clearly visible. (b) AES spectrum after one cleaning cycle (Ar^+ ion-sputtering + annealing). (c) The spectrum of the clean Sb(111) sample crystal as obtained after several cycles of sputtering and annealing. The cleanliness of the samples were checked before and after every HAS measurement.

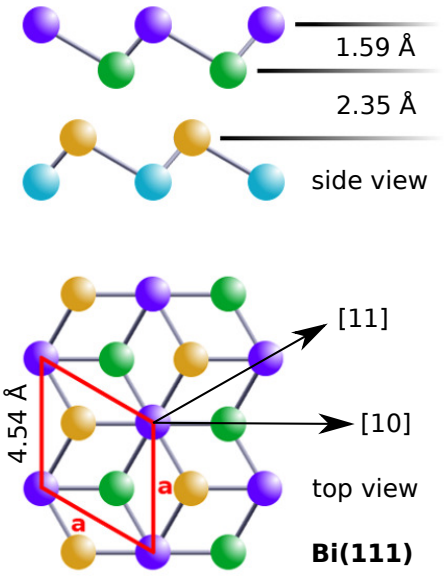

Figure 4.5: Structure of the Bi(111) surface with lattice constants as determined by Mönig et al.[103].

4.2.1 Characterisation of the clean Bi(111) Surface

Because of the simple cleaving along the (111) planes, Bi(111) crystals are commercially available easily. The crystals, which were investigated during the work of this thesis, had been bought from Metal Crystals & Oxides Ltd[102]. Ar^+-ion sputtering (1.5 kV, 2 μA/cm^2, 15 min) and annealing at 420 K for up to twelve hours was used to obtain a clean sample surface. The purity of the Bi(111) crystals was checked with X-ray photoelectron spectroscopy (XPS)[1,4,5]. A description of this method can be found in the PhD thesis of Anton Tamtögl[1].

4.2.2 Surface Steps and Terrace Height of Bi(111)

As described in section 2.5.4, the surface step height and the distribution of terraces can be determined from HAS measurements. Thereto, the He intensity of the specular peak is measured while changing the incident energy of the He atoms with tuning the nozzle temperature. With this procedure the wavevector transfer Δk_z normal to the surface can be varied, resulting in a modulation of the specular intensity. By using equation (2.53) and the inclusion of the Debye-Waller attenuation as well as the nozzle temperature dependence of the He intensity, the expected He intensity can be modelled.

In figure 4.6(a) the result of the best-fitting calculation together with the normalised measured intensity is shown. The increasing difference between the theoretically and experimentally obtained values for decreasing wavevector transfer is due to the influences of SAR (see section 2.6.1) at low incident beam energies. The positions of the strongest

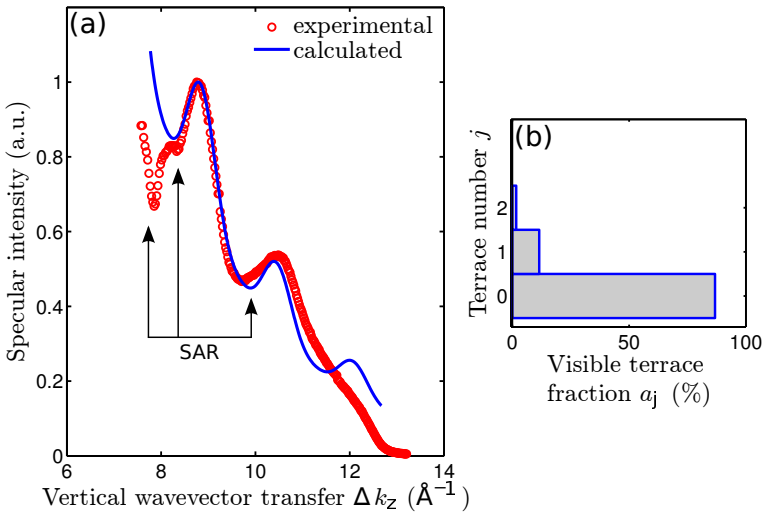

Figure 4.6: (a) Specular intensity as a function of the vertical wavevector transfer Δk_z of the He beam for the Bi(111) surface. The measurement was performed along the $\overline{\Gamma M}$ azimuth while the crystal was kept at a temperature of 123 K. The experimental data points (open red circles) were fitted using equation (2.53) for values between 7.8 and 13 Å^{-1} (solid blue line). The positions of recently determined positions of SAR effects[8] are indicated by black arrows. (b) The distribution of the terraces as obtained from the best fit result.

SAR had been calculated recently[8] and are indicated in the figure. Deviations for high values of the incident beam energy originate from a bad adjustment of the nozzle, which occurs during the heating of the nozzle and always is a challenging task for such a large range of nozzle temperatures. Nevertheless, the model is able to reproduce the measured values in the region between 8 and 11.5 Å^{-1} very well. The surface step height determined from the fit is $h = (3.9 \pm 0.1)$ Å, which is in good agreement with the step height of a bilayer (3.94 Å, see figure 4.5) determined from experiments[80,103] and recent DFPT calculations[6]. The distribution of terraces, figure 4.6(b), shows that the Bi(111) surface seems to be quite flat, although these results should be considered with care because of the simplicity of the model.

A detailed description of the fitting procedure can be found in section 6.3.3, in which the investigation of surface steps and terrace heights of Sb(111) is presented.

5 Vibrational dynamics and surface structure of Bi(111) from helium atom scattering measurements

The following corresponds to a publication by
Michael Mayrhofer-Reinhartshuber, Anton Tamtögl, Patrick Kraus, Karl-Heinz Rieder and Wolfgang E. Ernst in *Journal of Physics: Condensed Matter*, **24**:104008-1-6, February 2012[5].

The author of this thesis was responsible for

- the main parts of the angular HAS measurements with the Bi(111) sample crystal cooled down with liquid nitrogen,
- the main parts of the temperature-dependent HAS measurements of Bi(111) (see figures 5.2 and 5.5),
- the analysis of the corrugation with the GR method (see table 5.1 and figures 5.3 and 5.4),
- and the authorship of the abstract and sections 5.1.1, 5.3.1, 5.3.2, and 5.4.

The contributions of the co-authors are listed below:

- A. Tamtögl: Introduction, HAS-measurements, Implementation of the Eikonal-Method, DW-analysis
- P. Kraus: HAS-measurements, Check of the implemented algorithms
- K.-H. Rieder: Bismuth: preparation and properties, Help with the implementation of the Eikonal-Method
- W.E. Ernst: supervision (experiment, theory, publication), laboratory, funding

Abstract

The Bi(111) surface was studied by elastic scattering of helium atoms at temperatures between 118 K and 408 K. The observed diffraction patterns with clear peaks up to third order were used to model the surface corrugation using the eikonal approximation as well as the GR-method. Best fit results were obtained with a rather large corrugation height compared to other surfaces with metallic character. The corrugation shows a slight enhancement of the surface electron density in between the positions of the surface atoms. The vibrational dynamics of Bi(111) were investigated by measurements of the Debye-Waller attenuation of the elastic diffraction peaks and a surface Debye temperature of (84 ± 8) K was determined. A decrease of the surface Debye temperature at higher temperatures that was recently observed on Bi nanofilms could not be confirmed in the case of our single crystal measurements.

5.1 Introduction

The semimetal bismuth (Bi) has attracted increasing interest accompanied by the discovery of a phase transition in Bi that occurs at the quantum limit and involves electron pockets which host Dirac electrons[104]. For an explanation of the transition to a metal, the Bi(111) surface plays a central part since it is a much better metal than the bulk due to the presence of metallic surface states[80,105,106]. Bi surfaces are frequently mentioned as prime candidate to study the quantum size effect in solids[80,105,107] and superconductivity of Bi cluster films, nanowires and Bi bicrystals has been observed[81,82,108,109]. Apart from the fact that the strong spin-orbit interaction in Bi is challenging from a theoretical point of view, it is a promising property of Bi surfaces and interfaces with respect to applications in spintronics[80].
Helium atom scattering (HAS) experiments are of particular interest on Bi surfaces as the diffraction patterns do not only contain information about the geometrical positions of the surface atoms but also about the electronic structure since the impinging helium atoms are scattered at the surface electron density and thus provide a mapping of the electron density. Furthermore, the properties of He atom scattering are ideal for the investigation of the dynamics of inelastic processes. Thereby the vibrational dynamics of the surface atoms give rise to a thermal attenuation of the scattering peaks which allows the determination of the surface Debye temperature[35,39,110].

5.1.1 Structure and Properties of Bi(111)

Bismuth crystallizes in the rhombohedral A7 structure. The major characteristics of this structure are the puckered bilayers of atoms arranged perpendicular to the [111] direction. Within those bilayers the bonding is much stronger than in between, where

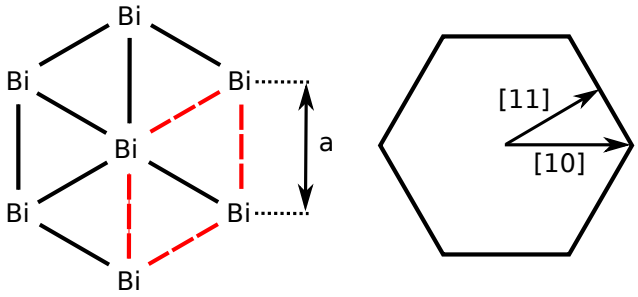

Figure 5.1: Top view of the Bi(111) surface structure showing the 1^{st} layer together with the two scattering directions. The dashed rhombus indicates the unit cell with a lattice constant of $a = 4.538$ Å [103].

the bonds have more of a van der Waals character. Due to those weak bonds the crystal is easily cleaved along the [111] direction.

The first LEED patterns of the Bi(111) surface were presented by Jona[96]. Mönig et al.[103] investigated the detailed structural parameters using LEED and ab-initio calculations and displayed that the only relaxation at the surface is a small deviation of the interlayer distances from the bulk values. Besides the rhombohedral structure, Bi can also be described by a pseudocubic or a hexagonal structure. The latter one is the natural choice when describing the Bi(111) surface since it describes its first layer in an intuitive way. The unit cell in this notation is highlighted in figure 5.1. The sixfold symmetry of the surface structure described by first layer atoms is reduced to threefold symmetry if second layer atoms are included. However, with the applied energies in our HAS experiments influences of other than first layer atoms are negligible. Both the $\langle 10 \rangle$ and the $\langle 11 \rangle$ direction can be treated as mirror planes. Most of the previous experiments on the Bi surfaces focused on photoemission studies[78,105–107,111–114]. A very interesting aspect of the previous outcomes is that the number of surface charge carriers is much higher than the corresponding number of bulk carriers[80]. For this reason, the surfaces of Bi are a far better metal than the bulk. This can be explained in terms of the strong spin-orbit splitting occurring in Bi[78].

5.2 Experimental Details

The experimental work of this study was conducted using a HAS apparatus with a 91.5° source-target-detector geometry. A nearly monochromatic He beam was generated in a supersonic expansion of helium through a 10 μm nozzle and the central part of the beam was then selected using a 310 μm skimmer. The whole apparatus has been described in greater detail in a previous publication[4].

The Bi(111) single crystal used in this study was a disc with a diameter of 15 mm and

a thickness of 2 mm. The crystal was mounted on the sample holder which can be heated resistively using a button heater. The sample temperature was measured using a chromel-alumel thermocouple. Prior to the measurements the surface was cleaned by Ar^+ sputtering (1.5 kV, 2 μA) and annealing to 423 K. After this treatment no surface contamination could be detected with XPS.

5.3 Data and Results

5.3.1 Elastic Scattering

For the Bi(111) surface with its sixfold symmetry of the very first layer there are two low-index, namely the $\langle 10 \rangle$ and the $\langle 11 \rangle$, directions which are shown in figure 5.1. They exhibit periodic structures with spacings of $1/2a$ and $\sqrt{3}/2a$ with the lattice constant $a = 4.538$ Å[80]. Angular HAS-scans were performed along these directions after the azimuthal orientation of the sample had been adjusted using LEED. It was already shown in our previous work that scattering of HAS on Bi(111) gives rise to sharp diffraction peaks. However, those measurements were carried out with the crystal at room temperature and only first order diffraction peaks could be observed[4]. By cooling the sample down to a temperature of 123 K and using incident energies of $E_i = 31.7$ meV ($\langle 10 \rangle$ azimuth) and $E_i = 24.1$ meV ($\langle 11 \rangle$ azimuth) of the helium beam diffraction patterns with peaks up to third order were observable. They are depicted in figure 5.2 as a function of the incident angle with the zero-order diffraction peak at $\theta_i = 45.75°$.

The positions of the peaks are in excellent agreement with the already known structure of the top-most layer as obtained by Mönig et al.[103]. As an advantage of the cooling, much higher intensities compared to the measurements with the sample at room temperature could be achieved. There is a slight asymmetry in the angular scans which is likely to be caused by steps in the Bi(111) surface[115] and alignment problems.

As already pointed out by Tamtögl et al.[4] a large fraction of the scattered He atoms is found in the diffraction peaks which is unusual for a surface with metallic character. Considering the reported metallic character of the surface one would expect a smoothening of the contour due to the Smoluchowski effect[37], yet the large diffraction peaks imply an increased importance of the surface corrugation for HAS on Bi(111) compared to other metals. To provide a more thorough investigation of this effect we have carried out a detailed analysis of the diffraction peak intensities.

5.3.2 The Surface Corrugation

In order to determine the corrugation of the He-Bi(111) surface interaction potential, diffraction intensity calculations based on the hard corrugated wall model were performed. We have used the assumptions of the eikonal approximation[35,39] as well as

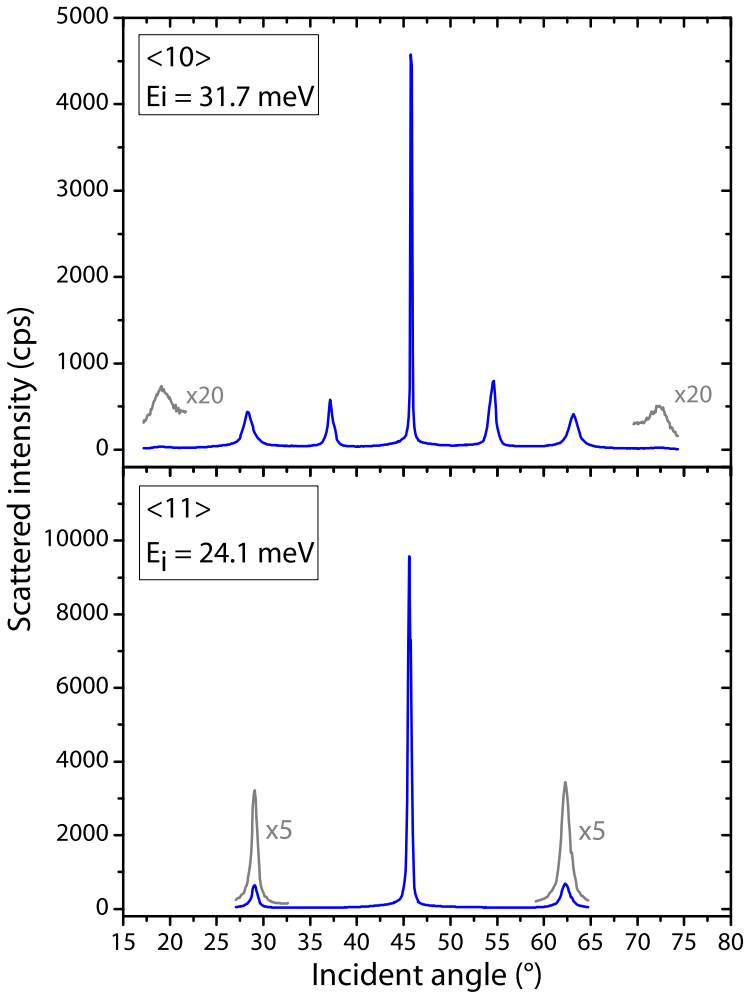

Figure 5.2: Scattered intensity of He vs. incident angle for He diffracted from Bi(111) along the ⟨10⟩ azimuth (upper part) and along the ⟨11⟩ azimuth (lower part). The crystal has been cooled down to 123 K.

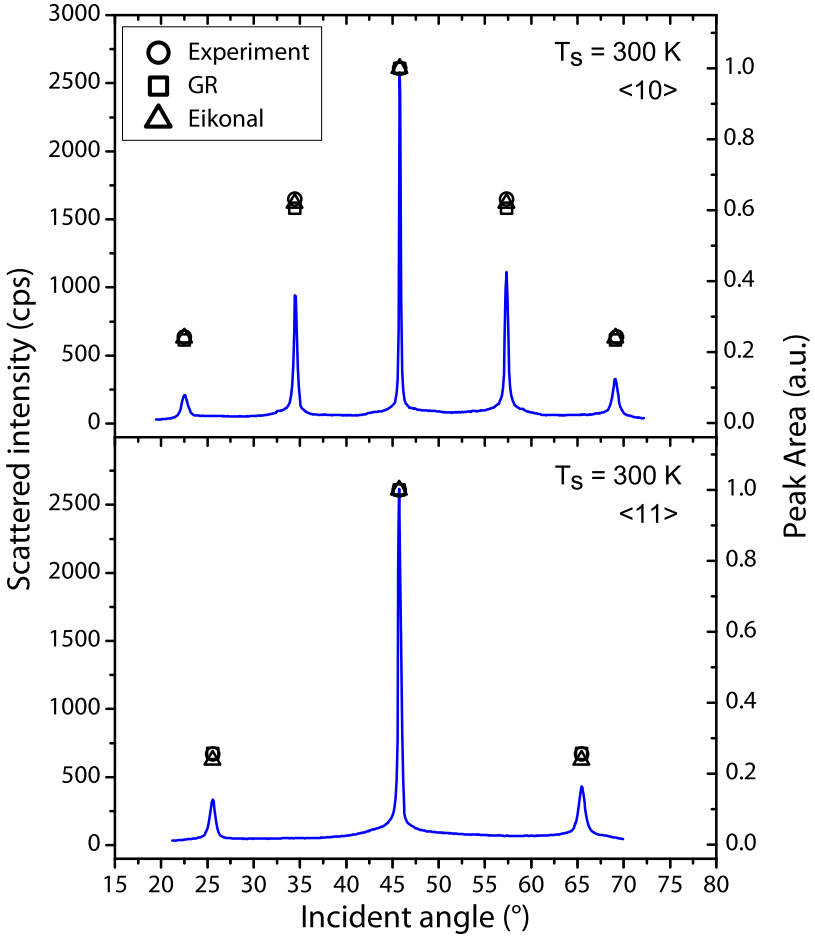

Figure 5.3: Scattered intensity of He vs. incident angle for He diffracted from Bi(111) along the $\langle 10 \rangle$ and $\langle 11 \rangle$ azimuth for $E_i = 17.7$ meV. The shown measurements were performed with the crystal at 300 K. The circles correspond to the experimentally determined peak areas, the triangles indicate the calculation using the eikonal approximation and the squares show the results using the GR method.

the GR-method[43,45]. The surface was modeled using the simple two-parameter Fourier ansatz for the surface corrugation function

$$\begin{aligned}\xi(x,y) = \quad & \xi_{01} \cdot \left(\cos\left[\tfrac{2\pi}{a}\left(x - \tfrac{y}{\sqrt{3}}\right)\right] + \cos\left[\tfrac{2\pi}{a}\left(x + \tfrac{y}{\sqrt{3}}\right)\right]\right) \\ & + \xi_{01} \cdot \cos\left[\tfrac{2\pi}{a} \cdot \tfrac{2y}{\sqrt{3}}\right] + \xi_{11} \cdot h.o. \end{aligned} \tag{5.1}$$

with x and y being rectangular coordinates with respect to the oblique geometry of the surface and $h.o.$ corresponding to higher order Fourier terms. Hard wall intensities were calculated for various ξ_{01} and ξ_{11} and compared to the relative experimental diffraction possibilities. The best-fit coefficients have then been determined by varying the amplitudes ξ_{01} and ξ_{11} until optimum agreement between the measured and the calculated intensities was reached. The accuracy of the agreement is usually judged by evaluating a reliability factor R[39]:

$$R = \frac{1}{N}\sqrt{\sum_G \left(P_G^{exp} - P_G^{calc}\right)^2} \tag{5.2}$$

where N denotes the number of experimentally observed diffraction peaks, and P_G^{exp} and P_G^{calc} are the experimental and calculated diffraction intensities for each G which have been normalized by dividing by the intensity of the specular peak. The fitting procedure has been applied to angular HAS scans with the Bi crystal at room temperature and cooled down to 123 K to account for dynamic effects that may be related to the structure. As shown by Conrad et al.[55] and certified by Farias and Rieder[39] this approach for fitting hard wall corrugation functions is sufficiently accurate. Figure 5.3 shows the corresponding angular scans along the $\langle 10 \rangle$ and the $\langle 11 \rangle$ azimuth with a beam energy $E_i = 17.7$ meV.

For comparison with the calculated intensities the experimental peak areas were determined. The reason for using the peak areas is due to the broadening of the elastic peaks caused by the energy spread of the He beam and a broadening caused by the apparatus and the domain size of the crystal surface[116,117]. Therefore the elastic peaks were fitted with two Gaussian functions to account for the narrow coherent elastic contribution and for the broad diffuse elastic and multiphonon contribution[47]. The area of the narrow coherent elastic peaks was then compared with the calculations. The asymmetries in the measurements were attributed to a poor alignment. Peak areas of corresponding peaks were averaged. In figure 5.3 the peak areas are indicated as circles while the solid curves show the experimental count rates versus incident angle. Figure 5.3 also shows the calculated intensities obtained by the eikonal approximation, indicated by the triangles and those obtained by the GR method designated by the squares.

To account approximately for the attractive well near the surface, the Beeby correction has been applied in the calculations[39]. In both cases (GR and eikonal approximation), a Beeby correction of 8 meV was found to provide a good fit. The best fits to the data

Table 5.1: Best fit corrugations in percent of the lattice constant a corresponding to the experimental measurements at $T_S = 123$ K and $T_S = 300$ K obtained with the eikonal approximation and the GR method by modeling the surface with the Fourier ansatz (5.1). All calculations were performed with the Beeby correction ($D = 8$ meV).

	R-factor (%)		corr. height/a (%)	
T_S (K)	Eikonal	GR	Eikonal	GR
123	4.0	2.8	10.6	9.7
300	1.6	1.4	11.2	10.1

are summarized in table 5.1 with the reliability factor according to (5.2) and the peak-to-peak corrugation in percentage of the surface lattice constant a. The experimental results agree well with the calculations, in terms of R the deviation is smaller than 2.8% for the GR method and smaller than 4.0% using the eikonal approximation. However, it should be mentioned that the application of the eikonal approximation for such a large corrugation should be treated with caution whereas the GR method has proven its reliability for corrugations as large as $0.18a$[39].

In a first estimation Tamtögl et al.[4] obtained a corrugation height of 16% of the lattice constant for the crystal at room temperature. In the presented analysis we find a corrugation of ≈10% which is smaller than the previous value. However, in the first estimation by Tamtögl et al. the Beeby correction was neglected, which would imply a larger corrugation, and the inclusion of higher order diffraction peaks in our calculations should give rise to a more accurate result. Nevertheless the tendency towards a large corrugation for scattering of He on Bi(111) has been confirmed since a peak to peak corrugation of $0.10a$ is still large for a surface which exhibits a metallic character. The observed corrugation of the electron density is by no means expected at a metal-like surface[112].
In figure 5.4 a surface plot together with a density plot of the best fit corrugation is shown. At a closer look it is quite remarkable that a linearly shaped enhancement of the electron density between the positions of the Bi atoms seems to appear. This is not due to any contribution of atoms in the second layer since the interaction of He atoms with the second layer can be neglected for an incident energy of 17.7 meV. Therefore it would be interesting to perform ab-initio calculations of the surface electron density of Bi(111) and derive the corresponding diffraction probabilities.
Furthermore it should be mentioned that the calculation of the corrugation shows a slight increase of the corrugation height with increasing surface temperature. While this tendency is still within the uncertainty of the calculations both calculation methods, the eikonal approximation as well as the GR method show the same trend. However,

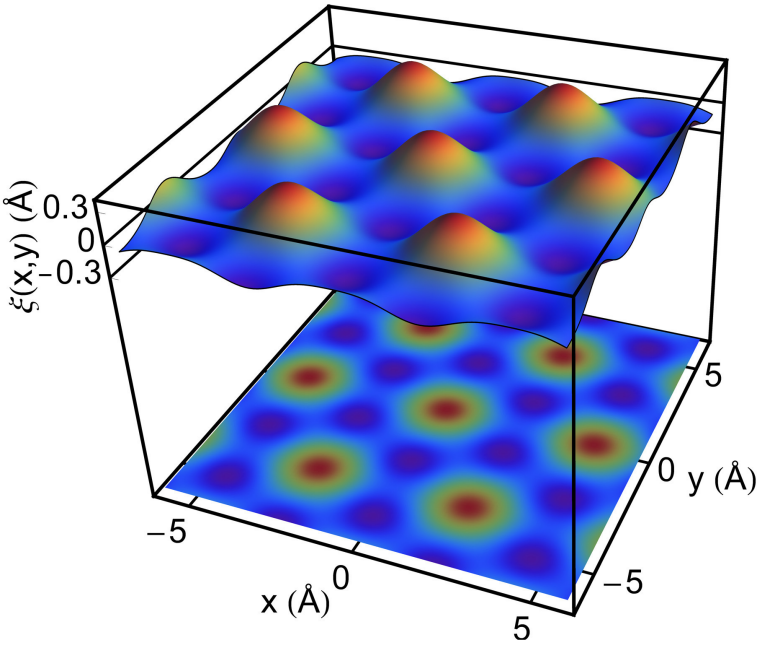

Figure 5.4: Plot of the hard-wall potential surface for the Bi(111) surface at an incident energy of $E_i = 17.7$ meV and a temperature of 300 K. The corrugation was obtained by fitting the observed helium diffraction intensities within the eikonal approximation. The peak to peak amplitude is 0.51 Å.

this effect could also be caused by a slight difference in the Debye temperatures of the diffraction peaks[39,55]. Hence if this tendency is of any physical meaning it should also give rise to a signature in the inelastic scattering of He from Bi(111).

5.3.3 Surface Debye Temperature of Bi(111)

The thermal attenuation of the diffraction peaks provides insight into the surface vibrational dynamics[39]. Figure 5.5 shows the decay of the specular peak intensity with increasing surface temperature T_S. Therefore scans of the scattered intensity around the zero order peak were collected for an incident energy of $E_i = 17.7$ meV while the Bi surface temperature was varied between 118 K and 408 K.

The thermal attenuation of the diffraction peak intensities is caused by vibrations of the surface atoms giving rise to inelastic scattering of the incoming atoms. This attenuation is described by the Debye-Waller factor which relates the diffraction intensity $I(T_S)$ of a sample at surface temperature T_S to the intensity I_0 of a sample at rest by

$$I(T_S) = I_0 \cdot e^{-2W(T_S)} \tag{5.3}$$

where $\exp[-2W(T_S)]$ is the Debye-Waller factor[39]. Assuming that the momentum trans-

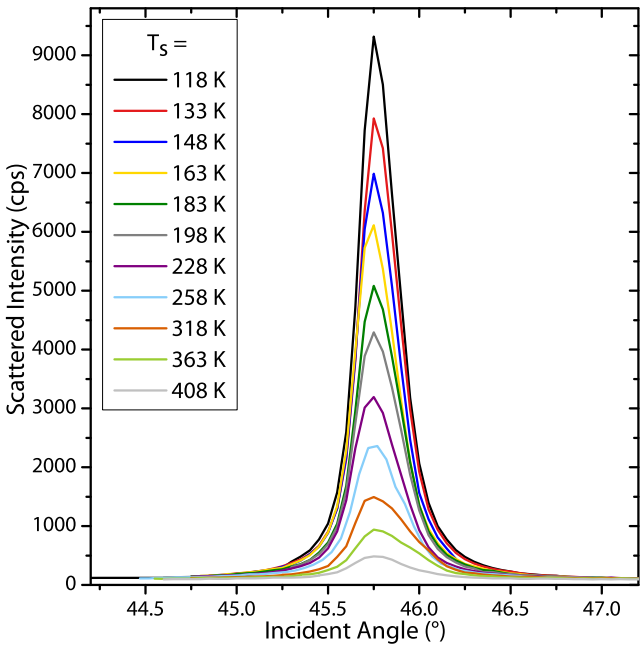

Figure 5.5: Plot of the attenuation of the specular peak with increasing surface temperature T_S of the Bi(111) sample. The scattered intensity of the helium beam with an incident energy of $E_i = 17.7$ meV is shown.

fer parallel to the surface equals zero, a reasonable approximation of the Debye-Waller factor is obtained:

$$2W(T_S) = \langle u_z^2 \rangle \cdot (\Delta k_z)^2 \tag{5.4}$$

where $\langle u_z^2 \rangle$ describes the average displacement of a crystal atom perpendicular to the surface and Δk_z is the momentum transfer during the scattering process. For a classical harmonic oscillator within the Debye model, $W(T_S)$ becomes

$$W(T_S) = \frac{3(\hbar^2 \Delta k_z^2) T_S}{2 M k_B \theta_D^2} \tag{5.5}$$

where M is the mass of the surface atom and Θ_D the surface Debye temperature[27,39]. Furthermore, the effect of the attractive well near the surface which gives rise to an additional acceleration perpendicular to the surface can be taken into account using the Beeby correction[39,47]. The influence of the attractive well is considered by replacing the momentum transfer Δk_z by

$$\Delta k_z^* = k_i \left[\sqrt{\cos^2(\theta_f) + \frac{D}{E_i}} + \sqrt{\cos^2(\theta_i) + \frac{D}{E_i}} \right] \tag{5.6}$$

with D the well depth of the potential. In the case of the specular beam, $\theta_i = \theta_f$ holds and the Debye Waller factor (5.5) together with the Beeby correction (5.6) can be

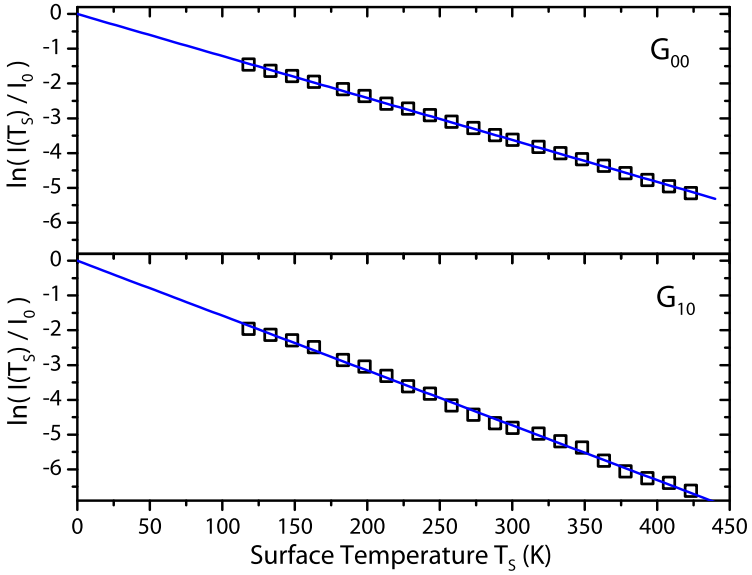

Figure 5.6: Decay of the specular and first order diffraction peak intensity $I(T_S)$ versus surface temperature T_S for an incident beam energy $E_i = 17.7$ meV. In both cases the natural logarithm of $I(T_S)/I_0$ exhibits a linear slope.

expressed as

$$W(T_S) = \frac{12m\left[E_i \cos^2(\theta_i) + D\right] T_S}{M k_B \theta_D^2} \tag{5.7}$$

where m is the mass of the impinging particle. Although (5.7) is strictly valid only for the specular beam, it is also a reasonable approximation for final angles θ_f that are not too different from the incident angle θ_i[39].
According to (5.3) and (5.4) a plot of $\ln(I(T_S)/I_0)$ versus the surface temperature T_S gives rise to a linear decay within the Debye model whereupon the surface Debye temperature can be calculated from the slope. In figure 5.6 the decay of the specular and the first order diffraction peak intensity versus temperature are depicted. Both measurements have been carried out at an incident beam energy $E_i = 17.7$ meV.

The experimental data perfectly fits a linear decay over the experimental range consistent with the Debye model. The intensity of the first order diffraction peak shows small deviations which could be the effect of a slightly misaligned symmetry axis due to elongation effects when cooling down the sample with liquid nitrogen. From the linear fit of the experimental data we obtain a slope of $-12.1 \cdot 10^{-3}$ K^{-1} for the decay of the specular peak intensity and $-15.8 \cdot 10^{-3}$ K^{-1} for the first order diffraction peak. Using (5.5) - (5.7) one can calculate the surface Debye temperature θ_D from the slope if the mass of the helium atom scatterer M and the potential well depth D is known. For He atom scattering D is typically in the range of $5 - 8$ meV[66]. We assume a value of

$D = 8$ meV for the calculation of the Debye temperature which is motivated by the enhanced metallic character of the Bi(111) surface which in turn should give rise to a considerable well depth[118,119]. This value was also found to provide a good fit for the calculations of the surface corrugation. Also investigations of selective adsorption resonances and a determination of the He-Bi(111) interaction potential confirmed this value[8].

With M equal to the mass of a single Bi atom, the Debye temperature θ_D was determined to be (84 ± 8) K from the measurements of the specular peak and (75 ± 8) K from the measurements of the first order peak. Hence the surface Debye temperature of Bi(111) is reduced significantly with respect to the bulk value which is 120 K[120,121]. This is in good agreement with the theoretical approximation of van Delft[122] that estimates a reduction of the surface Debye temperature by a factor of $1/\sqrt{2}$ with respect to the bulk value.

Even though the determination of the surface Debye temperature using LEED measurements usually includes the measurement of scattered electrons that are penetrating into the first layers of the bulk, we will try to compare the LEED results with our HAS measurements. Compared to Mönig et al.[103] who determined a surface Debye temperature of Bi(111) with $\theta_D = 71(+7/-5)$ K for the first layer using LEED experiments, our value is slightly larger. Considering collisions of the impinging helium atom with more than one surface atom due to the cooperative motion of the surface atoms would give rise to a helium scatterer mass M greater than that of a single Bi atom and consequently a lower θ_D[123,124]. However, the uncertainty in our calculation of the Debye temperature results primarily from the well depth D.

Yaginuma et al.[125] reported a decrease of the surface Debye temperature above 350 K which they attribute to a softening transition of the outermost interbilayer bonds accompanied by a hardening of the topmost intrabilayer bonds. Their experimental findings appear when determining the surface Debye temperature of a bismuth nanofilm that adopts the same structure as the bulk truncated Bi(111) surface using LEED. Thereby θ_D decreases from 76 K to 50 K for $T_S > 350$ K[125]. However, in our measurements there is no evidence for such a drop in the surface Debye temperature. The fact that we are not able to observe this transition in our measurements of the bulk truncated surface may be caused by different properties of the nanofilm or a signature of the substrate. However, it has been shown that the nanofilm surface takes the same atomic configuration with a lattice constant that is almost the same as the one of the bulk truncated surface[126]. Therefore we believe that the reason for the different behavior of the surface Debye temperature is due to the different nature of the LEED experiments in comparison to HAS whereupon the helium atoms are scattered at the surface electron density.

5.4 Conclusion and Outlook

Elastic HAS experiments on Bi(111) at 123 K reveal clear diffraction peaks up to third order whose positions are in an excellent agreement with the structural data previously obtained by Mönig et al.[103]. High intensities in the diffraction peaks evidence a large corrugation both at surface temperatures of 123 K and 300 K compared to other surfaces with metallic behavior. With the eikonal approximation and the GR method a corrugation function could be determined with a corrugation height of approximately 10% of the surface lattice constant. This value is somewhat lower than the corrugation previously obtained by Tamtögl et al.[4], likely due to the inclusion of the Beeby correction and higher order diffraction peaks. The corrugation shows a quite remarkable enhancement of the electron density between the positions of the Bi atoms which could be a possible topic of future ab-initio calculations of the electron density of Bi(111).
Thermal attenuation effects in the intensities of the diffraction peaks were studied in a temperature range between 118 K and 408 K. A typical Debye-Waller behavior revealed surface Debye temperatures of (84 ± 8) K from the measurements of the specular peak and (75 ± 8) K from the measurements of the first order peak. In contrast to LEED measurements of a Bi nanofilm with a similar structure the surface Debye temperature measured with HAS remains constant over the whole temperature range, probably because of the different nature of electrons and helium atoms in scattering experiments. In our calculations the application of the Beeby correction with a potential well depth of 8 meV provided best results. With possible bound state resonance effects this value as well as the shape of the interaction potential between He and the Bi surface may be tested and further investigations are underway.

6 Helium Atom Scattering Investigation of the Sb(111) Surface

The following corresponds to a publication by
Michael Mayrhofer-Reinhartshuber, Anton Tamtögl, Patrick Kraus, and Wolfgang E. Ernst in *Journal of Physics: Condensed Matter*, **25**:395002-1-9, August 2013[60].

The author of this thesis was responsible for

- the LEED and AES measurements (see figure 6.2),
- the main parts of the angular HAS measurements of Sb(111) (see figures 6.4, 6.5, and 6.3),
- the analysis of the corrugation with the GR method (see section 6.3.2 and figures 6.4, 6.5, and 6.6),
- and the authorship of the abstract and sections 6.1, 6.2, 6.3.1, 6.3.2, and 6.4.

The contributions of the co-authors are listed below:

- A. Tamtögl: HAS-measurements, Step-size and distribution (section 6.3.3)
- P. Kraus: Check of the implemented algorithms
- W.E. Ernst: supervision (experiment, theory, publication), laboratory, funding

Abstract

The Sb(111) surface was studied with helium atom scattering (HAS). Elastic HAS at different energies of the incident helium beam (15.3, 21.9, 28.4 meV) was applied for structural investigations. Lattice constants derived from the positions of the observed diffraction peaks up to third order are found to be in perfect agreement with previous structure determinations of Sb(111). Observed diffraction patterns with clear peaks up to second order were used to model the electronic surface corrugation with the GR method. As an estimation for the attractive part of the interaction potential a well depth of (4.0 ± 0.5) meV was found. Best fit results were obtained with a corrugation height of 12-13% of the lattice constant, which is rather large compared to other surfaces with metallic character. Intensity measurements of the specular peak as a function of incident energy were analysed to determine the distribution of terraces on the surface. The results show a quite flat Sb(111) surface and a step height of 3.81 Å of the remaining terraces.

6.1 Introduction

As one of the essential components in the newly discovered group of topological insulators[9], the semimetal antimony (Sb) has recently attracted significant interest. The main feature of this group is the existence of metallic surface states, which appear due to the topology of the electronic bands despite the insulating behaviour of the bulk[9,84,85]. Similar topological surface states at the antimony surface were subject of several experimental investigations (angle resolved photoemission spectroscopy (ARPES)[79,97–99], scanning tunneling microscopy (STM)[127]) as well as theoretical studies[10,128]. Furthermore, it was shown that Sb nanofilms are interesting candidates for applications in spintronics due to the effects of reversible spin polarization and tuneable bandgaps[83,129]. Another application of Sb(111) was found in a recent STM study. It was shown that Sb(111) electrodes in aqueous electrolyte solutions do not undergo quick surface reconstruction processes and can be used for future studies of two-dimensional adsorption layer formation processes of different organic compounds in ionic liquids[130]. Beside studies which focus on the characterization of the geometrical and electronic structure, thermal desorption spectroscopy shows indications for a considerable hydrophobic character of the Sb(111) surface[100]. The surface dynamics, namely the surface phonon modes of Sb(111) as well as the influences of electron-phonon interaction were calculated using density functional perturbation theory[10]. However, no further investigations of the surface dynamics have been reported so far. Due to the lack of experimental data, probing of Sb(111) with other particles than electrons is long overdue.

As a strictly surface sensitive technique, helium atom scattering (HAS) allows to investigate surface structure and dynamics of various materials[39]. Although semimetals

have interesting features, such as being much better conductors at the surface than in the bulk, and play an important role in the case of topological insulators, only two of them have been studied with HAS so far: First, structural corrugations as well as gas-surface potentials of carbon allotropes (graphite and graphene) were investigated[131–133]. With HAS it was possible to determine the electronic corrugation of epitaxially grown graphene, which was found to be much smaller than the structural corrugation reported from x-ray diffraction or low-energy electron diffraction (LEED) measurements[132]. Second, our group used HAS to investigate Bi(111) quite recently[5]. It was shown that HAS is able to detect sub-surface phonons on semimetal surfaces in the case of a strong electron-phonon interaction[6–8]. Therewith it is possible to obtain information about the surface e-p interaction strength[6,134]. Thus, HAS measurements of Sb(111) represent a plausible step towards a complete understanding of the group of semimetals as well as topological insulators.

6.1.1 Structure and Properties of Sb(111)

The structure of bulk antimony under standard conditions was investigated for the first time by W. H. Bragg and W. L. Bragg with the technique of X-ray diffraction[87]. Lattice constants were determined with improved precision over the years[88–92]. Sb crystals are built in the rhombohedral A7 structure (space group $R\bar{3}m$) with two atoms per unit cell[92]. In the hexagonal notation, which is the most intuitive choice when focusing on the (111) surface, the lattice constants are a=(4.3084±0.0002) Å and c=(11.2740±0.0005) Å at standard ambient conditions[91,92]. Each atom has three nearest neighbours, the distance to the three next nearest neighbours is slightly higher. This results in one of the main features of this formation, which are puckered bilayers of atoms with an orientation perpendicular to the ⟨111⟩ direction. Within these bilayers the bonding is of a covalent type whereas the inter-bilayer bonding is of van der Waals character. Due to these weaker inter-bilayer bonds Sb easily cleaves along the ⟨111⟩ direction[93]. In figure 6.1 a model of the Sb structure is shown with respect to the investigated (111) surface. The rhombus with sidelength a represents the unit cell of the surface structure in the hexagonal notation. The sixfold symmetry described by the very first-layer atoms of Sb(111) is reduced to threefold symmetry by including second-layer atoms. Nevertheless, with the applied energies during the HAS experiments of this study, influences of other than first-layer atoms can be neglected. Hence, the ⟨10⟩ as well as the ⟨11⟩ direction, which are both shown in figure 6.1 can be treated as mirror planes. First investigations of the surface structure were performed with LEED[96] and reflection high-energy electron diffraction (RHEED)[135]. Recent experiments using STM[93] and photoelectron diffraction[95] revealed the detailed geometric structure of the surface, which does not undergo relevant relaxations with respect to the bulk.

In contrast to the semimetallic properties of its bulk, the Sb(111) surface is found to

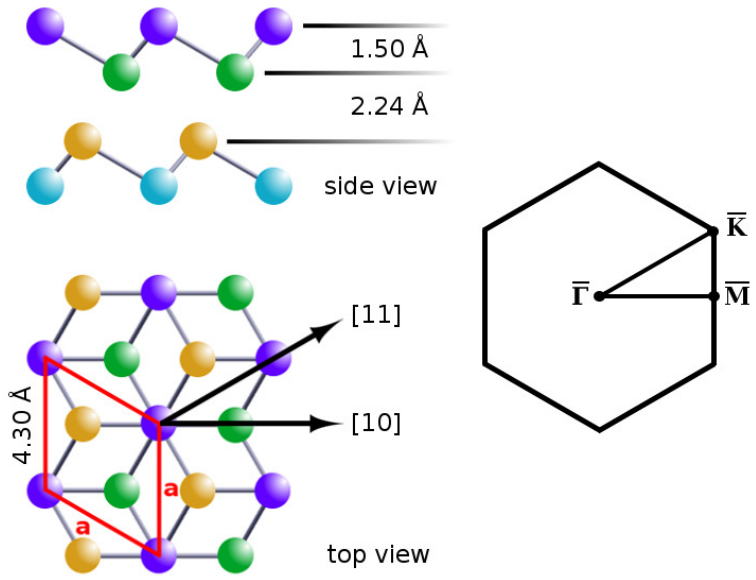

Figure 6.1: Sb(111) surface structure with the two high-symmetry directions of the topmost layer. Lattice constants as determined by Bengió et al.[95].

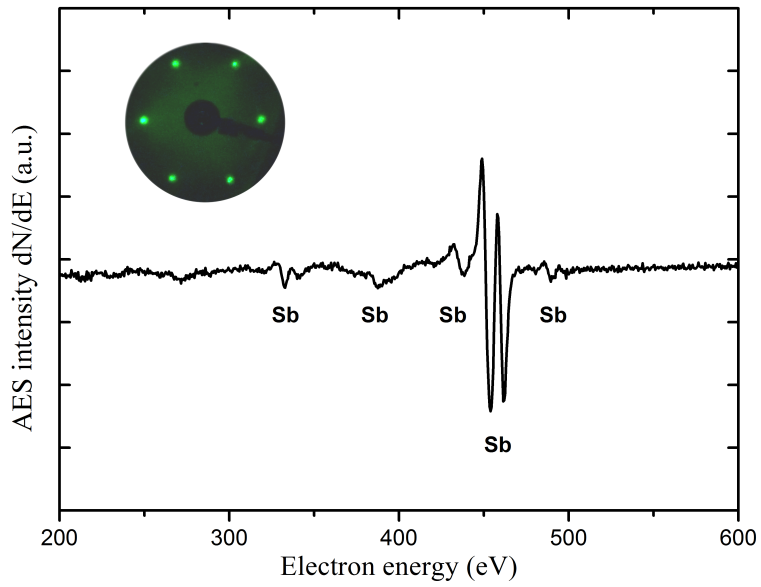

Figure 6.2: AES spectrum of Sb(111). The inset shows sharp LEED spots (beam energy: 38 eV) which are also indications for a clean, non-reconstructed surface. The cleanliness of the surface was checked before and after HAS measurements.

be metallic[97,98], which is similar to the low-index surfaces of Bi[80]. In the vicinity of the Fermi level the electronic band structure shows one hexagonal-like electron pocket at the center of the zone and six ellipsoidal shaped hole pockets encircling this pocket[97,99].

6.2 Experimental Details

All experiments of this study were performed on the HAS-apparatus H.Å.N.S. (Helium Atom Nondestructive Scattering), whose properties were described in greater detail elsewhere[4]. Briefly, a supersonic expansion ($p_{He,1} = 50$ bar $\rightarrow p_{He,2} \approx 10^{-6}$ mbar) through a nozzle (10 μm) and the subsequent selection of the central part of the beam with a skimmer (310 μm orifice) were used to create an almost monoenergetic He beam with an energy spread of $\Delta E/E \approx 2\%$. By varying the nozzle temperature, beam energies between 15 meV and 30 meV can be achieved. After the interaction with the sample crystal placed in an ultra-high vacuum (UHV) chamber, the He atoms of the beam are detected using a quadrupole mass analyser (QMA), which is positioned at the end of a differentially pumped UHV system in a cross-beam geometry. The apparatus has a fixed 91.5° source-target-detector geometry, thus the rotation of the sample has to be changed in order to achieve measurements at different incident angles.

The sample crystal was placed on a six-axis manipulator in the main chamber. Within this chamber, the base pressure was kept below $2 \cdot 10^{-10}$ mbar. The commercially available Sb(111) crystals were purchased from Metal Crystals & Oxides Ltd[102]. They had the shape of a disc with a diameter of (15 ± 1) mm and a thickness of (1.5 ± 0.5) mm.

Sample preparation was performed with a procedure based on a description of Shan et al.[100]. First the surface was sputtered with Ar^+ ions (1.7 kV, 3 μA/cm^2, 15 min) at room temperature. Afterwards the sample was heated to 550 K for approximately one hour. To achieve a completely clean crystal surface, several cycles of this treatment were performed. To prove the surface quality, we used low energy electron diffraction (LEED) and Auger electron spectroscopy (AES). Sharp LEED spots as well as clear Sb features in the AES spectrum (both shown in figure 6.2) indicated a surface free of any contaminations. The temperature of the sample was measured using a type-K (chromel-alumel) thermocouple.

All measurements during this study were carried out at an in-plane scattering geometry. For that purpose the scanning direction was calibrated by adjusting the azimuthal orientation of the crystal while observing the LEED picture. Subsequently, the vertical tilt of the sample was tuned to an optimum position. For the measurement itself the polar (incident) angle θ_i was changed by rotating the sample around the corresponding axis.

6.3 Data and Results

6.3.1 Elastic Scattering

Angular HAS scans were performed along both low-index high symmetry directions ($\overline{\Gamma M}$, $\overline{\Gamma K}$) of the surface and with different energies (15.3 meV, 21.9 meV and 28.4 meV) of the incident helium beam. For HAS at these energies, the turning point of the He atoms is in a region where only the very first layer contributes significantly to the relevant part of the electron corrugation above the surface. Therefore, the symmetry of the surface can be considered as sixfold.

By using incident energies of the helium beam up to 28.4 meV diffraction patterns with peaks up to third order were observable. Angular scans at this energy along the $\overline{\Gamma M}$ and $\overline{\Gamma K}$ direction are shown in figure 6.3 (a) and (b). The measured intensity is plotted as a function of the incident angle with the zero-order diffraction peak at $\theta_i = 45.75°$. Because of the large width of the peaks due to the energy broadening of the helium beam at this energy, lower incident energies ($E_{i,1}$ = 15.3 meV and $E_{i,2}$ = 21.9 meV) were used for further investigations during this study. At these energies a further test for quality and cleanliness of the surface was performed by taking a closer look at the shape of the peaks. As an example, the specular peak at $E_{i,1}$ is shown in figure 6.3 (c) with the sample rotated in the $\overline{\Gamma K}$ direction. Since the elastic peaks are composed of a narrow coherent peak and broad diffuse elastic and multiphonon contribution[47], the fitting function consists of two Gaussian contributions. Figure 6.3 (c) shows the narrow width of the coherent elastic contribution (red, dashed line) as well as a small magnitude of the diffuse part (green, dash-dotted line), which represents a good indication for a clean sample surface. Their sum (blue, solid line) is in very good agreement with the measured intensity values (blue dots) .

The experimental results of the scans with the chosen beam energies $E_{i,1}$ and $E_{i,2}$ are depicted in figures 6.4 and 6.5 (solid lines). A slight asymmetry in the angular scans occurred due to a not totally perfect alignment as well as the probable existence of steps on the Sb(111) surface[93,115]. An optimization procedure for the sample position at each peak position yielded an estimate of 10% uncertainty for the experimentally determined intensities caused by the influence of the small misalignment. Diffraction peak positions are in perfect agreement with the expected values, confirming the already known, non-reconstructed surface structure[93,95]. The shown measurements illustrate that a large fraction of the scattered He atoms can be found in first or higher order diffraction peaks. Thus, a contingently occurring Smoluchowski effect due to the metallic character of the surface seems negligible since this would result in lower intensities of these features[37]. As it has been found also for HAS on Bi(111)[4,5], the electronic surface corrugation for HAS on Sb(111) has an increased importance compared to other metallic surfaces[136,137], even when compared to the highly corrugated Ag(110) surface, where HAS experiments

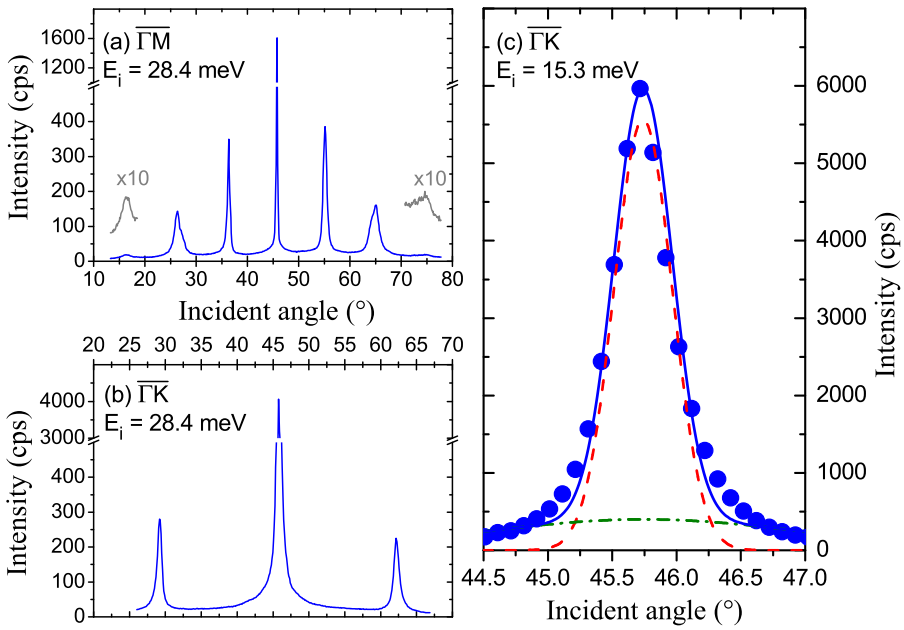

Figure 6.3: Scattered intensity of He versus incident angle for He diffracted from Sb(111) at a temperature of 300 K. Angular scans along $\overline{\Gamma M}$ (a) and $\overline{\Gamma K}$ (b) show diffraction peaks up to third order. In (c) the narrow coherent elastic peak (red, dashed line) over a small diffuse contribution (green, dash-dotted line) confirms the cleanliness of the sample. The sum of these parts (blue, solid line) matches very well with the measured intensity values (blue dots).

with incident energies up to 62 meV revealed an electronic corrugation of 0.27 Å[138]. To investigate this effect more thoroughly, the diffraction peak intensities were analysed in detail.

6.3.2 The Surface Corrugation

The He-Sb(111) surface interaction potential was determined by performing diffraction intensity calculations based on the hard corrugated wall model. Experimentally obtained peak intensities had to be compared with theoretically calculated values. As a well established approach, the GR method[43,45] was used for this theoretical path. Furthermore, it has been shown recently that this procedure works well for similar semimetallic systems such as Bi(111)[5].

First, an appropriate model, i.e. a surface corrugation function $\xi(x, y)$ that describes the investigated surface, is required. Considering the sixfold-symmetry of the topmost layer of the surface as well as the applied incident energies of the helium beam, a two-parameter Fourier ansatz was used:

$$\begin{aligned}\xi(x,y) = \quad & \xi_{01} \cdot \left(\cos\left[\tfrac{2\pi}{a}\left(x - \tfrac{y}{\sqrt{3}}\right)\right] + \cos\left[\tfrac{2\pi}{a}\left(x + \tfrac{y}{\sqrt{3}}\right)\right]\right) \\ & + \xi_{01} \cdot \cos\left[\tfrac{2\pi}{a} \cdot \tfrac{2y}{\sqrt{3}}\right] + \xi_{11} \cdot h.o. \end{aligned} \tag{6.1}$$

where x and y denote the rectangular coordinates and $h.o.$ symbolizes Fourier terms up to second order. For various coefficients ξ_{01} and ξ_{11} hard wall intensities P_G^{calc} were calculated for a sufficient amount of diffraction peaks G and compared to the experimental diffraction possibilities P_G^{exp} . Conrad et al. have shown that this approach is sufficiently accurate for fitting hard wall corrugation functions[39,55].

Since the obtained values P_G^{calc} correspond to a surface temperature of $T_{\mathrm{S}} = 0$ K, dynamic effects have to be taken into account. For comparison with the experimental results, the diffraction intensities at finite surface temperatures $I_G^{\mathrm{calc}}(T_{\mathrm{S}})$ were calculated using

$$I_G^{\mathrm{calc}}(T_{\mathrm{S}}) = e^{-2W} P_G^{\mathrm{calc}}, \tag{6.2}$$

where $2W$ denotes the correspondig Debye-Waller factor,

$$2W = \frac{3\hbar^2 T_{\mathrm{S}} (k_{\mathrm{iz}} + k_{\mathrm{fz}})^2}{M k_{\mathrm{B}} \Theta_{\mathrm{D}}^2}, \tag{6.3}$$

with M the mass of the surface atom, Θ_{D} the surface Debye temperature, $\hbar$ the reduced Planck constant, and k_{B} the Boltzmann constant. k_{iz} and k_{fz} denote the components of the incident and final (outgoing) wavevectors perpendicular to the surface. A surface Debye temperature of $\Theta_{\mathrm{D}} = 155$ K was used. This value was obtained in a recent study of our group, in which vibrational dynamics of Sb(111) were probed with HAS experiments[76]. In this study, the thermal attenuation of the diffraction intensities of the

specular and first order diffraction peaks with varying surface temperature was analyzed. Measurements at four different energies of the incident He atoms were performed to find a surface Debye temperature of (155 ± 3) K. As an estimation for the mean-square displacement perpendicular to the surface, a value of $(1.8 \pm 0.4) \times 10^{-2}$ Å^2 was found at room temperature. Additionally, a well depth of (4.5 ± 0.5) meV for the attractive part of the He-surface interaction potential was obtained. In contrast to LEED experiments, where the motion of the ion cores is measured directly, in the determination of the Debye temperature with HAS experiments the fluctuation of the outermost charge density is probed. Hence, the Debye temperature obtained with HAS may differ from values determined with other techniques. Nevertheless, since the same experimental method as in the present study was applied, this result was used in equation (6.3). Furthermore, it is in excellent agreement with an approximation of van Delft[122], that estimates a surface Debye temperature from a given bulk Debye temperature ($\Theta_{\mathrm{D,bulk}} = 211$ K[18]).

The comparison of the theoretically evaluated and corrected intensities $I_G^{\mathrm{calc}}(T_{\mathrm{S}})$ with the experiment was performed by determining the experimental peak areas P_G^{exp}. The reason for using the peak areas instead of the peak heights is due to the broadening of the elastic peaks caused by the energy spread of the He beam. Furthermore, additional broadening of the diffraction peaks is caused by the geometry of the apparatus, defects and the domain size effects of the crystal surface[116,117]. Nevertheless, the elastic peaks are still narrow, lying above a broad diffuse elastic and inelastic contribution (see figure 6.3 (c))[47]. Thus, a sum of two Gaussian functions was used to fit the experimental peaks. Afterwards, areas of the narrow coherent elastic peaks were taken, while each pair of peaks (G, $-G$) was averaged. These values were used as P_G^{exp} and compared with the appropriate calculations.

To determine the best-fit coefficients, the amplitudes ξ_{01} and ξ_{11} were optimized by finding the best agreement between measured and calculated intensities. Intensity values of all diffraction peaks were normalized by dividing by the intensity of the corresponding specular peak. To check the accuracy of these fits, a reliability factor R,

$$R = \frac{1}{N}\sqrt{\sum_G (P_G^{\mathrm{exp}} - I_G^{\mathrm{calc}}(T_{\mathrm{S}}))^2}, \tag{6.4}$$

with N the number of experimentally observed diffraction peaks has been calculated[39].

The described fitting procedure was applied to angular HAS scans with the Sb crystal at room temperature ($T_{\mathrm{S}} = 300$ K). To account for dynamic effects arising from a finite surface temperature the experimentally found values were corrected using the Debye-Waller factor (6.2). The shape of the modelled corrugation is a function of the incident energy since it is based on the classical turning point of the incident He atoms[139,140]. Therefore, two separate optimizations were performed and different parameters of the corrugation function $\xi(E)$ were obtained for both incident energies $E_{\mathrm{i},1}$ and $E_{\mathrm{i},2}$. Uncertainties were estimated by repeating the described calculations with an inclusion of the

uncertainty of 10% for diffraction peak intensities, which is the dominant component of error sources. Since the He-surface interaction potential exhibits also an attractive part, the Beeby correction was used in the models to account for this attractive well[39,46]. This approximation uses the well depth D, which is added to the energy of the incident helium atoms. Hence, the incident wavevector k_i as well as Θ_i have to be replaced in the calculations with an effective k'_i given by

$$k'_\mathrm{i} = \sqrt{\frac{2m(E+D)}{\hbar^2}} = k_\mathrm{i}\sqrt{1+\frac{D}{E}} \tag{6.5}$$

and a smaller effective angle of incidence Θ'_i with

$$sin(\Theta'_\mathrm{i}) = \frac{sin(\Theta_\mathrm{i})}{\sqrt{1+\frac{D}{E}}}. \tag{6.6}$$

Using these effective values a well depth of (4.0±0.5) meV was found to result in the best fits. Compared to He-Bi(111) with a well depth of (8.3±0.8) meV of the averaged surface potential[8], the determined value for Sb(111) is much lower. This can be explained by weaker van der Waals interaction between the He atoms and the Sb(111) surface due to the smaller polarizability of Sb compared to Bi.

The peak-to-peak corrugation

$$\xi_\mathrm{pp}(E) = max(\xi(E)) - min(\xi(E)) \tag{6.7}$$

for an incident energy $E_{\mathrm{i},1}$ was found to be $\xi_\mathrm{pp}(E_{\mathrm{i},1}) = (0.52 \pm 0.02)$ Å, which is $12.1\% \pm 0.4\%$ of the lattice constant a. The degree of agreement between experiment and calculation is given by a reliability factor $R(E_{\mathrm{i},1}) = 0.5\%$ according to (6.4). For an incident energy of 21.9 meV the calculations yielded a peak-to-peak corrugation of $\xi_\mathrm{pp}(E_{\mathrm{i},2}) = (0.57 \pm 0.03)$ Å $(13.3\% \pm 0.5\%)$ with a reliability factor $R(E_{\mathrm{i},2}) = 0.9\%$. The stars in figure 6.4 and 6.5 designate the peak areas (P_G^{exp}) while the results of the GR method are shown as squares (identical within the resolution of the figure). Both the reliability factors and the comparison of experimental and theoretical results depicted in figure 6.4 and 6.5 demonstrate the very good agreement of measured and calculated diffraction intensities and hence the quality of the modelled corrugation.

In figure 6.6(a) the best fit corrugation function for $E_{\mathrm{i},2}$ is shown. For a better illustration, cuts of the corrugation along both high symmetry directions are shown in figure 6.6(b) and 6.6(c). Besides the expected structure originating in the positions of the Sb atoms of the topmost layer an enhancement of the electron density between these positions (along the $\overline{\Gamma\mathrm{K}}$ direction) seems to appear. The lateral position of this characteristic does not match with the position of underlying atoms in the bilayer. At $E_{\mathrm{i},2}$ (solid black line) this feature is more distinct than at lower incident energy $E_{\mathrm{i},1}$ (dashed

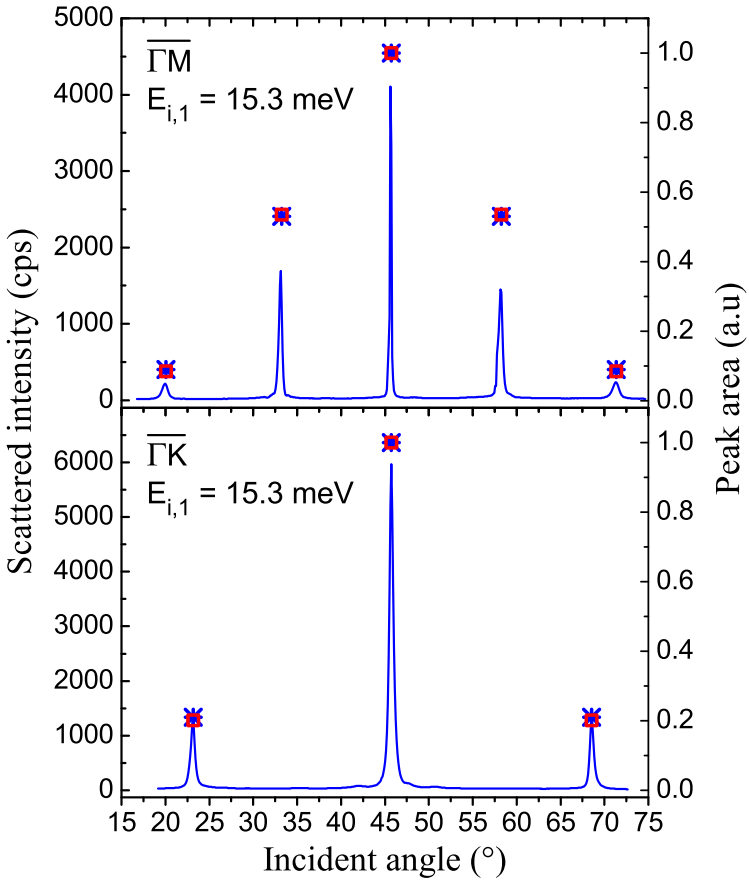

Figure 6.4: Scattered intensity of He versus incident angle for He diffracted from Sb(111) at a temperature of 300 K. In the upper part an angular scan along the $\overline{\Gamma M}$ azimuth at an incident energy of $E_{i,1} = 15.3$ meV is shown. The lower part depicts an angular scan along the $\overline{\Gamma K}$ azimuth at the same beam energy. The stars indicate the experimentally determined peak areas and the red squares correspond to the results of the GR method.

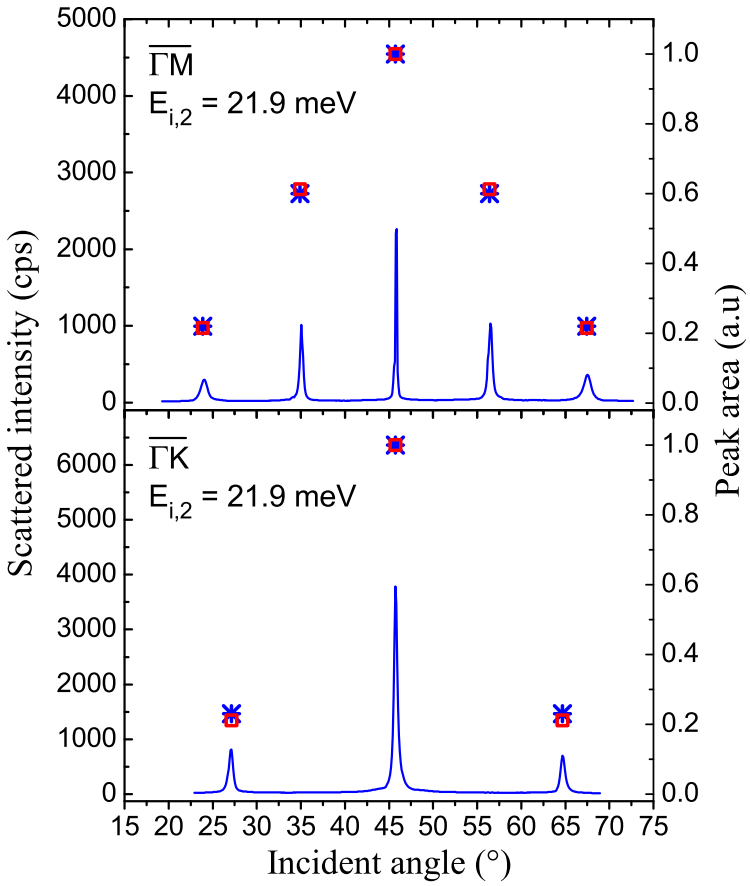

Figure 6.5: Scattered intensity of He versus incident angle for He diffracted from Sb(111) at a temperature of 300 K. In the upper part an angular scan along the $\overline{\Gamma M}$ azimuth at an incident energy of $E_{i,2} = 21.9$ meV is shown. The lower part depicts an angular scan along the $\overline{\Gamma K}$ azimuth at the same beam energy. The stars indicate the experimentally determined peak areas and the red squares correspond to the results of the GR method.

blue line). More precise yet much more time-consuming *ab initio* calculations would be interesting to investigate this behaviour in detail.

Compared to a surface corrugation of 10%, which was obtained for the semimetal Bi(111)[5], the values found for Sb(111) are a little higher for comparable incident energies. In general the electron density corrugation tends to be more smeared out when moving further away from the surface. Hence the higher corrugation on Sb(111) compared to Bi(111) might be a hint towards a He turning point lying closer to the surface in the case of He-Sb(111).

There exist only a limited number of direct comparisons between different atom-surface systems and actually none for different semimetallic materials. Thus, the results were compared with those obtained for group 11 metals which have been relatively well studied with HAS. Using the cut-off parameter Q_c and the softness parameter β determined in these studies, the average He turning point $\bar{z}$ on the corresponding surface can be calculated according to $\bar{z} = \beta/Q_c^2$[141,142]. This shows that the average He turning point migrates further away from the surface with increasing atomic number within the group 11 metals. This fact is also supported by recent calculations which show that the distance of the jellium edge from the surface layer increases when the He-Cu(001) system is compared to He-Ag(001)[143].

In view of these facts, the larger corrugation on Sb(111) compared to Bi(111) seems to confirm this trend for these two elements within the group 15. Yet in order to show that the increasing corrugation is really connected with a decreasing He turning point and to prove that it can be seen as a general trend for the group 15 semimetals further *ab initio* calculations are needed. Such calculations appear particularly desirable, because the electron density on semimetal surfaces differs significantly with respect to those on metal surfaces. Furthermore, measurements with a much higher resolution as they can be provided by the novel helium-3 spin-echo scattering technique would be advantageous[2].

6.3.3 Surface Steps and Terrace Height

For scattering from a “real" surface the specular intensity is usually dominated by interference effects due to waves scattered from different terraces[39]. This fact becomes evident when the intensity of the specular peak is monitored while changing the perpendicular component of the incident He wavevector k_{iz}. Therefore the energy of the incident helium beam is varied ($k_i = \sqrt{2mE_i}/\hbar$). Again, the observed peak consists of two different contributions. In contrast to the intensity of the narrow coherent peak, the intensity of the broad diffuse elastic and multiphonon contribution showed only a negligible change. Hence, monitoring the specular peak as the sum of both contributions is an adequate approach. Such a plot of the specular peak intensity is shown in figure 6.7(a).

The intensity of the specular peak oscillates due to constructive (in-phase) and destruc-

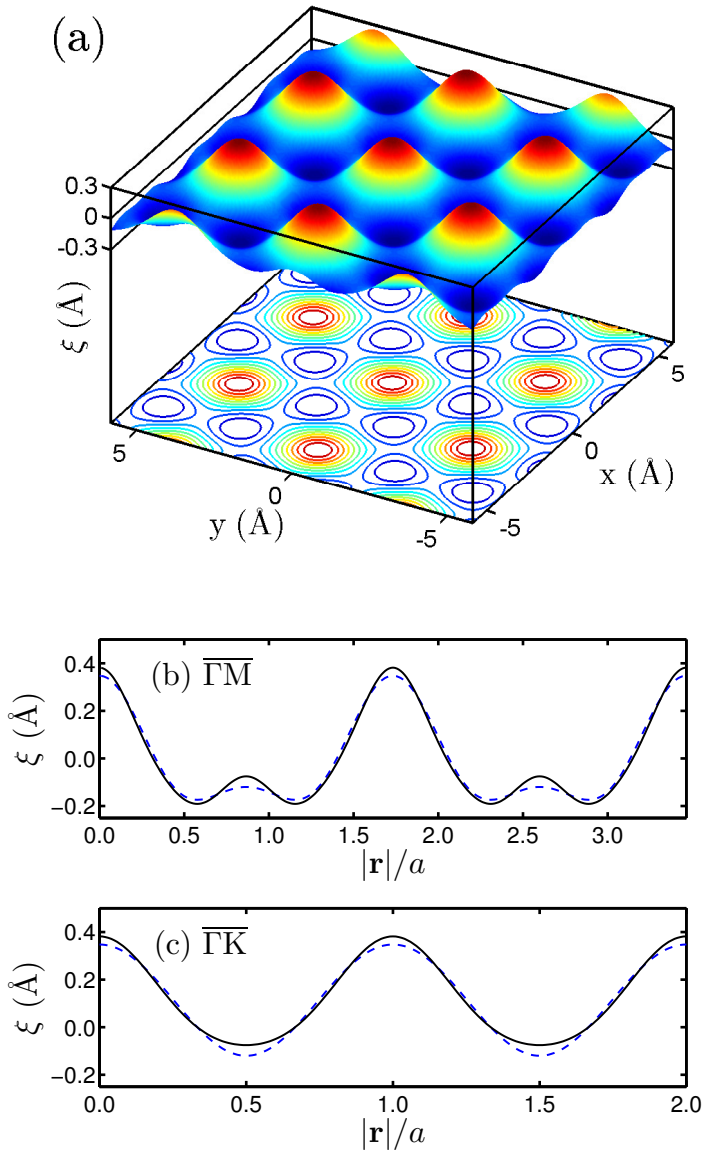

Figure 6.6: (a) Plot of the hard wall potential surface for the Sb(111) surface at an incident energy of $E_{i,2}$=21.9 meV. The GR method was used to fit the model potential (6.1) to the measured helium diffraction intensities as shown in figure 6.5. The obtained corrugation exhibits a peak-to-peak amplitude of (0.57 ± 0.03) Å. (b) and (c) show cuts along the $\overline{\Gamma M}$ and $\overline{\Gamma K}$ direction, respectively. On each x-axis the distance $|\mathbf{r}|$ to an arbitrary Sb atom of the topmost layer is given relative to the lattice constant a. The solid black lines represent cuts of the corrugation obtained at $E_{i,2}$=21.9 meV (depicted in (a)) and are compared to cuts of the corrugation obtained for an incident energy of $E_{i,1}$=15.3 meV (dashed blue lines).

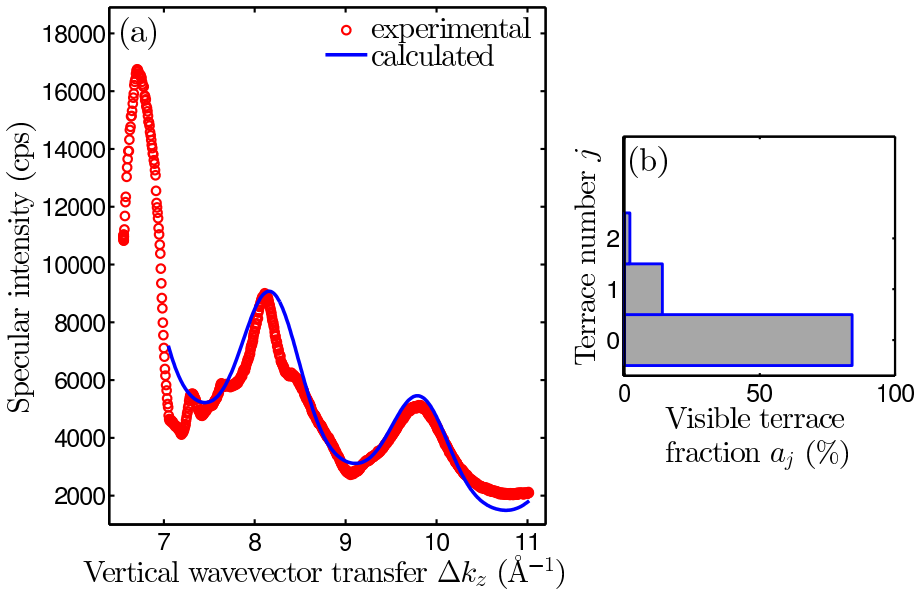

Figure 6.7: (a) Specular intensity as a function of the vertical wavevector transfer Δk_z of the He beam. The measurement was performed along the $\overline{\Gamma M}$ azimuth while the crystal was kept at room temperature. The experimental data points (open circles) were fitted using equation (6.8) for values between 7 and 10 Å^{-1} (solid line).
(b) The distribution of the terraces as obtained from the best-fit result.

tive (antiphase) interference between waves emerging from different terrace levels. For the specular geometry the phase difference between two waves scattered from two adjacent terrace levels is given by[57,59]:

$$\varphi = 2hk_i \cos\theta_i = h\Delta k_z \tag{6.8}$$

where h is the step height and Δk_z is the wavevector transfer perpendicular to the surface. For $\varphi = 2\pi n$ an integer value of n gives rise to in-phase scattering whereas a half-integer value of n causes antiphase scattering. When the incident energy of the He beam meets one of these conditions maxima or minima are observed. This periodic change in the intensity is superimposed by the attenuation of the specular intensity due to the Debye-Waller effect (see (6.2)) with increasing $k_{iz} = k_i \cos\theta_i$[57].
The experimental data points (open circles) in figure 6.7(a) show the measured intensity of the specular peak on Sb(111) versus the perpendicular wavevector transfer Δk_z. Since for the specular scattering geometry $\Delta k_z = 2k_{iz}$ holds, Δk_z is varied by changing the energy of the incident He beam via the nozzle temperature. As the intensity of the incident He beam depends on the nozzle temperature T_N via $1/\sqrt{T_N}$[144], the measured intensity has been corrected for this factor.

In a first attempt, the intensity variation can be described by a simple model which

assumes the coherent overlap of plane waves that are emerging from different terrace levels. The scattered specular intensity as a function of Δk_z is then given by[57,59]:

$$I(\Delta k_z) = I_0 e^{-2W} \left| \sum_{j=0}^{\infty} a_j e^{-ij\varphi(\Delta k_z)} \right|^2 \tag{6.9}$$

where I_0 is the intensity of the specular peak for an ideal surface without steps. $\varphi(\Delta k_z)$ is the phase shift as defined in (6.8) and a_j the visible fraction of terrace level j. The exponential prefactor accounts for the aforementioned attenuation of the intensity due to the Debye-Waller effect (see equation (6.2)).
However, this simple model neglects the occurrence of selective adsorption resonances whereupon the He atom is bound temporarily on the surface due to the attractive well of the He-surface interaction potential. Such selective adsorption processes give rise to peaks and dips in the scattered intensity with changing incident beam energy[39]. As can be seen in figure 6.7(a) various fine peaks and dips are superimposed onto the main peaks which suggest the occurrence of selective adsorption resonances. It has also been noted by Pan et al.[59] that the distance between the maxima may not be exactly equidistant due to overlaying resonance effects. While an understanding of these resonance processes is crucial e.g. in the analysis of inelastic scattering events[8], it is a rather complex task and we will restrict ourselves to an analysis of the contribution from surface steps.
Therefore, we have analysed the experimental data points in 6.7(a) in more detail only at higher beam energies since resonance processes become less pronounced with increasing k_{iz}[39]. The solid line in figure 6.7(a) represents the best fit to the experimental data points using equation (6.9) under the assumption that three surface layers are visible to the He beam.
The surface step height determined from the fit is $h = 3.81$ Å which agrees well with the step height of a bilayer (see figure 6.1). This value is somewhat larger than the value determined from STM measurements ($d = (3.75 \pm 0.10)$ Å[93]) but in perfect agreement with recent calculations[10]. The distribution of the terraces obtained by the fitting of equation (6.9) is depicted in figure 6.7(b). The best-fit coefficients a_j are $a_0 \approx 84\%$, $a_1 \approx 14\%$ and $a_2 \approx 2\%$. While these results should be considered with care due to the simplicity of the model, they indicate that the clean Sb(111) surface is quite flat. An evidence for this fact is also the good quality of the diffraction patterns as seen in section 3.1.

6.4 Conclusion and Outlook

Elastic HAS experiments on Sb(111) at a temperature of 300 K reveal diffraction peaks up to third order. The positions of these peaks are in perfect agreement with the already

known structural data[93,95]. Rather high diffraction peaks indicate a large electronic corrugation as it has been shown for the (111)-surface of the semimetal Bi[5]. Experimentally obtained diffraction intensities were compared to theoretical values, which were determined by using a hard corrugated wall model for the He-Sb(111) surface interaction potential. A potential well depth of (4.0 ± 0.5) meV provided best fit results when applying the Beeby correction in our calculations. The GR method was used to determine corrugation functions with a corrugation height in the region of 12-13% of the surface lattice constant at incident beam energies of 15.3 meV and 21.9 meV. Compared to Bi(111) this value is slightly higher which may be an effect of a He turning point lying closer to the surface in the case of He-Sb(111). Furthermore, the obtained corrugations show enhanced values between the positions of the Sb atoms, which rise with increasing incident energy. This remarkable enhancement of the electron density has been observed also at the Bi(111) surface and its origin could be a topic of future *ab initio* calculations. Furthermore, possible influences of anticorrugating effects, as they were observed in scattering processes from metal surfaces[145,146], could be included in prospective studies. A plane wave model was applied to intensity measurements of the specular peak which revealed the quite flat shape of the clean Sb(111) surface. The surface step height was found to be 3.81 Å which is in excellent agreement with recent calculations[10]. A thorough investigation of inelastic effects as well as surface phonon measurements are a logical step towards a more complete understanding of the Sb(111) surface as well as other materials with metallic surface states.

7 Surface Debye Temperature and Vibrational Dynamics of Antimony(111) from Helium Atom Scattering Measurements

The following corresponds to a publication by
Anton Tamtögl, **Michael Mayrhofer-Reinhartshuber**, Patrick Kraus and Wolfgang E. Ernst in *Surface Science*, **617**:225-228, August 2013[76].

The author of this thesis was responsible for

- the LEED and AES measurements,
- the main parts of the temperature-dependent HAS measurements of Sb(111),
- assisting the first author with the analysis of the measurements and the determination of the Debye temperature,
- and the authorship of sections 7.1.1 and 7.2.

The contributions of the other authors are listed below:

- A. Tamtögl: HAS-measurements, main authorship
- P. Kraus: Check of the implemented algorithms
- W.E. Ernst: supervision (experiment, theory, publication), laboratory, funding

Abstract

The surface Debye temperature and the vibrational dynamics of Sb(111) were studied using helium atom scattering. The Debye-Waller attenuation of the elastic diffraction peaks was measured at surface temperatures between 98 K and 447 K. A surface Debye temperature of (155 ± 3) K is obtained within the description originally derived for electron diffraction. The attractive well depth for the He-Sb(111) interaction is determined to be (4.5 ± 0.5) meV. The perpendicular mean-square displacement for the surface at room temperature is estimated to be $(1.8 \pm 0.4) \times 10^{-2}$ Å^2.

7.1 Introduction

Antimony has recently attracted considerable interest since it is present in several compounds belonging to the newly discovered class of topological insulators. These compounds display an insulating behavior in the bulk, but exhibit metallic surface states due to the topology of the bulk electronic bands[9,83–85]. Moreover, Sb nanofilms offer attractive features for potential applications in spintronics such as a tunable band gap and spin polarization[83].

The electronic surface states of antimony have been studied both experimentally and theoretically[10,79,97–99,127,128]. While the surface phonons of Sb and the aspect of coupling between surface topologically protected states and phonons have been studied theoretically[10], no measurements regarding the surface dynamics of Sb(111) have been reported so far. In this context an investigation of the thermal vibrations at the surface of Sb(111) is particularly interesting.

Helium atom scattering (HAS) is a strictly surface sensitive technique which can be utilized to study the surface structure and dynamics of a wide range of materials[39]. Despite their great importance, especially in the case of topological insulators, semimetals have never been approached with HAS due to their intrinsic complexity of being surface conductors (even superconductors) and strongly corrugated at the same time. The only exceptions are graphite[147,148] and Bi(111) which was investigated recently using HAS[5]. A study of the surface phonon dispersion of Bi(111) showed that HAS is capable of detecting sub-surface phonons on semimetal surfaces[6–8]. The success of HAS was attributed to the comparatively strong electron-phonon interaction on Bi(111) whereupon inelastic HAS measurements can even provide information about the surface electron-phonon interaction strength[6,134].

7.1.1 Structure and Properties of Sb(111)

Jona et al.[96] reported the first low energy electron diffraction (LEED) patterns of Sb(111). The detailed surface geometric structure was recently determined by photoelectron diffraction[95] and scanning tunneling microscopy[93] whereupon no substantial relaxations with respect to the bulk spacing were found. A model of the geometric structure is shown in figure 7.1 a): The top view of the surface exhibits hexagonal planes and the side view shows the bilayer stacking which is characteristic of the group V semimetal structures[10,94]. The unit cell according to the hexagonal notation is highlighted by the rhombus with $a = 4.30$ Å[95] in the top view.
Although Sb is a bulk semimetal, it shares the same topological order of the 3D topological insulator $Bi_{1-x}Sb_x$.[85,86]. Similar to the low-index surfaces of Bi, the Sb(111) surface is found to be metallic in contrast to the semimetallic character of the bulk[80,97,98]. The electronic band structure in the vicinity of the Fermi level exhibits one hexagonal-like electron pocket at the zone center and six ellipsoidal hole pockets surrounding the electron pocket[97,99]. The surface states near the Fermi energy are spin-split due to the spin-orbit coupling and the broken space inversion symmetry[79].
Furthermore, the electronic properties of Sb(111) nanofilms are strongly dependent on the film thickness: By reducing the film thickness they undergo transitions from a semimetal to a topological insulator and to a quantum spin Hall phase[84,129]. In addition, in a single bilayer of Sb(111) nontrivial quantum spin hall states can be realized under tensile strain, whereupon the size of the band gap and the spin polarization can be tuned using an external electric field[83].

7.2 Experimental Details

All measurements of this work were conducted on a HAS apparatus with a fixed 91.5° source-target-detector geometry. A nearly monochromatic He beam was generated in a supersonic expansion of helium through a 10 µm nozzle and the central part of the beam was then selected using a 310 µm skimmer. The whole apparatus has been described in greater detail elsewhere[4].
The Sb(111) single crystal used in the study was a disc with a diameter of 15 mm and a thickness of 2 mm. The crystal was mounted on the sample holder which can be heated resistively using a button heater or cooled down to 100 K using liquid nitrogen. The sample temperature was measured using a chromel-alumel thermocouple. Prior to the measurements the surface was cleaned by Ar^+ sputtering and annealing to 490 K. Cleanliness and surface order were ensured by Auger electron spectroscopy and low energy electron diffraction, respectively[60].
The thermal attenuation of the elastic scattering signal was recorded over a surface temperature (T_S) range of $98 - 447$ K. Specular and first-order diffraction peaks were

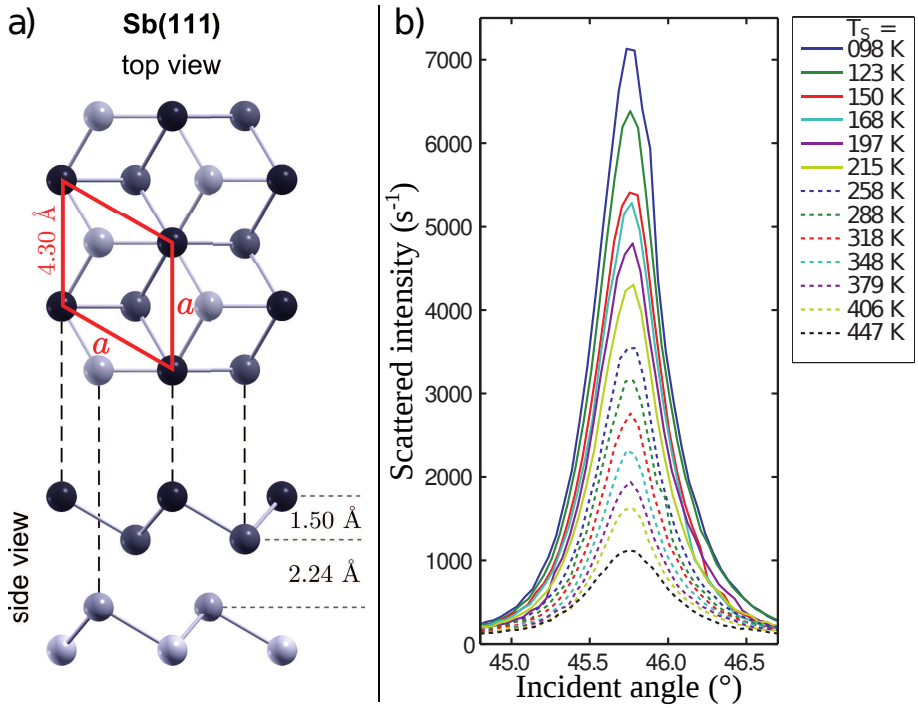

Figure 7.1: a) Top and side view of the Sb(111) surface structure (according to[95])
b) Plot of the attenuation of the specular peak with increasing surface temperature T_S of the Sb(111) sample. The scattered intensity of the helium beam with an incident energy of $E_i = 24$ meV is shown.

collected for four different incident beam energies E_i along the $\overline{\Gamma K}$ azimuth. The data was analyzed in order to determine the surface Debye temperature θ_D of Sb(111) and the attractive well depth of the He-Sb(111) system. Furthermore, an estimation of the vibration amplitude perpendicular to the surface is extracted from the measurements.

7.3 Results and Discussion

The thermal attenuation of the diffraction peaks provides insight into the surface vibrational dynamics: In the case of real systems zero-point motion and thermal vibrations of the surface atoms cause inelastic scattering of the incoming particles which can be observed in the thermal attenuation of the coherent diffraction intensities without a change in the peak shapes[39].
Figure 7.1 shows the decay of the zero order peak for He scattered from Sb(111) at an incident beam energy of $E_i = 24$ meV. Scans of the scattered intensity versus the incident angle θ_i were collected while the Sb surface temperature was varied between 98 K and 447 K. The decay of the peak intensity with increasing surface temperature T_S is caused by the increasing vibrational amplitude of the surface oscillators which can be described by the Debye-Waller factor[47]. The Debye-Waller factor $\exp[-2W(T_S)]$ relates the diffraction intensity $I(T_S)$ of a sample at temperature T_S to the intensity I_0 of a sample at rest by[39]:

$$I(T_S) = I_0 \cdot e^{-2W(T_S)} \tag{7.1}$$

The Debye-Waller factor is described using:

$$2W(T_S) = \left\langle (\vec{u} \cdot \Delta\vec{k})^2 \right\rangle_{T_S} \tag{7.2}$$

with $\vec{u}$, the displacement of a lattice atom out of its equilibrium position and $\Delta\vec{k}$ the momentum transfer during the scattering process. The outer brackets indicate that the thermal average has to be taken[39].
Equation 7.2 can be decomposed into contributions from the perpendicular momentum transfer Δk_z and the parallel momentum transfer ΔK[149,150]:

$$2W = \Delta k_z^2 \langle u_z^2 \rangle + \Delta K^2 \langle U^2 \rangle \tag{7.3}$$

For elastic scattering $\Delta K = k_i(\sin(\theta_i) - \sin(\theta_f))$ holds with the incident wave vector k_i and θ_i and θ_f the incident and final angle, respectively. Assuming that the momentum transfer parallel to the surface equals zero (i.e. for the specular geometry $\theta_i = \theta_f$) equation 7.3 reduces to:

$$2W(T_S) = \langle u_z^2 \rangle \cdot (\Delta k_z)^2 \tag{7.4}$$

where $\langle u_z^2 \rangle$ describes the average displacement of a crystal atom perpendicular to the surface. For a classical harmonic oscillator $1/2\ M\omega^2 \langle u^2 \rangle = 3/2\ k_B T$ holds. Applying the

Debye model and the definition of the Debye temperature[18] in terms of ω_D: $\hbar\omega_D/k_BT = \theta_D/T$, equation 7.4 becomes:

$$2W(T_S) = \frac{3\hbar^2\Delta k_z^2 T_S}{Mk_B\theta_D^2} \tag{7.5}$$

where M is the mass of the surface atom and θ_D the surface Debye-temperature.
It should be noted that equation 7.5 is not generally valid and it turns out that the Debye-Waller factor in atom-surface scattering remains an aspect of great theoretical interest[151]. Problems arise due to the relatively long range of the interaction potential and because the collisions are no longer fast enough to be considered impulsive[151–153]. Corrections have been proposed to account for the long interaction time with respect to the vibrational phonon periods by Levi and Suhl[154] as well as for the presence of the attractive atom-surface interaction known as the Beeby effect[46]. While the Beeby effect is accounted for as described in the following, the first correction requires the knowledge of the surface phonon spectrum and is rather involved. However, by considering comparatively small parallel momentum transfers as it is the case in the presented HAS experiments, equation 7.5 can be considered to be approximately correct[39,47,133] and will form the basis for the following analysis[1].
Within this description the attractive part of the atom-surface interaction potential can be taken into account by using the Beeby correction. The attractive part of the potential has the effect of first accelerating the incoming He atoms and then decelerating the scattered atoms as they leave the surface. Hence, the influence of the attractive well is considered by replacing the perpendicular momentum transfer Δk_z by[39,47]:

$$\Delta k_z' = k_i \left[\sqrt{\cos^2(\theta_f) + \frac{D}{E_i}} + \sqrt{\cos^2(\theta_i) + \frac{D}{E_i}} \right] \tag{7.6}$$

In doing so the attractive part of the potential is included by assuming a spatially uniform well of depth D which is usually in the range of 4-10 meV for HAS[39].
In the case of the specular beam, $\theta_i = \theta_f$ holds and the Debye Waller factor (equation 7.5) together with the Beeby correction can be expressed as:

$$W(T_S) = \frac{12m\left[E_i\cos^2(\theta_i) + D\right]T_S}{Mk_B\theta_D^2} \tag{7.7}$$

[1] According to[154] and[35] the collision time in the present experiments can be estimated to be in the range of $\tau_c = 4.7 \times 10^{-14}$ s and $\tau_c = 6.5 \times 10^{-14}$ s depending on the incident energy of the beam. Using this time as a period of a phonon vibration this gives rise to an energy value of $E_c = 89$ meV and $E_c = 63$ meV, respectively. Since phonon states above the energy k_BT_S are hardly populated they do not contribute to the attenuation of elastic intensities. Hence if $E_c \gg k_BT_S$ is fulfilled the collision can be regarded as fast and equation 7.5 can be used without any restrictions. For $T_S = 100$ K, $k_BT_S \approx 0.1\ E_c$ holds and the collision can be considered as fast. At $T_S = 450$ K this value is $\approx 1/2\ E_c$ and it is more likely that corrections occur due to the Levi effect. On the other hand, from the experimental trend it seems that this effect is still quite small which is why it has not been considered.

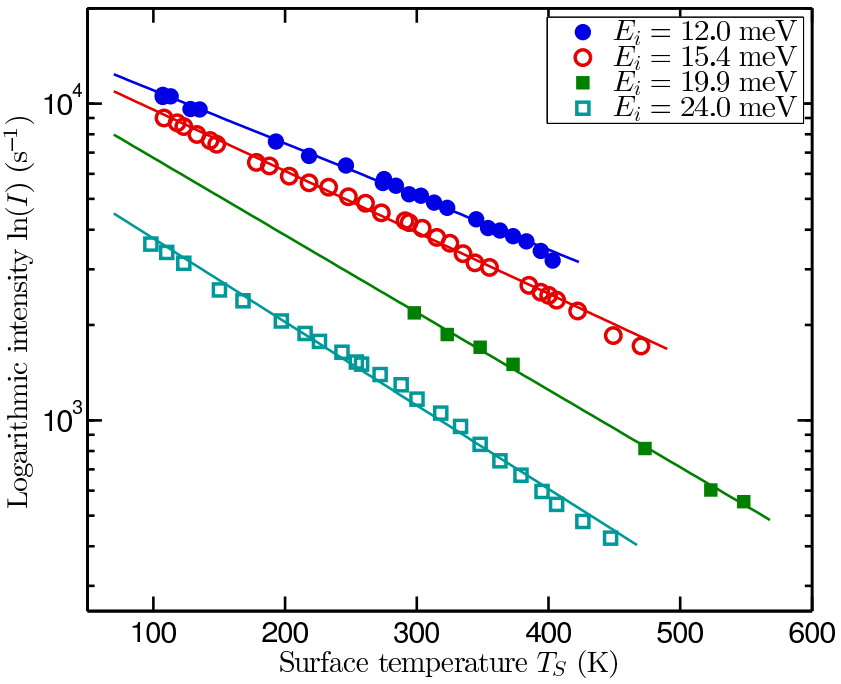

Figure 7.2: Decay of the logarithmic specular peak intensity ln(I) versus surface temperature T_S for four different incident beam energies E_i. In all cases the measurements exhibit a linear decay.

where m is the impinging particle mass and the momentum was replaced by the incident beam energy using $k_i^2 = 2mE_i/\hbar^2$. Although equation 7.7 is strictly valid only for the specular beam, it is also a reasonable approximation for final angles θ_f that are not too different from the incident angle θ_i.

According to equation 7.1, a plot of ln(I) versus the surface temperature T_S gives rise to a linear decay within the Debye model whereupon the surface Debye temperature can be calculated from the slope. In figure 7.2 the decay of the specular peak intensity versus the surface temperature is depicted. For the peak intensities the area of a Gaussian fit of the scattered intensity (figure 7.1) was used. The measurement shows for all four different incident beam energies E_i an almost perfect linear decay.

Using equation 7.5 (equation 7.7 for the specular geometry) the surface Debye temperature can be determined from the experimental data points. In doing so it is important to keep in mind that the surface Debye temperature and vibration amplitudes are usually related to the motion of the ion cores. However, He atoms are scattered by the electron density above the first atomic layer rather than the ion cores. In the case of inelastic scattering this corresponds to a scattering of the He atoms by phonon-induced charge density oscillations[155]. The association of these charge density oscillations with the surface Debye temperature, i.e., with the motion of the ion cores is possible due to the electron-phonon coupling.

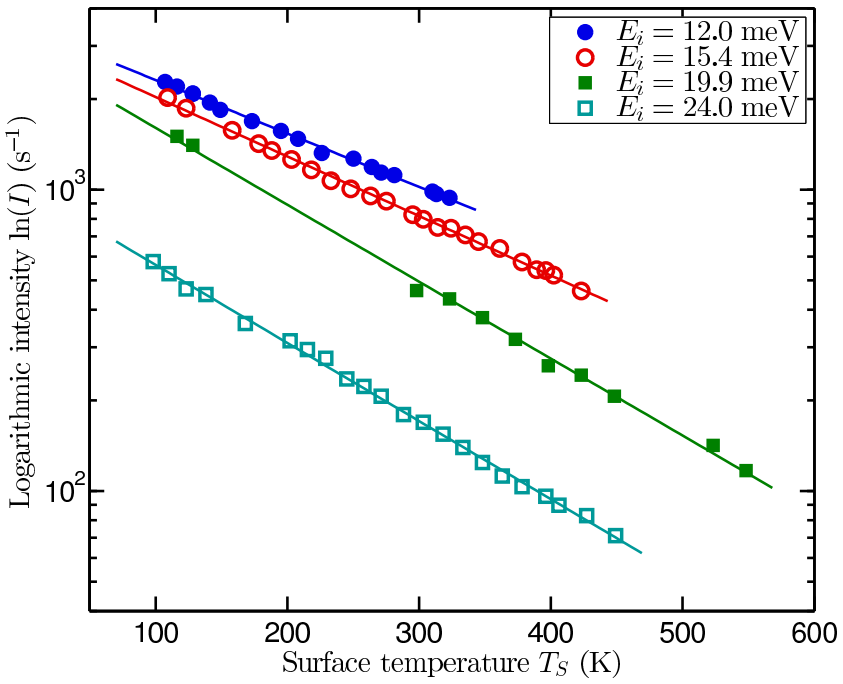

Figure 7.3: Decay of the logarithmic peak intensity ln(I) with increasing surface temperature T_S of the first order diffraction peak along $\overline{\Gamma K}$. The measurements at four different incident beam energies E_i are plotted.

Indeed, precaution must be taken when comparing HAS measurements with LEED data due to the different nature of the scattering processes: LEED experiments usually include the measurement of scattered electrons that are penetrating into the first layers of the bulk.
Nevertheless, these simple equations have proven to serve as a good approximation in the case of HAS[39,47,133] and they have been applied successfully for other semimetal surfaces such as Bi(111) where the results are similar to those obtained from LEED measurements[5].
Thus using equation 7.7 together with 7.1, the surface Debye temperature is determined by applying a three-parameter fit to the experimental data (I_0, D and θ_D) and assuming that M is equal to the mass of a single Sb atom. Using the best-fit results a surface Debye temperature $\theta_D = (155 \pm 3)$ K is obtained and a well depth of $D = (4.5 \pm 0.5)$ meV. Hence the surface Debye temperature of Sb(111) is reduced significantly with respect to the bulk value which is 211 K[18].
According to the theoretical approximation of van Delft[122] the surface Debye temperature should be reduced by a factor of $1/\sqrt{2}$ with respect to the bulk value. Even though this approximation accounts only for the nuclear motion while HAS probes the oscillations of the electron density above the first atomic layer, this value is in good agreement with our experimental findings.

The same analysis can be applied to the first order diffraction peaks measured along the $\overline{\Gamma K}$ azimuth. A plot of $\ln(I)$ versus the surface temperature T_S for the first order diffraction peak is shown in figure 7.3. From the slope of the linear fits, the Debye temperature can be calculated using equation 7.5. Considering that the mirror condition $\theta_i = \theta_f$ no longer holds, the perpendicular momentum transfer is calculated using equation 7.6, assuming that the well depth equals the previously determined value: $D = 4.5$ meV. The surface Debye temperature determined from the first order diffraction peaks is $\theta_D = (150 \pm 6)$ K, in accordance with the value determined from the specular peak. Furthermore, the perpendicular mean-square displacement $\langle u_z^2 \rangle$ can be extracted from Debye-Waller attenuation measurements when the Δk_z-dependence of the Debye-Waller exponent is considered. When including the temperature dependence of the Debye-Waller exponent, i.e. the derivative of equation 7.3 gives rise to[47,149]:

$$\sigma \equiv -\frac{d(2W)}{dT_S} = -\left[\Delta k_z^2 \frac{d\langle u_z^2 \rangle}{dT_S} + \Delta K^2 \frac{d\langle U^2 \rangle}{dT_S}\right] \tag{7.8}$$

For the specular geometry only the component perpendicular to the surface remains in equation 7.8. Together with the Beeby correction (equation 7.6) for $\theta_i = \theta_f$:

$$\Delta k_z^2 = 4k_i^2 \left[\cos^2(\theta_i) + \frac{D}{E_i}\right] \tag{7.9}$$

the derivative of the Debye-Waller exponent (σ) times the incident energy E_i becomes:

$$E_i \cdot \sigma = 4k_i^2 \frac{d\langle u_z^2 \rangle}{dT_S} \left[E_i \cos^2(\theta_i) + D\right] \tag{7.10}$$

We find that the slope of equation 7.10 is proportional to $d\langle u_z^2 \rangle / dT_S$ and the well depth D can be determined from the intercept.
In figure 7.4, $E_i \cdot \sigma$ is plotted versus $E_i \cos^2(\theta_i)$ for the measurements from figure 7.2. A linear fit to the data yields a slope of -0.0114 and an intercept of 0.0338. Taking $k_i = 6.8$ Å^{-1}, $d\langle u_z^2 \rangle / dT_S = (6.1 \pm 1.2) \times 10^{-5}$ Å^{2}K^{-1} and the well depth determined from the intercept is (3.1 ± 1.8) meV. Thus the value of D is consistent with the value determined from the Debye-Waller fits within the uncertainty.

The mean-square displacement $\langle u_z^2 \rangle$ can also be calculated theoretically within the harmonic approximation using[156]:

$$\langle u_z^2 \rangle = \frac{3\hbar^2}{M k_B \theta_D} \left[\frac{1}{x^2} \int_0^x \frac{t}{e^t - 1} dt + \frac{1}{4}\right] \tag{7.11}$$

with $x = \theta_D / T_S$. In the high temperature limit the contribution from zero-point motion can be neglected and equation 7.11 becomes:

$$\langle u_z^2 \rangle = \frac{3\hbar^2}{M k_B \theta_D^2} T_S \tag{7.12}$$

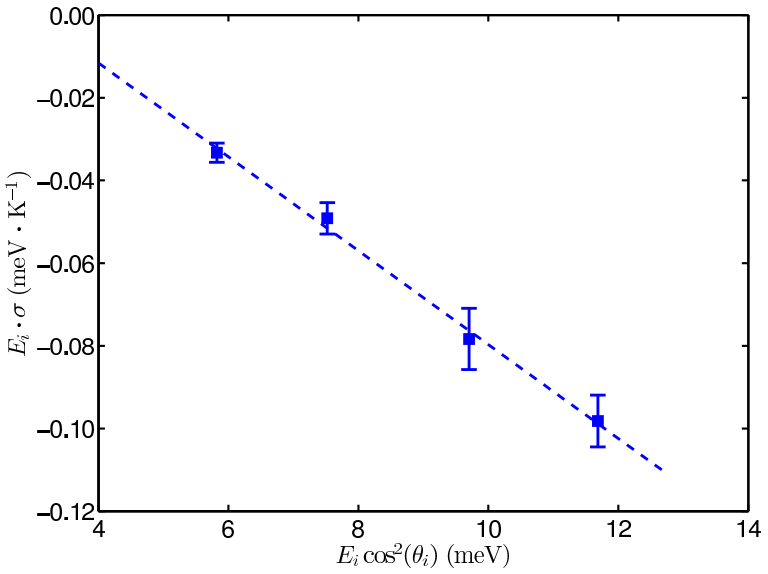

Figure 7.4: Linear fit to the incident beam energy dependence of the Debye-Waller factor. The derivative of the Debye-Waller exponent, σ, times the incident energy E_i is plotted versus $E_i \cos^2(\theta_i)$. The slope and the intercept characterize the perpendicular mean-square displacement and the well depth D, respectively.

Hence $\langle u_z^2 \rangle$ is proportional to T_S at all but the lowest temperatures[55] and it can be readily compared with the value determined from the derivative of the Debye-Waller factor. For the Sb(111) surface at room temperature ($T_S = 298$ K), $\langle u_z^2 \rangle = 1.5 \times 10^{-2}$ Å^2 according to equation 7.11. Using the experimentally determined value of $d\langle u_z^2 \rangle / dT_S$ the perpendicular mean-square displacement at room temperature is $(1.8 \pm 0.4) \times 10^{-2}$ Å^2 in good agreement with the theoretical value.

7.4 Conclusion

The thermal attenuation in the diffraction of He from Sb(111) was studied in a temperature range between 98 K and 447 K. The surface Debye temperature of Sb(111) was determined for the first time using an approximative description which was originally derived for electron scattering. A typical Debye-Waller behavior revealed a surface Debye temperature of (155 ± 3) K from the measurements of the specular peak and (150 ± 6) K from the measurements of the first order diffraction peak intensity. The best-fit results of the data give rise to a well depth of $D = (4.5 \pm 0.5)$ meV for the He-Sb(111) atom-surface interaction potential. The perpendicular mean-square displacement for Sb(111) is determined to be $(1.8 \pm 0.4) \times 10^{-2}$ Å^2 at room temperature which is found to be in good agreement with the theoretical prediction.

8 The Helium-Surface Interaction Potential of Sb(111) from Scattering Experiments and Close-Coupling Calculations

The following corresponds to a publication by
Michael Mayrhofer-Reinhartshuber, Patrick Kraus, Anton Tamtögl, Salvador Miret-Artés, and Wolfgang E. Ernst in *Phys. Rev. B*, **88**:205425-1 - 205425-11, November 2013[32].

The author of this thesis was responsible for

- the LEED and AES measurements,
- the main parts of the HAS measurements of Sb(111) (see figures 8.2, 8.5, and 8.7),
- supporting the analyses of SAR and drift spectra (see sections 8.2.2 and 8.4.3),
- analysis of KF (see section 8.4.4),
- and the authorship of the abstract and sections 8.2, 8.3, 8.4, and 8.5.

The contributions of the co-authors are listed below:

- P. Kraus: SAR analysis, Kinematic Analysis, CC calculations, supporting authorship of section 8.2.3
- A. Tamtögl: HAS-measurements, authorship of the introduction (section 8.1)
- S. Miret-Artés: CC calculations
- W.E. Ernst: supervision (experiment, theory, publication), laboratory, funding

Abstract

Helium atom scattering (HAS) was used to study the antimony Sb(111) surface beyond the hard-wall model. HAS angular distributions and drift spectra show a number of selective-adsorption resonance features, which correspond to five bound-state energies for He atoms trapped in the surface-averaged He-Sb(111) potential. As their best representation, a 9-3 potential with a depth of 4.4 ± 0.1 meV was determined. Furthermore, the charge density corrugation of the surface was analyzed using close coupling calculations. By using a hybrid potential, consisting of a corrugated Morse potential (short-range) and a 9-3 potential (long-range), a peak-to-peak corrugation of 17% was obtained. The kinematic focusing effects that occured were in good agreement with surface phonon dispersion curves from already published density functional perturbation theory calculations.

8.1 Introduction

The semimetal surfaces of antimony have recently attracted great interest since antimony is one of the basic building blocks for a number of compounds belonging to the class of topological insulators[9,85]. Moreover, Sb(111) nanofilms have proven to be an ideal test bed for the experimental investigation of topoelectronic phase transitions[84]. The film thickness and bonding to the substrate can be used to tune the electronic and spintronic properties of thin Sb films[129,157]. Hence Sb(111) films do offer attractive features for potential applications in spintronics such as a tunable band gap and spin polarization[83].

The electronic surface states of antimony have been studied both experimentally and theoretically,[10,79,97–99,127,128] whereas for the surface dynamics of Sb(111), only theoretical investigations are available[10]. Furthermore, the atom-surface interaction as observed in scattering experiments has not been addressed with the exception of a study of the adsorption of water on Sb(111)[100]. A detailed study of the He-Sb(111) atom-surface interaction is particularly interesting not only from a fundamental point of view but also as a necessary ingredient for surface phonon measurements.

In order to understand the atom-surface interaction at semimetal surfaces helium atom scattering (HAS) is ideally suited. Experimental information about the detailed shape of the physical adsorption is most easily gained by analyzing elastic HAS intensities[48]. While semimetal surfaces are normally conducting[80,97,98] and therefore possess free-surface electrons, in HAS experiments they are found to be strongly corrugated[5,60], unlike the low-index surfaces of ordinary metals which are perfectly flat. This may be caused by the concentration of surface electrons and holes at the Fermi energy into comparatively narrow pockets[80,97,98]. Hence semimetals are particularly interesting for HAS studies since corrugation is necessary for the occurrence of inelastic bound-state resonances which can enhance certain phonon events[6,7]. It was recently shown that

inelastic HAS is capable of detecting sub-surface phonon modes which are localized in layers beneath the surface in the case of metal and semimetal surfaces[6,7,134]. The depth to which these phonons are observable is determined by the range of the electron-phonon (e-ph) interaction and inelastic HAS intensities can be used to infer the corresponding e-ph coupling strength[134,155].

In a detailed analysis of the intensities on the Bi(111) semimetal surface, a mechanism for the enhancement of inelastic HAS intensities from subsurface optical modes was singled out[8]. This mechanism which is called the surfing condition[158], is specific to semimetal surfaces and gives rise to a strong resonance enhancement of the scattered intensities under certain kinematic conditions[8]. It involves the selective adsorption of the incident He atom into a surface bound state due to the atom-surface interaction potential. In the case of the "surfing" situation the impinging He atom enters the bound-state inelastically by creating a phonon and the trapped atom then travels at the same speed as the group velocity of the phonon along the surface. This unusual form of an atomic polaron gives rise to a strong coupling with otherwise weak subsurface phonons[8].

Semimetal surfaces also hold the possibility of detecting electron-hole excitations via HAS due to the fact that electrons on these surfaces are restricted to narrow pockets in the parallel momentum space[6,7]. Furthermore, e-ph scattering processes at the Fermi level are likely to cause Kohn anomalies in the surface phonon dispersion[6,7,159], an effect which has been observed with HAS for the topological insulator surfaces Bi_2Se_3 and Bi_2Te_3[160–162].

In the present work the elastic diffraction peaks of He scattered from Sb(111) are analyzed using the exact close coupling (CC) method[48]. This method goes beyond the simple hard-wall approximation and has been mainly applied to ionic and metallic surfaces[39]. In doing so a surface corrugation function of the system He-Sb(111) is obtained. A series of modulations of the elastic intensities due to the so–called selective adsorption resonances (SARs) is used to determine the bound-state energies of the system He-Sb(111). These energies, usually extracted from drift spectra, allow a reliable prediction of the elastic resonance conditions and are used to fit an atom-surface interaction potential. Furthermore, an enhancement of the inelastic background due to the kinematic focusing (KF) effect[158] has also been observed. The obtained atom-surface interaction potential not only is a prerequisite for surface phonon measurements but also can be exploited to enhance certain phonon events which would otherwise be too weak.

8.2 Theory

In this section the minimum theoretical background necessary for the successive analysis of our measurements is presented. Throughout this work, square wave vectors quantities

are given in energy units, with $\hbar^2/2m = 1$, where m is the mass of the incident particles (He atoms). Furthermore, the standard notation in this field is used; that is, vectors parallel to the surface are written as boldface capital letters, and three-dimensional vectors as boldface lower-case letters.

8.2.1 The Atom-Surface Interaction Potential

In the presented experiments He atoms with a well defined kinetic energy impinge on the sample surface. Forces originating from the interaction with each individual surface particle act on the approaching He atoms. The London dispersion (van der Waals) force, appearing because of instantaneously induced dipoles, accelerates the He atom towards the surface. The interaction between electrons of the surface and the shell of the He atom acts as a short-range counterpart, the Pauli repulsion. In contrast to electron or neutron scattering, He atoms are repelled already by the electron density a few Ångströms above the topmost atomic layer.

9-3 Potential

Considering the contribution of these forces, the interaction between a He atom and a surface particle can be described by a 12-6 (Lennard-Jones) potential. Since one He atom is interacting with all atoms of the surface, these Lennard-Jones potentials must be summed. In the continuum limit the sums are replaced with integrals along the three space coordinates. The resulting integration over the whole semiinfinite lattice provides a 9-3 atom-surface potential given by[8]

$$V(z) = \frac{\sqrt{27}}{2} D \left[\left(\frac{\sigma}{z}\right)^9 - \left(\frac{\sigma}{z}\right)^3 \right], \tag{8.1}$$

with z the normal distance from the surface, D the well depth of the attractive part and σ the distance, at which the potential is zero.

Using the distorted wave Born approximation[36] the eigenvalues E_n (energy of the n^{th} bound-state) for this potential are given by

$$E_n \simeq -D \left[1 - \frac{\pi\hbar}{3.07} \frac{n + \frac{1}{2}}{\sigma\sqrt{2mD}} \right]^6 . \tag{8.2}$$

As recently shown by Kraus et al.[8], this description of the bound states is suitable for semimetal surfaces, such as Bi(111). Therefore, it is also applied for the analysis of bound states at the Sb(111) surface from HAS measurements of selective adsorption resonances.

Corrugated Morse Potential (CMP)

For the analysis of the electronic corrugation, represented by the corrugation function $\xi(\mathbf{R})$, the corrugated Morse potential (CMP)[163] is very often used in the CC framework. It can be written as

$$V(\mathbf{R},z) \;=\; D\left[\frac{1}{\upsilon_0}e^{-2\chi(z-\xi(\mathbf{R}))} \;-\; 2e^{-\chi z}\right], \tag{8.3}$$

with $\mathbf{r}=(\mathbf{R},z)$. χ is the stiffness parameter, and υ_0 the surface average over $e^{2\chi\xi(\mathbf{R})}$ (eq. (8.7) for $\mathbf{G}=0$). In reciprocal space, each lattice point of the surface can be reached with a surface reciprocal-lattice vector $\mathbf{G}$,

$$\mathbf{G} = h\mathbf{a}^* + k\mathbf{b}^*, \tag{8.4}$$

with $\mathbf{a}^*$ and $\mathbf{b}^*$ the basis vectors of the reciprocal lattice and h, k integer values. Within this study, a certain $\mathbf{G}$ is indicated as (h,k). Since $\xi(\mathbf{R})$ is periodic, equation (8.3) can be expanded in a Fourier series with

$$V(\mathbf{R},z) \;=\; V_0(z) + \sum_{\mathbf{G}\neq 0} V_{\mathbf{G}}(z)e^{i\mathbf{G}\cdot\mathbf{R}}, \tag{8.5}$$

where $V_0(z)$ is the bare potential and the Fourier coefficients are denoted $V_{\mathbf{G}}$. They can be expressed analytically through the corrugation Fourier coefficients $\upsilon_{\mathbf{G}}$

$$V_{\mathbf{G}} \;=\; D\frac{\upsilon_{\mathbf{G}}}{\upsilon_0}e^{-2\chi z}. \tag{8.6}$$

$\mathbf{G}\neq 0$ components of equation (8.6) are also called the coupling terms of the CMP. The coefficients $\upsilon_{\mathbf{G}}$ are given by

$$\upsilon_{\mathbf{G}} \;=\; \frac{1}{\Sigma}\int_{\Sigma} e^{-\mathrm{i}\mathbf{G}\cdot\mathbf{R}}e^{2\chi\xi(\mathbf{R})}d\mathbf{R}, \tag{8.7}$$

with Σ the area of the surface unit cell. The bare potential of the interaction can be written as

$$V_0(z) \;=\; D\left[e^{-2\chi z} \;-\; 2e^{-\chi z}\right]. \tag{8.8}$$

The bound states of the bare potential are described by an analytical expression[164]

$$E_n \;=\; -D + \hbar\omega\left(n+\frac{1}{2}\right)\left[1-\frac{(n+\frac{1}{2})}{2\gamma}\right] \tag{8.9}$$

with n a positive integer, $\gamma=\frac{2D}{\hbar\omega}$ and $\omega=\sqrt{\frac{2\chi^2 D}{m}}$.

Hybrid Morse Potential (HMP)

To include a more sensible, long-range interaction of the potential, a hybrid form was introduced[31]

$$V_0 = \begin{cases} D\left[e^{-2\chi z} - 2e^{-\chi z}\right] & , z \leq z_\mathrm{p}, \\ -\frac{C_3}{(z-z_\mathrm{e})^3} & , z > z_\mathrm{p}, \end{cases} \tag{8.10}$$

where both constants C_3 and z_e are chosen in a way that guarantees the continuity of the overall potential and its derivative at the inflection point z_p. While the bound states of the Morse potential can be described analytically, the ones for the HMP must be calculated numerically. Since the short-range part of the HMP is equal to the CMP, for CC calculations the same coupling terms eq. (8.6) can be used. The long-range part takes into account the asymptotic behavior of the more realistic 9-3 potential eq. (8.1).

8.2.2 Selective Adsorption Resonances

Selective adsorption resonances (SAR) are observed, when an impinging He atom enters in one of the bound states of the atom-surface interaction potential. After a short lifetime of typically 10^{-12} s, the atom leaves the surface[62,63]. Due to a phase shift of its wave function, the interference with other scattered atoms gives rise to a modulation of the scattered intensity. Several types of resonant scattering processes exist[64–66], the most important for the present work are described below.

In the first type, a particle with an initial state (E_i, Θ_i) is elastically scattered into a bound state of energy $-|E_n|$. Thereafter, it leaves the surface potential elastically into a final state. Due to a phase shift obtained during this process, these atoms interfere with directly elastically scattered atoms and result in intensity modulations of the elastic peaks[64].

In the second type, an incident He atom, which has elastically entered a bound state, is scattered inelastically into a final state. Due to the obtained phase shift relative to directly inelastically scattered particles, interference and hence features between the elastic peaks of the angular scans can also be observed. For this resonance type, interaction with a phonon is necessary. This scattering is also known as the phonon assisted SAR process[64,67,68].

By using the conservation laws for energy and parallel momentum, the condition for an elastic selective adsorption resonance can be obtained from[65,66]

$$\mathbf{k}_\mathrm{i}^2 = \left(\mathbf{k}_\mathrm{i} \sin\Theta_\mathrm{i} + G_\parallel\right)^2 + G_\perp^2 - |E_n|\,, \tag{8.11}$$

where $\mathbf{k}_\mathrm{i}$ denotes the incident wave vector and Θ_i is the incident angle with respect to the surface normal. $G_\parallel$ and $G_\perp$ are the parallel and perpendicular components of the reciprocal lattice vector $\mathbf{G}$ of the surface with respect to the plane of incidence. Resonances that have a non-zero $G_\perp$ component are referred to as *out-of-plane*; resonances

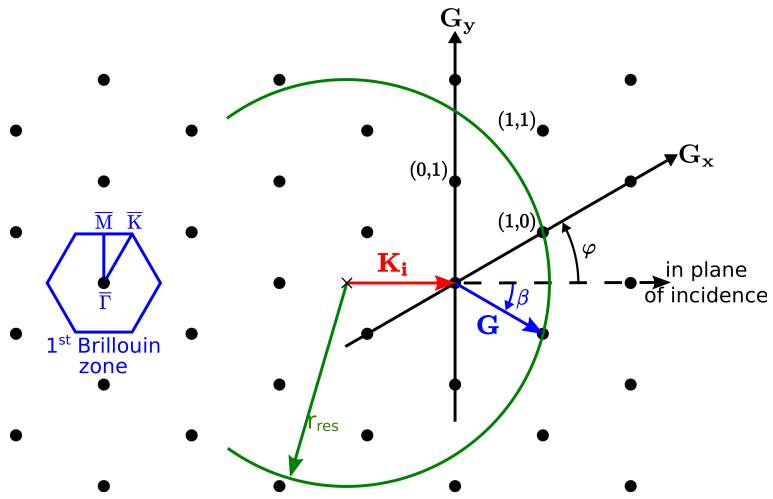

Figure 8.1: A geometrical representation of the resonance condition eq. (8.11) is shown in reciprocal space together with the first Brillouin zone for the first layer atoms of Sb(111). The sum of the vectors $\mathbf{K}_\mathrm{i} = \mathbf{k}_\mathrm{i} \sin\Theta_\mathrm{i}$ and $\mathbf{G}$, which leads to a resonant transition, lies on a circle with the radius $r_{res}^2 = \mathbf{k}_\mathrm{i}^2 + |E_n|$.

with $G_\perp = 0$ as *in-plane*. To fulfill condition eq. (8.11) in the experiment, either Θ_i or $\mathbf{k}_\mathrm{i}$ can be varied while the other is held constant. A geometrical representation of the resonance condition together with the reciprocal lattice of the first Sb(111) layer is depicted in figure 8.1.

8.2.3 Close-Coupling Calculations

In the CC formalism, helium atoms are considered to be structureless and non-penetrating, while the surface is considered to be statically corrugated and periodic. In a purely elastic scattering scheme, an impinging particle with wave vector $\mathbf{k}_\mathrm{i}$ is described by the time-independent Schrödinger equation

$$\left[-\nabla^2 + V(\mathbf{r}) - \mathbf{k}_\mathrm{i}^2\right] \Psi(\mathbf{r}) = 0. \tag{8.12}$$

Due to the elastic scattering from a periodic surface, the conservation of particle momentum is described by the Bragg condition

$$\Delta\mathbf{K} = \mathbf{K}_\mathrm{f} - \mathbf{K}_\mathrm{i} = \mathbf{G}, \tag{8.13}$$

with $\mathbf{K}_\mathrm{f}$ the wave vector component of the scattered He atom parallel to the surface. Due to the surface periodicity, the interaction potential as well as the wave function can be Fourier expanded. While the potential is given by equation (8.5), the wave function then reads

$$\Psi(\mathbf{r}) = \sum_{\mathbf{G}} \Psi_{\mathbf{G}}(z) \cdot e^{i(\mathbf{K}_\mathrm{i}+\mathbf{G})\cdot\mathbf{R}}. \tag{8.14}$$

If both expressions are substituted into equation (8.12), the following set of coupled equations for the diffracted waves is obtained

$$\left[\frac{\mathrm{d}^2}{\mathrm{d}z^2} + \mathbf{k}_{\mathbf{G},z}^2 - V_0(z)\right] \Psi_{\mathbf{G}}(z) = \sum_{\mathbf{G}' \neq \mathbf{G}} V_{\mathbf{G}'-\mathbf{G}}(z) \Psi_{\mathbf{G}'}(z), \tag{8.15}$$

with $\mathbf{k}_{\mathbf{G},z}$ the z-component of the particle wave vector after scattering given by

$$\mathbf{k}_{\mathbf{G},z}^2 \;=\; \mathbf{k}_{\mathrm{i}}^2 \;-\; (\mathbf{K}_{\mathrm{i}} + \mathbf{G})^2. \tag{8.16}$$

Each of the equations (8.15) includes a characteristic effective potential $V_0 + (\mathbf{K}_{\mathrm{i}} + \mathbf{G})^2$, where the second term is the asymptotic energy, which is dependent on $\mathbf{G}$ and the incident scattering conditions. All of these effective potentials have a continuous as well as a discrete spectrum. The wave functions associated with the continuum are usually expressed as $|\mathbf{K}_{\mathrm{i}} + \mathbf{G}, \mathbf{k}_{\mathbf{G},z}^2\rangle$. $|\mathbf{K}_{\mathrm{i}} + \mathbf{G}, n\rangle$ denotes discrete wave functions with n as the number for the n^{th} bound state of the He-surface interaction potential. In this study the term *channel* is used for each effective potential and is usually denoted by the corresponding $\mathbf{G}$-vector: the (h, k) *channel*. Since in a fixed-angle apparatus the angle of incidence, and thus also $\mathbf{K}_{\mathrm{i}}$ must be changed to measure a full angular spectrum, the asymptotic energies of the respective channels move. This phenomenon is usually called *moving thresholds*[48,165]. As can be seen in equation (8.16), depending on the absolute value of $\mathbf{G}$, the respective $\mathbf{k}_{\mathbf{G},z}^2$ of a channel can be either positive or negative. Through this, two elementary kinds of scattering channels can be distinguished. For $\mathbf{k}_{\mathbf{G},z}^2 > 0$, the channels are called *open*; they are energetically accessible. In the case of $\mathbf{k}_{\mathbf{G},z}^2 < 0$, the channels are called *closed*; they are energetically forbidden channels. Though they do not produce observable features directly, a number of closed diffraction channels must be included in the simulations to achieve numerical convergence for the outcome. The higher the expected surface corrugation, the stronger are the Fourier components of the interaction potential $V_{\mathbf{G}-\mathbf{G}'}(z)$ and the more channels must be included in the calculations[48]. Nevertheless, the number of channels N has to be restricted since the computational time scales with N^3 [166].

8.3 Experimental Details

8.3.1 The Sb(111) Surface Structure

Bulk antimony exhibits a rhombohedral crystal structure (space group R$\bar{3}$m). An important feature of this structure is the puckered bilayers of atoms perpendicular to the $\langle 111 \rangle$ direction. In contrast to the strong covalent bonding within these bilayers, the interbilayer bonds are of van der Waals character. Thus, the (111) surface of Sb is its natural cleavage plane[93,95], which results in easily available Sb(111) crystal samples. The topmost layer has a hexagonal structure with an atomic spacing of a=(4.3084±0.0002) Å[92].

Including second layer atoms, the sixfold symmetry of the first layer is broken to a three-fold symmetry. Nevertheless, in the HAS measurements in this study, the energy of the incident helium atoms was low enough to neglect influences of other than first-layer atoms[6].

Thorough investigations of the electronic properties of Sb(111) revealed metallic surface states of the otherwise semimetallic properties of the bulk[97–99]. At the $\overline{\Gamma}$ point a hexagonal-like cut through the Fermi Surface (FS) was observed. Anisotropies of the FSs due to an anisotropy of the spin-orbit interaction lead to a three-fold symmetry of the intensity of six lobes surrounding this central pocket. Furthermore, at the $\overline{\mathrm{M}}$ points oval-shaped electron pockets were detected[97,99]. Although a flat surface electron-density was expected due to the FS electronic states found in all directions, with HAS measurements a surprisingly high peak-to-peak corrugation of the electron-density was recently observed[60].

8.3.2 Experimental Setup

The measurements presented in this work were conducted on a HAS apparatus (H.Å.N.S.) with a fixed source-target-detector geometry $\Theta_{\mathrm{SD}} = 91.5°$. By varying the temperature of the nozzle which was used for the creation of the He beam, the energy of the He atoms could be tuned between 11 and 35 meV. More details about the apparatus and its dimensions are given in a previous paper[4]. The Sb(111) single crystal used in the study was a disc with a diameter of approximately 15 mm which was cleaned by Ar^+ sputtering and annealing to 475 K prior to the measurements. The cleanliness and surface order were checked by Auger electron spectroscopy and low energy electron diffraction, respectively[60]. All HAS measurements were performed with the crystal at room temperature (300 K). For angular scans the incident angle Θ_{i} of the monoenergetic He beam with respect to the surface normal was altered by rotating the sample. The angular resolution in these measurements was 0.1°. Drift spectrum measurements were obtained by varying the incident energy of the He atoms while the incident angle was held constant.

8.4 Results

8.4.1 He-Sb(111) Potential

Angular HAS scans were performed and the observed resonance features were used to extract bound-state energies. Figure 8.2(a) displays the data resulting from a measurement along the $\overline{\Gamma\mathrm{K}}$ direction. The increased intensity (solid line) of the measured He signal is plotted versus the incident angle of the He beam. The dashed curves depict the resonance conditions given by our experimental geometry, the experimental parameter

Table 8.1: Bound-state energies experimentally determined from HAS measurements and analytically calculated for the fitted 9-3 He-Sb(111) interaction potential with $D = (4.41 \pm 0.09)$ meV and $\sigma = (6.3 \pm 0.3)$ Å.

Bound State	Experiment Energy (meV)	9-3 Potential (8.2) Energy (meV)
E_0	-3.7 ± 0.2	-3.7 ± 0.1
E_1	-2.6 ± 0.2	-2.6 ± 0.2
E_2	-1.86 ± 0.02	-1.8 ± 0.2
E_3	-1.17 ± 0.02	-1.2 ± 0.1
E_4	-0.70 ± 0.02	-0.8 ± 0.1

$\mathbf{k}_\mathrm{i}$ and for a given $\mathbf{G}$-vector. If this line intersects the energy of a bound state, the condition eq. (8.11) for selective adsorption resonances is fulfilled and maxima or minima may be observable in the measured signal. These features between the angular positions of the Bragg peaks originate from phonon assisted SAR.

To determine the He-Sb(111) interaction potential, in the first step the bound state energies have to be estimated. For that purpose, these energies (solid, horizontal lines in figure 8.2) were varied until the angular positions of their intersections with the resonance conditions were in good agreement with the features in the measured signal. In the measurement along $\overline{\Gamma\mathrm{K}}$ the distinct peak at $\Theta_\mathrm{i} = 36°$ and the modulations around $\Theta_\mathrm{i} = 30°$ were assigned to the in-plane resonance with the $\mathbf{G}$-vector (1,1) ((1,1)-channel), whereas the high peak at $\Theta_\mathrm{i} = 50.5°$ and the small enhancements around $\Theta_\mathrm{i} = 59°$ were associated with the out-of-plane (1,0)-channel. This procedure resulted in five bound state energies $E_{i=0\ldots4}$, which are listed in table 8.1.

The angular scan along $\overline{\Gamma\mathrm{M}}$ is shown in figure 8.2(b). Also in this direction several features from selective adsorption resonance effects appear, which were included in the fitting procedure described above. The peaks at $\Theta_\mathrm{i} = 30°$ and $\Theta_\mathrm{i} = 32°$ were associated with the (1,1)-channel. The shoulders of the specular (0,0)-peak arise from resonances with the (1,0)-channel, the shoulders of the (1,0)-peak from the (0,1)-channel. Around $\Theta_\mathrm{i} = 55°$ narrow oscillations appear, which may be produced by either the (1,0) or the (0,1) channel.

It is remarkable that features originating from resonance effects with E_0 seem to result in quite small, broad intensity enhancements in the angular scans in contrast to features with bound-state energies E_1 to E_4, which yield narrower shapes with higher intensities.

With the determined energies of the bound states, the laterally averaged He-Sb(111) interaction potential was derived. Therewith, the model potential was optimized and its analytically calculated eigenvalue spectrum was compared to the measured values with a least-squares fit. As it is a good representation of the surface, the 9-3 potential

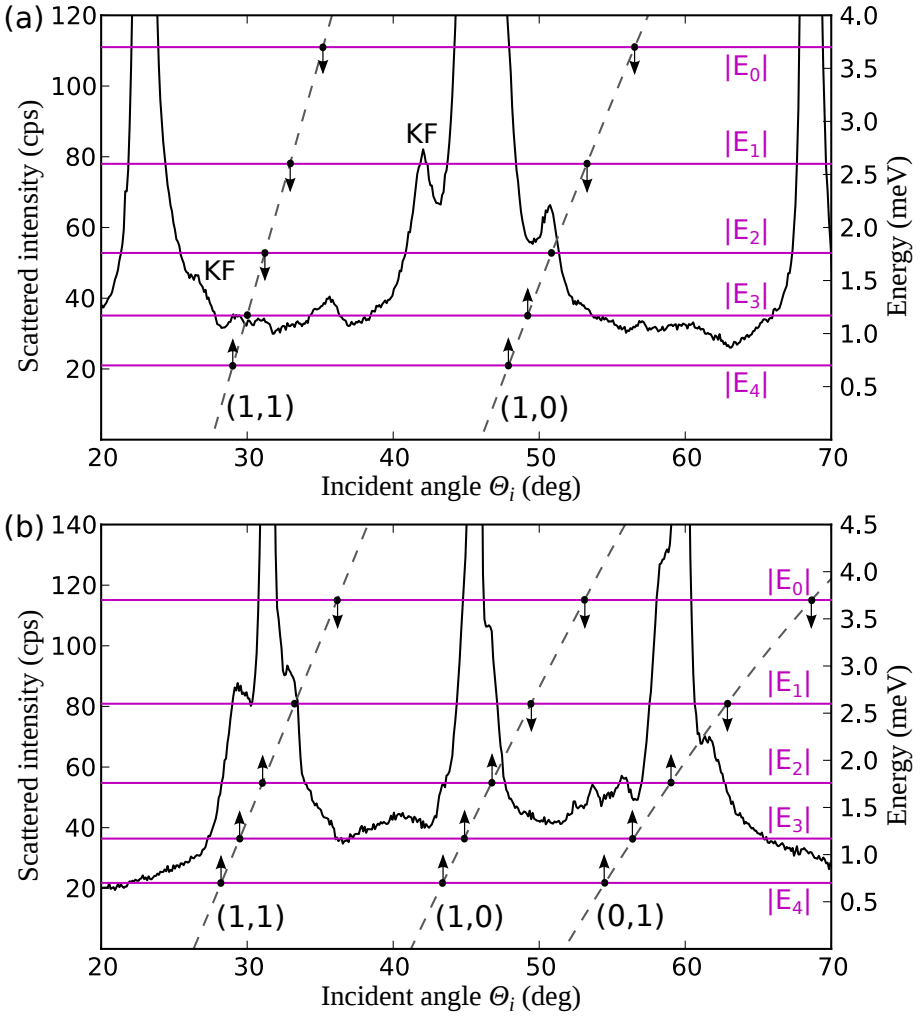

Figure 8.2: (a): Angular distribution of the HAS intensity (left-hand ordinate scale) from Sb(111) along the $\overline{\Gamma K}$ surface direction at a beam energy of 15 meV. In addition to the specular peak (45.75°) and the two closest Bragg peaks, further features corresponding to selective adsorption processes are identifiable. The five bound-state energies, that were found with our measurements, are depicted as horizontal lines (right-hand ordinate scale). The two dashed lines correspond to the resonance conditions for two **G** vectors [(1,0), (1,1)] in our experimental geometry and are labeled accordingly. Two additional peaks are attributed to kinematic focusing (KF) effects, which are discussed in section 8.4.4.
(b): Same as (a) for an angular scan along the $\overline{\Gamma M}$ direction with resonance conditions for three **G** vectors [(1,0), (0,1), (1,1)].

eq. (8.1) was used whose eigenvalues are given by equation (8.2). The best fit resulted in a potential with $D = (4.41 \pm 0.09)$ meV and $\sigma = (6.3 \pm 0.3)$ Å. This well depth is in the expected range of 4-10 meV[39] and is in good agreement with values estimated in previous studies by our group[60,76]. It must be mentioned, that the positions of the bound state features are not given explicitly through this zeroth order approximation. Nevertheless, the influence of other channels is much smaller and the bare 9-3 potential and its eigenvalues have proven to be good estimations[8].

In figure 8.3 the obtained potential (solid black line) and its corresponding eigenvalues [dashed (blue) lines] are shown, and they agree very well with the measured values [lighter solid (red) lines]. Both experimentally and theoretically determined eigenvalues are listed in table 8.1, which also points out the excellent agreement. Although only 5 bound-state energies were observed in HAS measurements, the obtained potential has an eigenvalue spectrum of 14 bound states. The energies of the additional states $E_{i=5...13}$ are in the region between -0.48 meV and -0.001 meV. Because of these closely spaced levels, a distinct assignment of features in the angular HAS scans (figure 8.2) would require a much higher resolution of the measured data. Nevertheless, in figure 8.2(b) the structures at $\Theta_i = 41°$ and $\Theta_i = 53°$ may arise from resonances with the bound-state energies E_5 to E_{13}.

Compared to the well depth of 8.3 meV for the He-Bi(111) interaction potential[8], the value found for He-Sb(111) is much smaller. This is most likely caused by the higher polarizability of Bi, which causes stronger London dispersion (van der Waals) forces. In contrast to the SAR features in HAS measurements on Bi(111), the observed peaks for He-Sb(111) have both a higher absolute intensity and a much better signal-to-noise ratio. Although the measurement times were longer with HAS from Sb(111), the high intensities were far beyond expectation and should be the subject of an inelastic CC analysis.

8.4.2 Close-Coupling Calculations

In a previous study, the electronic surface corrugation of Sb(111) was determined from HAS by using the approximative GR method[60]. This approach is based on the hard corrugated wall (HCW) model, which neglects the actual shape and especially the attractive part of the atom-surface potential. For a thorough characterization of the Sb(111) surface and the He-Sb(111) interaction potential, an analysis beyond this method is required. Therefore, exact CC calculations, which are based on the determined interaction potential, were performed.

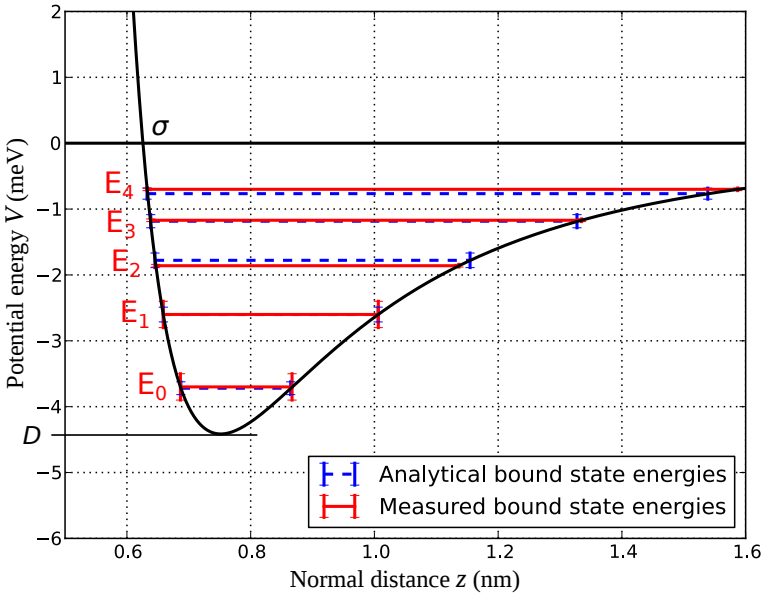

Figure 8.3: Best fit 9-3 potential (8.1) for the He-Sb(111) atom-surface interaction with $D = 4.41$ meV and $\sigma = 0.63$ nm. Lighter solid (red) lines correspond to the experimentally determined bound state energies; dashed (blue) lines indicate the analytical bound state values calculated with eq. (8.2). Uncertainties are shown as vertical bars at the intersections with the potential.

Kinematic Analysis

For numerical convergence in terms of channels, a kinematic analysis must be carried out first. The perpendicular component of the final energy was calculated for different channels. This energy $E_{\mathrm{f},z}$ is a function of the incident energy E_{i}, the azimuthal angle and the incident angle Θ_{i}. The latter is depicted in figure 8.4 for both high symmetry directions and $E_{\mathrm{i}} = 15.3$ meV. If $E_{\mathrm{f},z}$ is positive, the corresponding channel is open, otherwise it is closed. It is obvious that the specular (0,0) channel (solid black line) is always open. The figure also shows channels with a (1,0)-radius (green lines), a (1,1)-radius (blue lines) and a (2,0)-radius (red lines). To preserve the clarity of the illustration, further channels are not shown. For the sixfold geometry of the topmost Sb(111) layer, there are always 6 channels at a certain radius. As shown in figure 8.1, they are partly degenerate. Further degeneracies appear due to crossing of different channels. Both degeneracies are broken by the coupling coefficients of our CC calculations. Furthermore, the zero order positions of SAR are given with the interceptions of the channels with the bound-state energies (dashed horizontal lines). The vertical lines indicate the positions of the Bragg peaks for the fixed-angle geometry of our apparatus. This particular geometry causes moving thresholds (see section 8.2.3); i.e., a certain channel can cross the positions of the Bragg-peaks at different energies. Usually in the CC calculations all open channels,

Table 8.2: Fitted potential parameters (well depth D, stiffness parameter χ, and inflection point z_p) for the Morse- as well as the Hybrid (Morse/9-3) He-Sb(111) interaction potential.

Type	D (meV)	χ (Å^{-1})	z_p (Å)
CMP	4.196	0.380	–
HMP	4.252	0.395	3.0

as well as closed channels with an energy close to zero have to be included. However, for numerical convergence often more channels are taken into account, although at the cost of longer computational times.

Potentials

For further calculations, the potential V_0 and the couplings $V_{\mathbf{G}'-\mathbf{G}}$ have to be specified in the coupled equations (8.15). They should represent the atom-surface interaction as precisely as possible while keeping the set of equations solvable. Usually a CMP, (8.3), is used for CC calculations, because the coupling terms, (8.6), have been derived analytically for this potential type. Since the long-range part of the HMP, (8.10), is similar to the more realistic 9-3 potential, the analysis of the HAS measurement was done with both the CMP and the HMP. For both types the same coupling terms, which are given by equation (8.6), were used. The parameters of these potentials were obtained in the same way as for the 9-3 potential (see section 8.4.1) and are listed in table 8.2. The corresponding bound-state energies are listed in table 8.3. As an estimation for the uncertainty, the parameter σ_E given in table 8.3 is defined as

$$\sigma_\mathrm{E} \;=\; \frac{1}{N}\sqrt{\sum_{i=1}^{N}\left|\epsilon_i^{\mathrm{exp}}-\epsilon_i^{\mathrm{pot}}\right|^2}, \tag{8.17}$$

with N the number of bound-states included. For both potentials the calculated energies of the fitted potentials are in very good agreement with the experimentally obtained values. However, the values for E_3 and E_4 are better represented by the HMP than by the CMP due to the superior asymptotic behavior.

The electronic surface corrugation

After these initial considerations, CC calculations were performed to obtain the effective electronic surface corrugation. The corrugation function $\xi(\mathbf{R})$ that we used for our model

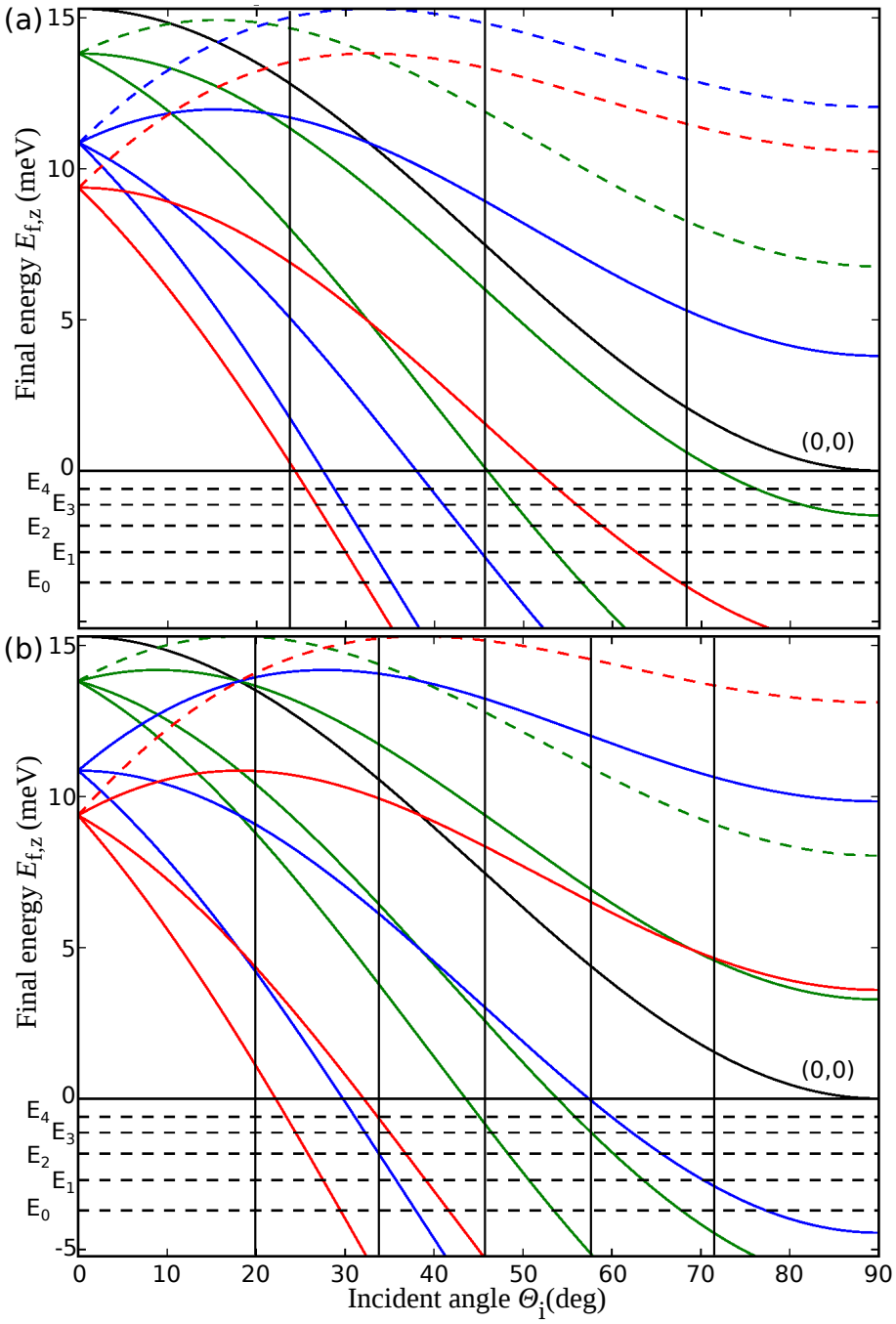

Figure 8.4: (a): Perpendicular kinetic energy $E_{f,z}$ as a function of the incident angle Θ_i with the Sb(111) crystal oriented in $\overline{\Gamma K}$ direction and an incident energy $E_i = 15.3$ meV for He atoms. The black curve indicates the specular (0,0) channel. Green, blue and red lines depict channels with (1,0)-, (1,1)- and (2,0)-radii, respectively. The Bragg peak positions for the experimental setup used are represented by the vertical lines.
(b): Same as (a), for the $\overline{\Gamma M}$ direction.

Table 8.3: Bound-state energies experimentally determined from HAS measurements and calculated analytically for the CMP and numerically for the HMP.

Bound State	Experiment Energy (meV)	CMP eq. (8.9) Energy (meV)	HMP Energy (meV)
E_0	-3.7	-3.7	-3.7
E_1	-2.6	-2.7	-2.7
E_2	-1.86	-1.82	-1.82
E_3	-1.17	-1.13	-1.17
E_4	-0.70	-0.60	-0.72
σ_{E}	$-$	0.03	0.02

potential (8.3) is given by

$$\xi(x,y) = \xi_0 \cdot \left(\cos\left[\tfrac{2\pi}{a}\left(x - \tfrac{y}{\sqrt{3}}\right)\right] + \cos\left[\tfrac{2\pi}{a}\left(x + \tfrac{y}{\sqrt{3}}\right)\right]\right) + \xi_0 \cdot \cos\left[\tfrac{2\pi}{a} \cdot \tfrac{2y}{\sqrt{3}}\right]. \tag{8.18}$$

It takes into account the sixfold-symmetry of the topmost layer of the surface, which is the only important layer when considering the energies of the He atoms used in our experiments[60]. x and y are rectangular coordinates and ξ_0 denotes the amplitude of the corrugation to be optimized. Therewith, the amplitudes of the outgoing waves were calculated by solving the CC equations using a Numerov algorithm with a Fox-Goodwin integrator. The square moduli of these resulting amplitudes are proportional to the diffraction intensities (probabilities) I_G^{calc} [48]. The geometry of our sample determines the Fourier coefficients $v_{\mathbf{G}=h\mathbf{a}^*+k\mathbf{b}^*}$ of the coupling terms (8.6) to be[167]

$$v_{h,k} = \frac{\sqrt{3}}{2}\frac{a^2}{\pi}\frac{1}{2}\sum_{i=-\infty}^{\infty} I_i(\alpha)[I_{i+h}(\alpha)I_{i-k}(\alpha) + I_{i-h}(\alpha)I_{i+k}(\alpha)], \tag{8.19}$$

with $I_i(\alpha)$ the modified Bessel functions and $\alpha = 2\chi\xi_0$.

To account for the influence of surface vibrations at non-zero surface temperature on the intensity of the diffraction peaks, the Debye-Waller factor was included in our CC results. Its application in the analysis of HAS results has been discussed elsewhere[60]. The Debye-temperature used, 155 K, was measured with HAS recently[76].

To find the best fit between measured (P_G^{exp}) and calculated diffraction probabilities a measure of deviation R,

$$R = \frac{1}{N}\sqrt{\sum_G (P_G^{\mathrm{exp}} - I_G^{\mathrm{calc}})^2}, \tag{8.20}$$

Table 8.4: Results of the CC calculations for the CMP and HMP at different incident energies E_i. Peak-to-peak values are given for the obtained corrugation function, eq. (8.18), as well as the effective corrugation function, (8.21), relative to the lattice constant a.

Type	E_i (meV)	ξ_{pp} (Å)	R (%)	ξ_{pp}/a (%)	$\xi_{E_i,pp}/a$ (%)
CMP	15.3	0.59	6.1	13.7	9.5
CMP	21.9	0.63	7.2	14.6	9.8
HMP	15.3	0.76	4.5	17.7	12.4
HMP	21.9	0.74	3.8	17.1	11.5

was calculated, where N is the number of experimentally observed diffraction peaks[39]. This approach was used for both incident energies E_i, resulting in the best fit coefficients ξ_0 listed in table 8.4. The peak-to-peak corrugation ξ_{pp} was calculated for a comparison with the values obtained with the GR method in a previous analysis[60] and is also given as a percentage of the lattice constant. Especially in the case of the HMP, where the diffraction possibilities found are reproduced very well, the corrugation determined within this study is significantly higher. Since the shape of the obtained potential was included in the calculations, in particular, the results for the HMP are more accurate than the results obtained with the GR-method, which uses a HCW model. Beside the fact that the CC calculations are quantum-mechanically correct if convergent, they are preferable to HCW models when dealing with such high peak-to-peak corrugations as observed in this investigation.

In figure 8.5(a) the results of angular HAS scans are shown along the surface directions $\overline{\Gamma M}$ and $\overline{\Gamma K}$ at an incident beam energy of $E_i = 15.3$ meV (black line). For comparison with CC results, the areas of the experimentally measured Bragg peaks were determined (black crosses). The peak area was used instead of the intensity to account for effects such as the different widths of the Bragg peaks due to the nonzero energy width as well as the angular spread of the incident He beam. While the red squares in figure 8.5 indicate the best fitting CC results that were obtained with the CMP, the resulting probabilities of CC calculations with the HMP are represented by (green) circles. Figure 8.5(b) depicts results obtained experimentally and theoretically at $E_i = 21.9$ meV. As shown in the figures and the R-values in table 8.4, the best fit was obtained with the HMP in CC calculations. Although there are deviations between theoretical and experimental findings, the corrugation found gives a good prediction of the measured intensities and their agreement is much better than for the CMP. Particularly, the calculations for the CMP failed to reproduce the diffraction probabilities along $\overline{\Gamma K}$ as well as the second order probabilities along $\overline{\Gamma M}$. When the fit was adjusted to get a better agreement at these positions, the fit for the first order diffraction peaks in $\overline{\Gamma M}$ got much worse. Hence, these

values were taken for the best fit CMP CC results. The lower intensities obtained from the measurements may be caused by the experimental setup: The measured intensities decrease with increasing angle between the specular peak and the position of measurement, which can be seen in the background signal of figure 8.2. The theoretical results in figure 8.5(a) show a remarkable asymmetry for both first and second order diffraction probabilities. While this is clearly noticeable in calculations with $E_\mathrm{i} = 15.3$ meV, the results for a higher incident energy (see figure 8.5(b)) are almost symmetric. Likely, this is caused by the relative arrangement of the diffraction channels at a particular position of an elastic diffraction peak (see figure 8.4). No clear indication of such an arrangement and hence no final explanation were found, but it should be noted that small deviations between real and determined bound-state energies may have a major influence on the occurence of such conditions during CC calculations. In order to achieve a precision of two significant digits in the results of the CC calculations, a total number of 75 channels were included.

At the position of the classical turning points of He atoms $V(\mathbf{R}, z) = E_i \cos^2 \Theta_\mathrm{i}$ holds, which defines implicitly $[z = \xi_{E_i}(\mathbf{R})]$ the *effective corrugation function* $\xi_{E_\mathrm{i}}(\mathbf{R})$[140]. Due to the fixed-angle geometry of the apparatus, measurements at different incident angles Θ_i are indispensable. However, for the following determination of the effective corrugation, perpendicular incidence $\Theta_\mathrm{i} = 0°$ was assumed, which yields

$$\xi_{E_\mathrm{i}}(\mathbf{R}) = \frac{1}{\chi} \ln \left[-\frac{D}{E_\mathrm{i}} + \sqrt{\frac{D^2}{E_\mathrm{i}^2} + \frac{D}{E_\mathrm{i}} \left(1 + \sum_{\mathbf{G} \neq 0} \frac{\nu_\mathbf{G}}{\nu_0} e^{i\mathbf{G}\cdot\mathbf{R}} \right)} \right] . \tag{8.21}$$

Note that ξ_{E_i} depends on the incident energy E_i of the He atoms and on the well depth of the laterally averaged atom-surface interaction potential D. ξ_{E_i} is used to obtain equipotential surfaces and is usually presented as a result of CC calculations. The obtained results are listed in table 8.4. Furthermore, it acts as an effective illustration of the shape of the electronic corrugation, hence it is depicted in figure 8.6.

8.4.3 Resonance Effects in the Specular Intensity

When the intensity of the specular peak is measured as a function of the incident momentum (drift spectrum), several features of different origins appear. First, the intensity of the incident He beam depends on the nozzle temperature T_N via $1/\sqrt{T_\mathrm{N}}$. Second, due to interference effects of waves scattered from different terraces, an oscillation of the measured signal is detectable[39]. Using the positions as well as the intensities of the major peaks and dips, the terrace height and distribution on the Sb(111) surface were estimated in a previous study[60]. Besides these main features, finer peaks and dips arise because of SAR conditions that are moving "through" the angular position of the measurement. In principle this type of experiment is possible with an arbitrary incident angle. However, the position of the specular peak was chosen to obtain the best signal-to-noise ratio.

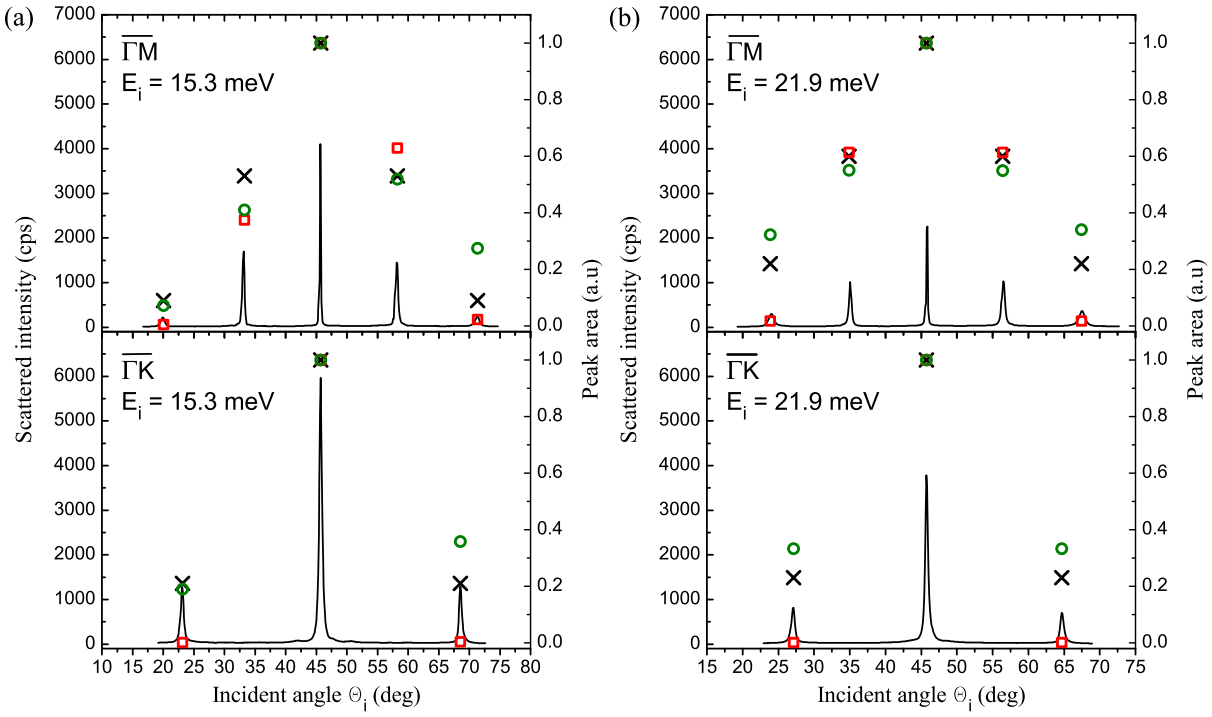

Figure 8.5: (a): Angular distributions of HAS intensity along the $\overline{\Gamma M}$ and $\overline{\Gamma K}$ surface directions at a beam energy of 15.3 meV. The peak areas (black crosses), determined from measurements (black line) are in good agreement with the best-fit results from CC calculations including the HMP [(green) circles]. Best-fit diffraction probabilities calculated with the CMP [(red) squares] show a larger deviation from the measured values. Especially when modeling the diffraction in $\overline{\Gamma K}$, the HMP is superior to the CMP.
(b): Same as (a) with a beam energy of 21.9 meV. Again, the CC results for the HMP are, in contrast to the CMP, in very good agreement with the measured values.

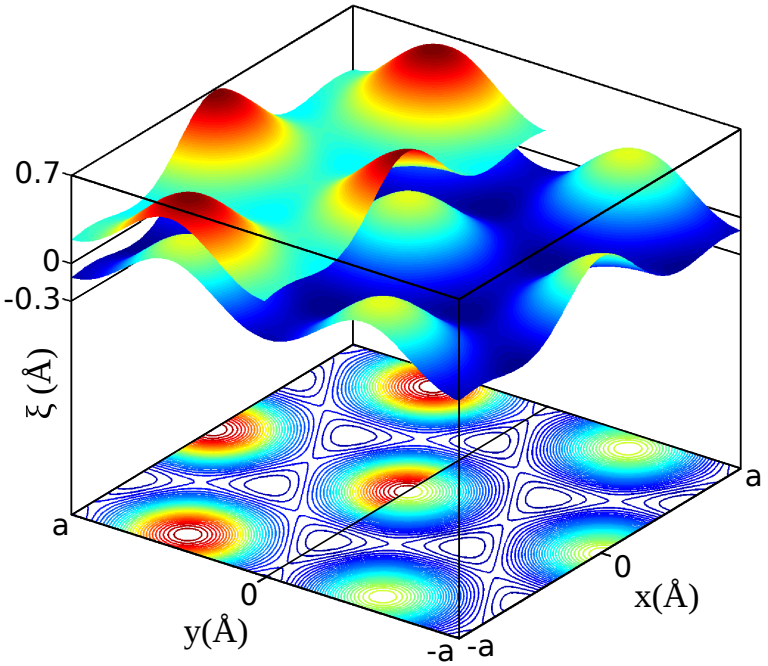

Figure 8.6: Plot of the effective corrugation for the Sb(111) surface as obtained by HAS measurements and CC calculations with the HMP for perpendicular incidence $\Theta_i = 0°$. The upper part shows the result for an incident energy E_i=15.3 meV, whereas the lower part shows the effective corrugation for E_i=21.9 meV. In the latter case He atoms experience turning points closer to the surface.

In figure 8.7(a) the measured specular intensity (dashed black line) is shown as a function of the energy of the incident helium beam. The nozzle temperature was varied between 53 and 150 K to achieve energies of the He atoms between 11 and 32 meV. Elastic CC calculations were used to explain the features observed in this measurement. The necessary corrugations for these calculations were obtained with a linear inter- and extrapolation of the best fitting corrugation parameters (HMP). The obtained result [dashed black line in figure 8.7(b)] was convoluted with a Gaussian peak to take into account the energy broadening of the incident He beam [solid (red) line]. In addition, the nozzle temperature-dependency of the He beam intensity and the contribution from the different terraces[60] were included and the Debye-Waller (DW) attenuation was taken into account by using a surface Debye temperature of 155 K, which was determined in a previous study[76].

In figure 8.7(a) the theoretically predicted signal is shown as the solid (green) line. It is in good agreement with the experimental data, although there is a shift of the peak near E_i=12 meV. Most of the features found in the measurement could be assigned to peaks in the theoretically predicted signal, which proves the quality of the model used (the electronic surface corrugation found).

8.4.4 Kinematic Focusing

The angular scan along $\overline{\Gamma\mathrm{K}}$ (figure 8.2(a)) shows two additional features at $\Theta_\mathrm{i} = 26.5°$ and $\Theta_\mathrm{i} = 42.0°$, which can be explained by the occurrence of kinematic focusing (KF)[26,74]. At an angular position, where the scan curve of the HAS experiment is tangent to the surface-phonon dispersion curve, an enhancement of the detected He intensity is observable. For the experimental setup used, a certain scan curve is given by[6,74]

$$\frac{\Delta E}{E_\mathrm{i}} = \frac{\sin^2\Theta_\mathrm{i}}{\sin^2(\Theta_\mathrm{SD}-\Theta_\mathrm{i})}\left(1+\frac{\Delta K}{K_\mathrm{i}}\right)^2 - 1, \tag{8.22}$$

where ΔE is the gained (lost) energy due to phonon annihilation (creation), and ΔK the corresponding wave vector of the phonon. Although the surface-phonon bands have not been measured to date, Campi et al.[10] used density functional perturbation theory (DFPT) to model the surface dynamics of Sb(111). Figure 8.8 shows the results for a slab with 24-layers as a longitudinally polarized mode along the $\overline{\Gamma\mathrm{K}}$ direction. Furthermore, selected scan curves for our measuring geometry at incident angles around the KF positions are plotted as solid (blue) lines (phonon creation). It is clearly shown that the scan curves in the vicinity of these angles are tangent to the surface phonon modes, which is a prerequisite for KF appearance. The peaks found prove that KF is a reliable tool for investigation of the exact position of theoretically predicted surface phonon modes.

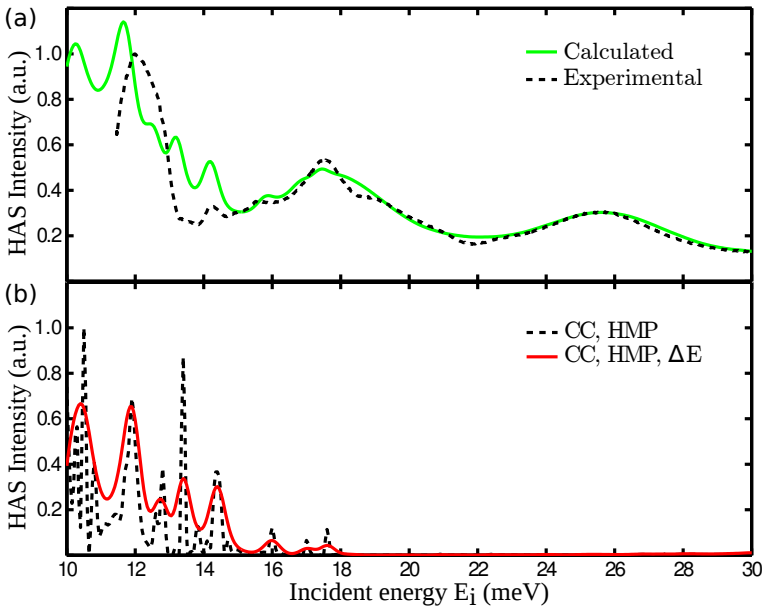

Figure 8.7: (a): Drift spectrum of the specular (0,0) peak with the sample orientated in the $\overline{\Gamma M}$-direction. The measured intensity [dashed (black) line] is plotted versus the incident energy E_i of the He beam. The simulated intensity [solid (green) line] is in good agreement with the experiment.
(b): Results from CC calculations [dashed (black) line] were convoluted with a Gaussian peak to account for the energy spread ΔE of the He beam. The signal obtained [solid (red) line] was used as the SAR contribution for the calculated intensity in (a).

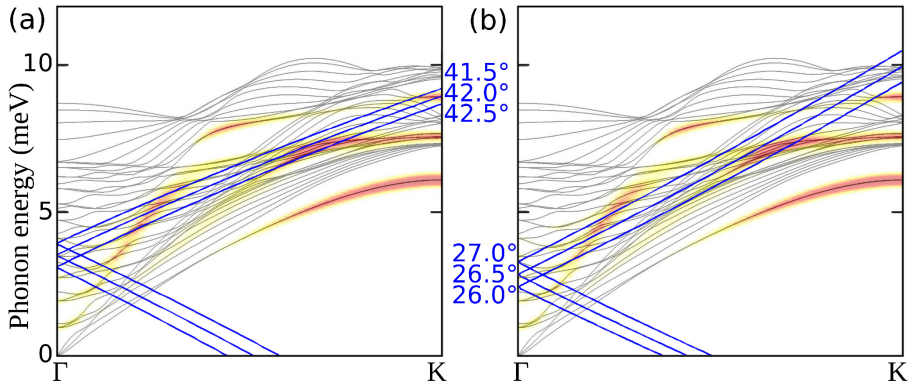

Figure 8.8: (a): Scan curves [solid (blue) lines] proving the KF origin of the additional peak at $\Theta_i = 42°$ in figure 8.2(a). Black lines show the dispersion curves for a 24-layer slab of Sb(111) calculated with DFPT as published by Campi et al.[10]. Surface-localized modes and resonances for longitudinal polarization are indicated by shaded regions. For an incident angle of about 42.5°, the scan curve for phonon creation is tangent to the surface mode with an energy between 7 and 8 meV.
(b): Same as (a) with scan curves for incident angles of about $\Theta_i = 26.5°$, which are tangent to the same surface phonon mode.

8.5 Conclusions

The He-Sb(111) interaction potential was determined by a thorough analysis of elastic HAS measurements. Clearly observable SAR features between the positions of the Bragg peaks were used to estimate five bound-state energies in the attractive well (see table 8.1). They were best fit with the eigenvalues of a 9-3 interaction potential with a well depth of 4.4 ± 0.1 meV. Compared to HAS on Bi(111)[8], the He-Sb(111) potential is shallower, which is the result of the lower polarizability of Sb. Furthermore, the exact CC method was applied to determine the electronic surface corrugation. Therewith, the bound-state energies were used to model potentials (CMP, HMP) suitable for CC calculations. The CC results for the CMP showed deviations from the measured intensities, most likely due to the weaker long-range part of the CMP compared to the HMP. CC results for the HMP are in good agreement with the experimental data. For the best fitting model, HMP, a peak-to-peak corrugation of approximately 17% was obtained, which is higher than the value obtained with the less accurate HCW models[60]. The effective corrugation was found to have a peak-to-peak value of approximately 12%. Furthermore, CC calculations were used to model the intensity modulation of the specular peak as a function of the incident beam energy. The theoretical findings are in very good agreement with the measurements, which is further proof of the good quality of the He-Sb(111) interaction potential obtained. Two additional peaks found in

the elastic measurements were attributed to KF effects, which were used as a coarse consistency check for the DFPT calculations of the Sb(111) surface phonon modes[10]. The He-Sb(111) interaction potential and the electronic surface corrugation obtained represent a further step towards a complete understanding of the surface properties of the semimetal antimony and its role as a building block in topological insulators. The bound-state energies determined will help in the analysis of future inelastic HAS measurements. Therewith, the experimentally determined surface phonon dispersion will be obtained and a comparison with DFPT results[10] will help to improve theoretical models of the surface dynamics. Based on our results for HAS on Bi(111)[6–8], mode-dependent electron-phonon coupling strengths will be investigated, especially if resonance-enhanced subsurface phonon modes can be detected.

In this work, we have applied the exact CC method within the framework of elastic channels. However, even in the calculation of elastic intensities and elastic selective adsorption resonances, couplings to inelastic channels have to be taken into account. We have used a simplified approach by including inelastic effects via a global attenuation factor: the DW factor. We think that it would be desirable to include inelastic channels in the CC framework instead of using the DW factor in order to be completely consistent. Further theoretical developments towards this goal are under way and should show whether our current approximations are sufficient.

9 Summary

This thesis describes helium atom scattering (HAS) experiments that have been performed with the aim of investigating the semimetal surfaces Bi(111) and Sb(111). A characterisation of the used apparatus H.Å.N.S.[3,75] and the main results of HAS from Bi(111)[4–8] had been already summarised by Anton Tamtögl[1]. Hence, the included analysis of HAS from Bi(111) acts as a supplement and concentrates on surface step height and terrace distribution, the electronic corrugation and the surface Debye temperature. Together with these results from Bi(111), novel findings on the structure and dynamics of Sb(111) are summarised below. Furthermore, the most important results found during this study are compared in table 9.1.

9.1 Bi(111)

Elastic HAS measurements on Bi(111) revealed diffraction peaks up to third order. The lattice constant obtained from the positions of the peaks is in very good agreement with the data obtained by Mönig et al.[103]. Modulations of the HAS intensity at the position of the specular peak with different incident energies of the He beam were used to find a step height of (3.9 ± 0.1) Å which is in excellent agreement with other experiments[80,103] and DFPT calculations[6]. Although a very simple model was used, it could be shown that the clean Bi(111) surface is quite flat.

An electronic corrugation of approximately 10% was found with using the eikonal approximation and the GR method to analyse the relative heights of the diffraction peaks. By using the Beeby correction, a well depth of 8 meV of the attractive part of the He-Bi(111) interaction potential was found, which is in very good agreement with recent investigation of selective adsorption resonances (8.3 ± 0.8) meV[8]. The rather large corrugation may be caused by electronic states, e.g. electron pockets at the Fermi level[105].

To account for effects arising from influences of phonons, the HAS measurements were performed with the crystal surface at different temperatures between 118 K and 408 K. The sample showed a typical Debye-Waller behaviour in the thermal attenuation of the HAS intensity. A surface Debye temperature of (84 ± 8) K was obtained from measurements of the specular peak. Measurements at an angular position of a first order peak yielded a surface Debye temperature of (75 ± 8) K. The obtained values remain

constant over the whole temperature range, which is in contrast to LEED measurements of Bi nanofilms.

The results of inelastic HAS together with a thorough interpretation of the surface phonon dispersion of Bi(111) can be found in[1].

9.2 Sb(111)

Elastic HAS measurements on Sb(111) revealed diffraction peaks up to third order. The positions of these peaks are in perfect agreement with already known structural data obtained by Bengió et al.[95]. Modulations of the HAS intensity at the position of the specular peak with different incident energies of the He beam were used to find a step height of 3.81 Å which is in excellent agreement with recent calculations[10]. Although a very simple model was used, it was shown that the clean Sb(111) surface is quite flat.

Beam energies between 15.3 and 21.9 meV were used to estimate the surface corrugation. While the result obtained from hard corrugated wall models (GR method) was in the region of 12-13% of the lattice constant, close-coupling (CC) calculations yielded a higher value of approximately 17%. The applied CC method considered only elastic channels, nevertheless it was based on a more realistic shape of the He-Sb(111) interaction potential. Hence, the higher value for the electronic surface corrugation represents a more reliable result. Also in the case of Sb(111) this, compared to other surfaces with metallic character, rather large corrugation may be caused by electronic states, e.g. electron pockets at the Fermi level[97].

To investigate the surface dynamics of Sb(111), HAS measurements were performed with the crystal surfaces at different temperatures between 98 K and 447 K. The sample showed a typical Debye-Waller behaviour in the thermal attenuation of the HAS intensity. A surface Debye temperature of (155 ± 3) K was obtained from measurements of the specular peak. Measurements at an angular position of a first order peak yielded a surface Debye temperature of (150 ± 6) K.

A careful analysis of selective adsorption resonances revealed a potential well depth of (4.4 ± 0.1) meV of the attractive part of the He-Sb(111) interaction potential. Two additional peaks found in the elastic measurements were attributed to KF effects, which were used as a coarse consistency check for DFPT calculations of the Sb(111) surface phonon modes[10].

Table 9.1: Comparison of Bi(111) and Sb(111) properties as determined with HAS.

	Bi(111)	Sb(111)
no. of observed HAS peaks in $\overline{\Gamma M}$, $\overline{\Gamma K}$	3, 1	3, 1
lattice constant a (T=298 K)	4.54 Å	4.31 Å
step height	3.9 Å	3.81 Å
terrace distribution (0^{th}, 1^{st}, 2^{nd} level)	87%, 12%, 1%	84%, 14%, 2%
Debye temperature Θ_D, specular peak	(84 ± 8) K	(155 ± 3) K
Debye temperature Θ_D, 1^{st} order peak	(75 ± 8) K	(150 ± 6) K
He-surface 9-3 potential depth D	(8.3 ± 0.8) meV	(4.4 ± 0.1) meV
no. of observed bound states	3	5
surface corrugation / a, with GR	10%	13%
surface corrugation / a, with CC	-	17%

Danksagung

Zuallererst darf ich mich bei meinem Betreuer, *Prof. Wolfgang E. Ernst*, sehr herzlich bedanken. Sein mir vermitteltes Fachwissen, seine Erfahrungen und auch die von ihm zur Verfügung gestellte Finanzierung bildeten das Fundament für die hier vorliegende Arbeit. Weiters möchte ich besonders die Freiheit und die Flexibilität, die er sowohl in der Forschung, als auch in der Administration gewährt, positiv hervorheben.
Besonderer Dank gilt all jenen, die dazu beigetragen haben, dass ich die Zeit meines Doktoratsstudiums nicht nur als "Arbeit" in Erinnerung behalten werde. Danke, an *Captain Toni*, der das Boot mehr als einmal durch raue See führte. An *Günter*, für faire Outdoor-Abenteuer, ob im Kajak oder in den Bergen. An *Michi*, für Daleks und Popcorn in kalten Zeiten ("Winter is coming!"). An *Stefan* und die *NERDs 08*, für lustige erste, zweite und dritte Halbzeiten. An *Mani*, der uns durch sein intensives Studium fremder Kulturen einige Feldversuche ermöglichte. Und natürlich an *Patrick*, denn was gibt es schöneres, als mit Freunden am selben Projekt zu arbeiten und dabei Erfolge ("Call me, call me by my name...") und Misserfolge ("Ich stehe morgens auf, es ist halb drei...") zu teilen. Insbesondere dann, wenn man sich dabei selbst nicht allzu ernst, die ungezählten Go-Partien und Conference Calls von *Mr. Wang* dafür umso wichtiger nimmt. Ihr alle habt die Zeit meines Studiums bereichert, mich durch schwere Zeiten begleitet und ihr alle habt Anteil am Erfolg dieser Arbeit.
Auch wenn es nicht immer so scheint, gibt es auch ein Leben abseits der Physik. Und weitere Menschen, bei denen ich mich bedanken möchte. Allen voran stehen hier natürlich meine Eltern *Martin und Anna*. Es ist unmöglich, in wenigen Sätzen zu beschreiben, für was und wie sehr ich mich bei euch bedanken will. Nur durch eure Hilfe habe ich es bis hierher geschafft. Ich darf nur hoffen, dass ich meinen eigenen Kindern ähnlich zur Seite stehen und für sie da sein kann, wie ihr das für mich getan habt.
Meinem Bruder *Martin* danke ich vor allem für die leider viel zu seltenen Gespräche, egal ob über (Koch-)Künste, Philosophen oder andere Themen des täglichen Seins. Es ist schön, einen Bruder wie dich zu haben und ich freue mich jedes Mal, wenn wir uns sehen, egal ob in Graz, Thalgau oder sonst irgendwo auf dieser Welt.
Sara, dir danke ich neben deiner Unterstützung, besonders in arbeitsintensiven Zeiten, vor allem auch für das Strahlen in deinen Augen, das mir jeden Tag aufs Neue zeigt, was es heißt, zu lieben und geliebt zu werden.
Zum Abschluss möchte ich mich bei *Gott* bedanken. Erst mit dir macht alles Sinn.
Danke.

10 Bibliography

[1] A. Tamtögl, Ph.D. thesis, Graz University of Technology (2012).

[2] A. Jardine, H. Hedgeland, G. Alexandrowicz, W. Allison, and J. Ellis, Prog. Surf. Sci. **84**, 323 (2009), ISSN 0079-6816, URL http://www.sciencedirect.com/science/article/B6TJF-4X0MP7F-1/2/4b3a9cac32140a526ede2c1e79325b49.

[3] N. Balak, Master's thesis, Graz University of Technology (2009).

[4] A. Tamtögl, M. Mayrhofer-Reinhartshuber, N. Balak, W. E. Ernst, and K. H. Rieder, J. Phys.: Cond. Matt. **22**, 304019 (2010), URL http://stacks.iop.org/0953-8984/22/i=30/a=304019.

[5] M. Mayrhofer-Reinhartshuber, A. Tamtögl, P. Kraus, K. H. Rieder, and W. E. Ernst, J. Phys.: Cond. Matt. **24**, 104008 (2012), ISSN 0953-8984, URL http://stacks.iop.org/0953-8984/24/i=10/a=104008.

[6] A. Tamtögl, P. Kraus, M. Mayrhofer-Reinhartshuber, D. Campi, M. Bernasconi, G. Benedek, and W. E. Ernst, Phys. Rev. B **87**, 035410 (2013), URL http://link.aps.org/doi/10.1103/PhysRevB.87.035410.

[7] A. Tamtögl, P. Kraus, M. Mayrhofer-Reinhartshuber, D. Campi, M. Bernasconi, G. Benedek, and W. E. Ernst, Phys. Rev. B **87**, 159906(E) (2013), URL http://link.aps.org/doi/10.1103/PhysRevB.87.159906.

[8] P. Kraus, A. Tamtögl, M. Mayrhofer-Reinhartshuber, G. Benedek, and W. E. Ernst, Phys. Rev. B **87**, 245433 (2013), URL http://link.aps.org/doi/10.1103/PhysRevB.87.245433.

[9] H. Zhang, C.-X. Liu, X.-L. Qi, X. Dai, Z. Fang, and S.-C. Zhang, Nature Physics **5**, 438 (2009), URL http://www.nature.com/nphys/journal/v5/n6/abs/nphys1270.html.

[10] D. Campi, M. Bernasconi, and G. Benedek, Phys. Rev. B **86**, 075446 (2012), URL http://link.aps.org/doi/10.1103/PhysRevB.86.075446.

[11] E. Hulpke, *Helium Atom Scattering from Surfaces* (Springer, 1992).

[12] R. B. Doak, *Atomic and Molecular Beam Methods* (Oxford University Press, 1983), vol. 2, chap. Single-Phonon Inelastic Helium Scattering, pp. 385–441.

[13] J. P. Toennies, *Surface Phonons* (Springer, 1991), chap. Experimental Determination of Surface Phonons by Helium Atom and Electron Energy Loss Spectroscopy, pp. 111–166.

[14] S. A. Safron, *Advances in Chemical Physics - Surface Properties* (John Wiley & Sons, 1996), vol. 95 of *Advances in Chemical Physics*, chap. High-Resolution Helium Atom Scattering as a Probe of Surface Vibrations, p. 129.

[15] H. Pauly, *Atom, Molecule, and Cluster Beams I* (Springer, 2000).

[16] T. Reisinger, G. Bracco, S. Rehbein, G. Schmahl, W. E. Ernst, and B. Holst, The Journal of Physical Chemistry A **111**, 12620 (2007), pMID: 17985855, `http://pubs.acs.org/doi/pdf/10.1021/jp076102u`, URL `http://pubs.acs.org/doi/abs/10.1021/jp076102u`.

[17] H. Pauly, *Atom, Molecule, and Cluster Beams II* (Spri, 2000).

[18] C. Kittel, *Introduction to Solid State Physics* (John Wiley & Sons Inc, 2005).

[19] K. Oura, V. G. Lifshits, A. A. Saranin, A. V. Zotov, and M. Katayama, *Surface Science: An Introduction* (Springer, 2003).

[20] W. Unertl, in *Physical Structure*, edited by W. Unertl (North-Holland, 1996), vol. 1 of *Handbook of Surface Science*, pp. 3 – 49, URL `http://www.sciencedirect.com/science/article/pii/S1573433196800060`.

[21] H. Lüth, *Solid Surfaces, Interfaces and Thin Films* (Springer, 2001), 4th ed.

[22] K. Kern and G. Comsa, *Helium-Scattering Studies of the Dynamics and Phase Transitions of Surfaces* (John Wiley & Sons, Inc., 2007), pp. 211–280, ISBN 9780470141250, URL `http://dx.doi.org/10.1002/9780470141250.ch5`.

[23] F. W. de Wette, *Surface Phonons*, vol. 21 of *Springer Series in Surface Sciences* (Springer, 1991).

[24] B. R. Williams, The Journal of Chemical Physics **55**, 3220 (1971), URL `http://scitation.aip.org/content/aip/journal/jcp/55/7/10.1063/1.1676571`.

[25] B. F. Mason and B. R. Williams, The Journal of Chemical Physics **61**, 2765 (1974), URL `http://scitation.aip.org/content/aip/journal/jcp/61/7/10.1063/1.1682411`.

[26] G. Benedek, G. Brusdeylins, J. P. Toennies, and R. B. Doak, Phys. Rev. B **27**, 2488 (1983), URL http://link.aps.org/doi/10.1103/PhysRevB.27.2488.

[27] J. R. Manson, Phys. Rev. B **43**, 6924 (1991), URL http://link.aps.org/abstract/PRB/v43/p6924.

[28] M. DeKieviet, D. Dubbers, C. Schmidt, D. Scholz, and U. Spinola, Phys. Rev. Lett. **75**, 1919 (1995), URL http://link.aps.org/doi/10.1103/PhysRevLett.75.1919.

[29] A. P. Jardine, J. Ellis, and W. Allison, Journal of Physics: Condensed Matter **14**, 6173 (2002), URL http://stacks.iop.org/0953-8984/14/i=24/a=315.

[30] G. Brusdeylins, R. B. Doak, and J. P. Toennies, Phys. Rev. B **27**, 3662 (1983), URL http://link.aps.org/doi/10.1103/PhysRevB.27.3662.

[31] H. Hoinkes, Rev. Mod. Phys. **52**, 933 (1980), URL http://link.aps.org/doi/10.1103/RevModPhys.52.933.

[32] M. Mayrhofer-Reinhartshuber, P. Kraus, A. Tamtögl, S. Miret-Artés, and W. E. Ernst, Phys. Rev. B **88**, 205425 (2013), URL http://link.aps.org/doi/10.1103/PhysRevB.88.205425.

[33] G. P. Brivio and M. I. Trioni, Rev. Mod. Phys. **71**, 231 (1999), URL http://link.aps.org/doi/10.1103/RevModPhys.71.231.

[34] M. I. Trioni, G. Fratesi, S. Achilli, and G. P. Brivio, Journal of Physics: Condensed Matter **21**, 264003 (2009), URL http://stacks.iop.org/0953-8984/21/i=26/a=264003.

[35] T. Engel and K. Rieder, in *Structural Studies of Surfaces* (Springer Berlin Heidelberg, 1982), vol. 91 of *Springer Tracts in Modern Physics*, pp. 55–180, ISBN 978-3-540-10964-8, URL http://dx.doi.org/10.1007/BFb0041342.

[36] M. W. Cole and T. Tsong, Surface Science **69**, 325 (1977), ISSN 0039-6028, URL http://www.sciencedirect.com/science/article/pii/0039602877901777.

[37] R. Smoluchowski, Phys. Rev. **60**, 661 (1941), URL http://link.aps.org/doi/10.1103/PhysRev.60.661.

[38] G. Boato, *Atomic and Molecular Beam Methods* (Oxford University Press, 1983), chap. Elastic Scattering of Atoms, pp. 340–365.

[39] D. Farias and K.-H. Rieder, Reports on Progress in Physics **61**, 1575 (1998), URL http://stacks.iop.org/0034-4885/61/i=12/a=001.

[40] E. Conrad, in *Physical Structure*, edited by W. Unertl (North-Holland, 1996), vol. 1 of *Handbook of Surface Science*, pp. 271 – 360, URL http://www.sciencedirect.com/science/article/pii/S1573433196800126.

[41] J. W. B. R. Strutt, Proceedings of the Royal Society of London **A 79**, 388 (1907).

[42] J. Wauer and T. Rother, Optics Communications **282**, 339 (2009), ISSN 0030-4018, URL http://www.sciencedirect.com/science/article/pii/S0030401808010122.

[43] N. García, The Journal of Chemical Physics **67**, 897 (1977), URL http://link.aip.org/link/?JCP/67/897/1.

[44] N. García and N. Cabrera, Phys. Rev. B **18**, 576 (1978), URL http://link.aps.org/doi/10.1103/PhysRevB.18.576.

[45] E. Stoll, M. Baumberger, and N. Garcia, The Journal of Chemical Physics **81**, 1496 (1984), URL http://link.aip.org/link/?JCP/81/1496/1.

[46] J. L. Beeby, J. Phys. C: Solid State Phys. **4**, L359 (1971).

[47] J. S. Becker, R. D. Brown, E. Johansson, N. S. Lewis, and S. J. Sibener, The Journal of Chemical Physics **133**, 104705 (pages 8) (2010), URL http://link.aip.org/link/?JCP/133/104705/1.

[48] A. Sanz and S. Miret-Artés, Phys. Rep. **451**, 37 (2007), ISSN 0370-1573, URL http://www.sciencedirect.com/science/article/pii/S0370157307003250.

[49] G. Wolken, The Journal of Chemical Physics **58**, 3047 (1973), URL http://scitation.aip.org/content/aip/journal/jcp/58/7/10.1063/1.1679617.

[50] G. Wolken, The Journal of Chemical Physics **59**, 1159 (1973), URL http://scitation.aip.org/content/aip/journal/jcp/59/3/10.1063/1.1680162.

[51] A. Liebsch, J. Harris, B. Salanon, and J. Lapujoulade, Surface Science **123**, 338 (1982), ISSN 0039-6028, URL http://www.sciencedirect.com/science/article/pii/0039602882903326.

[52] R. B. Laughlin, Phys. Rev. B **25**, 2222 (1982), URL http://link.aps.org/doi/10.1103/PhysRevB.25.2222.

[53] G. Drolshagen, A. Kaufhold, and J. P. Toennies, The Journal of Chemical Physics **83**, 827 (1985), URL http://scitation.aip.org/content/aip/journal/jcp/83/2/10.1063/1.449497.

[54] J. R. Manson, E-mail correspondence (2011).

[55] E. H. Conrad, D. S. Kaufman, L. R. Allen, R. M. Aten, and T. Engel, J. Chem. Phys. **83**, 5286 (1985), URL http://link.aip.org/link/?JCP/83/5286/1.

[56] W. Steurer, A. Apfolter, M. Koch, W. Ernst, and B. Holst, Surface Science **602**, 1080 (2008), ISSN 0039-6028, URL http://www.sciencedirect.com/science/article/pii/S0039602808000101.

[57] C. Tölkes, P. Zeppenfeld, M. A. Krzyzowski, R. David, and G. Comsa, Phys. Rev. B **55**, 13932 (1997), URL http://link.aps.org/doi/10.1103/PhysRevB.55.13932.

[58] V. Bortolani, V. Celli, A. Franchini, J. Idiodi, G. Santoro, K. Kern, B. Poelsema, and G. Comsa, Surface Science **208**, 1 (1989), ISSN 0039-6028, URL http://www.sciencedirect.com/science/article/pii/0039602889900332.

[59] F. M. Pan, C. Pflitsch, R. David, L. K. Verheij, and R. Franchy, Phys. Rev. B **63**, 125414 (2001), URL http://link.aps.org/doi/10.1103/PhysRevB.63.125414.

[60] M. Mayrhofer-Reinhartshuber, A. Tamtögl, P. Kraus, and W. E. Ernst, J. Phys.: Condens. Matter **25**, 395002 (2013), URL http://stacks.iop.org/0953-8984/25/i=39/a=395002.

[61] B. Poelsema, A. F. Becker, G. Rosenfeld, R. Kunkel, N. Nagel, L. K. Verheij, and G. Comsa, Surface Science **272**, 269 (1992), ISSN 0039-6028, URL http://www.sciencedirect.com/science/article/pii/003960289291449L.

[62] R. B. Doak, Ph.D. thesis, Massachusetts Institute of Technology (1981).

[63] M. I. Hernández, J. Campos-Martínez, S. Miret-Artés, and R. D. Coalson, Phys. Rev. B **49**, 8300 (1994), URL http://link.aps.org/doi/10.1103/PhysRevB.49.8300.

[64] S. Miret-Artés, Surface Science **366**, L735 (1996), ISSN 0039-6028, URL http://www.sciencedirect.com/science/article/pii/0039602896009363.

[65] V. Celli, *Helium Atom Scattering from Surfaces* (Springer, 1992).

[66] H. Hoinkes and H. Wilsch, *Helium Atom Scattering from Surfaces* (Springer, 1992).

[67] G. Brusdeylins, R. B. Doak, and J. P. Toennies, The Journal of Chemical Physics **75**, 1784 (1981), URL http://link.aip.org/link/?JCP/75/1784/1.

[68] G. Lilienkamp and J. P. Toennies, The Journal of Chemical Physics **78**, 5210 (1983), URL http://link.aip.org/link/?JCP/78/5210/1.

[69] D. J. Riley, A. P. Jardine, S. Dworski, G. Alexandrowicz, P. Fouquet, J. Ellis, and W. Allison, The Journal of Chemical Physics **126**, 104702 (2007), URL http://scitation.aip.org/content/aip/journal/jcp/126/10/10.1063/1.2464087.

[70] M. Vargas and W. Mochán, Surface Science **355**, 115 (1996), ISSN 0039-6028, URL http://www.sciencedirect.com/science/article/pii/0039602895013679.

[71] M. Vargas and W. Mochán, Surface Science **409**, 130 (1998), ISSN 0039-6028, URL http://www.sciencedirect.com/science/article/pii/S0039602898002921.

[72] V. Celli, N. Garcia, and J. Hutchison, Surface Science **87**, 112 (1979), ISSN 0039-6028, URL http://www.sciencedirect.com/science/article/pii/0039602879901730.

[73] A. A. Maradudin, E. W. Montroll, and G. H. Weiss, *Solid State Physics* (Academic, New York, 1963), chap. III. Theory of Lattice Dynamics in the Harmonic Approximation, p. chapter III.

[74] G. Benedek, Phys. Rev. Lett. **35**, 234 (1975), URL http://link.aps.org/doi/10.1103/PhysRevLett.35.234.

[75] M. Mayrhofer-Reinhartshuber, Master's thesis, Graz University of Technology (2010).

[76] A. Tamtögl, M. Mayrhofer-Reinhartshuber, P. Kraus, and W. E. Ernst, Surface Science **617**, 225 (2013), ISSN 0039-6028, URL http://www.sciencedirect.com/science/article/pii/S0039602813002252.

[77] T. A. S. Foundation, *Apache http server project*, http://httpd.apache.org/ (2013), URL http://httpd.apache.org/.

[78] Y. M. Koroteev, G. Bihlmayer, J. E. Gayone, E. V. Chulkov, S. Blügel, P. M. Echenique, and P. Hofmann, Phys. Rev. Lett. **93**, 046403 (2004), URL http://link.aps.org/doi/10.1103/PhysRevLett.93.046403.

[79] T. Kadono, K. Miyamoto, R. Nishimura, K. Kanomaru, S. Qiao, K. Shimada, H. Namatame, A. Kimura, and M. Taniguchi, Applied Physics Letters **93**, 252107 (2008), ISSN 0003-6951.

[80] P. Hofmann, Progress in Surface Science **81**, 191 (2006), ISSN 0079-6816, URL http://www.sciencedirect.com/science/article/pii/S0079681606000232.

[81] B. Weitzel and H. Micklitz, Phys. Rev. Lett. **66**, 385 (1991), URL http://dx.doi.org/0.1103/PhysRevLett.66.385.

[82] F. Muntyanu, A. Gilewski, K. Nenkov, A. Zaleski, and V. Chistol, Solid State Commun. **147**, 183 (2008), ISSN 0038-1098, URL http://dx.doi.org/10.1016/j.ssc.2008.05.024.

[83] F.-C. Chuang, C.-H. Hsu, C.-Y. Chen, Z.-Q. Huang, V. Ozolins, H. Lin, and A. Bansil, Applied Physics Letters **102**, 022424 (2013), URL http://ieeexplore.ieee.org/xpl/freeabs_all.jsp?arnumber=6415513&abstractAccess=no&userType=inst.

[84] P. Zhang, Z. Liu, W. Duan, F. Liu, and J. Wu, Phys. Rev. B **85**, 201410 (2012), URL http://link.aps.org/doi/10.1103/PhysRevB.85.201410.

[85] D. Hsieh, Y. Xia, L. Wray, D. Qian, A. Pal, J. H. Dil, J. Osterwalder, F. Meier, G. Bihlmayer, C. L. Kane, et al., Science **323**, 919 (2009), http://www.sciencemag.org/content/323/5916/919.full.pdf, URL http://www.sciencemag.org/content/323/5916/919.abstract.

[86] D. Hsieh, L. Wray, D. Qian, Y. Xia, J. H. Dil, F. Meier, L. Patthey, J. Osterwalder, G. Bihlmayer, Y. S. Hor, et al., New J. Phys. **12**, 125001 (2010), URL http://stacks.iop.org/1367-2630/12/i=12/a=125001.

[87] W. H. Bragg and W. L. Bragg, *X-rays and Crystal Structure* (G. Bell and Sons, London, 1915).

[88] R. James and N. Tunstall, Philosophical Magazine Series 6 **40**, 233 (1920), http://www.tandfonline.com/doi/pdf/10.1080/14786440808636119, URL http://www.tandfonline.com/doi/abs/10.1080/14786440808636119.

[89] A. Ogg, Philosophical Magazine Series 6 **42**, 163 (1921), http://www.tandfonline.com/doi/pdf/10.1080/14786442108633744, URL http://www.tandfonline.com/doi/abs/10.1080/14786442108633744.

[90] E. R. Jette and F. Foote, The Journal of Chemical Physics **3**, 605 (1935), URL http://link.aip.org/link/?JCP/3/605/1.

[91] C. S. Barrett, P. Cucka, and K. Haefner, Acta Crystallographica **16**, 451 (1963), URL http://dx.doi.org/10.1107/S0365110X63001262.

[92] D. Schiferl and C. S. Barrett, Journal of Applied Crystallography **2**, 30 (1969), URL http://dx.doi.org/10.1107/S0021889869006443.

[93] B. Stegemann, C. Ritter, B. Kaiser, and K. Rademann, Phys. Rev. B **69**, 155432 (2004), URL http://link.aps.org/doi/10.1103/PhysRevB.69.155432.

[94] D. Campi, M. Bernasconi, and G. Benedek, Phys. Rev. B **86**, 245403 (2012), URL http://link.aps.org/doi/10.1103/PhysRevB.86.245403.

[95] S. Bengió, J. Wells, T. Kim, G. Zampieri, L. Petaccia, S. Lizzit, and P. Hofmann, Surface Science **601**, 2908 (2007), ISSN 0039-6028, URL http://www.sciencedirect.com/science/article/pii/S0039602807004992.

[96] F. Jona, Surface Science **8**, 57 (1967), ISSN 0039-6028, URL http://www.sciencedirect.com/science/article/pii/0039602867900738.

[97] K. Sugawara, T. Sato, S. Souma, T. Takahashi, M. Arai, and T. Sasaki, Phys. Rev. Lett. **96**, 046411 (2006), URL http://link.aps.org/doi/10.1103/PhysRevLett.96.046411.

[98] H. Höchst and C. R. Ast, Journal of Electron Spectroscopy and Related Phenomena **137-140**, 441 (2004), ISSN 0368-2048, iCESS-9 Proceedings of the 9th International Conference on Electronic Spectroscopy and Structure, URL http://www.sciencedirect.com/science/article/pii/S0368204804000714.

[99] K. Sugawara, T. Sato, S. Souma, T. Takahashi, M. Arai, and T. Sasaki, Journal of Magnetism and Magnetic Materials **310**, 2177 (2007), ISSN 0304-8853, URL http://www.sciencedirect.com/science/article/pii/S0304885306024693.

[100] J. Shan, A. Chakradhar, Z. Yu, and U. Burghaus, Chemical Physics Letters **517**, 46 (2011), ISSN 0009-2614, URL http://www.sciencedirect.com/science/article/pii/S0009261411012802.

[101] P. W. Palmberg, G. E. Riach, R. E. Weber, and R. E. MacDonald, *Handbook of Auger Electron Spectroscopy* (Physical Electronics Industries, Inc., Edina, Minnesota, 1975), 3rd ed.

[102] M. Crystals and O. Ltd, *Antimony and bismuth crystal properties*, http://www.metal-crystals.com (2013), URL http://www.metal-crystals.com.

[103] H. Mönig, J. Sun, Y. M. Koroteev, G. Bihlmayer, J. Wells, E. V. Chulkov, K. Pohl, and P. Hofmann, Phys. Rev. B **72**, 085410 (2005), URL http://link.aps.org/doi/10.1103/PhysRevB.72.085410.

[104] K. Behnia, Science **321**, 497 (2008), http://www.sciencemag.org/content/321/5888/497.full.pdf, URL http://www.sciencemag.org/content/321/5888/497.short.

[105] C. R. Ast and H. Höchst, Phys. Rev. Lett. **87**, 177602 (2001), URL http://link.aps.org/doi/10.1103/PhysRevLett.87.177602.

[106] M. Hengsberger, P. Segovia, M. Garnier, D. Purdie, and Y. Baer, Eur. Phys. J. B **17**, 603 (2000), URL http://dx.doi.org/10.1007/s100510070097.

[107] F. Patthey, W.-D. Schneider, and H. Micklitz, Phys. Rev. B **49**, 11293 (1994), URL http://dx.doi.org/10.1103/PhysRevB.49.11293.

[108] C. Vossloh, M. Holdenried, and H. Micklitz, Phys. Rev. B **58**, 12422 (1998), URL http://link.aps.org/doi/10.1103/PhysRevB.58.12422.

[109] M. Tian, N. Kumar, M. H. W. Chan, and T. E. Mallouk, Phys. Rev. B **78**, 045417 (2008), URL http://dx.doi.org/10.1103/PhysRevB.78.045417.

[110] J. P. Toennies, J. Phys.: Condens. Matter **5**, A25 (1993), URL http://stacks.iop.org/0953-8984/5/i=33A/a=003.

[111] C. R. Ast and H. Höchst, Phys. Rev. B **70**, 245122 (2004), URL http://dx.doi.org/10.1103/PhysRevB.70.245122.

[112] C. R. Ast and H. Höchst, Phys. Rev. B **67**, 113102 (2003), URL http://dx.doi.org/10.1103/PhysRevB.67.113102.

[113] G. Jezequel, J. Thomas, and I. Pollini, Phys. Rev. B **56**, 6620 (1997), URL http://dx.doi.org/10.1103/PhysRevB.56.6620.

[114] G. Jezequel, Y. Petroff, R. Pinchaux, and F. Yndurain, Phys. Rev. B **33**, 4352 (1986), URL http://dx.doi.org/10.1103/PhysRevB.33.4352.

[115] C. Wöll and A. M. Lahee, *Helium Atom Scattering from Surfaces* (Springer, 1992).

[116] G. Comsa, Surf. Sci. **81**, 57 (1979), ISSN 0039-6028, URL http://www.sciencedirect.com/science/article/pii/0039602879905053.

[117] J. Lapujoulade, Y. Lejay, and G. Armand, Surf. Sci. **95**, 107 (1980), ISSN 0039-6028, URL http://www.sciencedirect.com/science/article/pii/0039602880901314.

[118] N. Esbjerg and J. K. Nørskov, Phys. Rev. Lett. **45**, 807 (1980), URL http://link.aps.org/doi/10.1103/PhysRevLett.45.807.

[119] J. Harris and A. Liebsch, J. Phys. C **15**, 2275 (1982), URL http://stacks.iop.org/0022-3719/15/i=10/a=027.

[120] R. M. Goodman and G. A. Somorjai, J. Chem. Phys. **52**, 6325 (1970), URL http://dx.doi.org/10.1063/1.1672946.

[121] K. G. Ramanathan and T. M. Srinivasan, Phys. Rev. **99**, 442 (1955), URL http://dx.doi.org/10.1103/PhysRev.99.442.

[122] F. van Delft, Surf. Sci. **251-252**, 690 (1991), ISSN 0039-6028, URL http://www.sciencedirect.com/science/article/pii/003960289191080H.

[123] D. Velic and R. J. Levis, Chem. Phys. Lett. **269**, 59 (1997), ISSN 0009-2614, URL http://www.sciencedirect.com/science/article/pii/S0009261497002509.

[124] E. K. Grimmelmann, J. C. Tully, and M. J. Cardillo, J. Chem. Phys. **72**, 1039 (1980), URL http://link.aip.org/link/?JCP/72/1039/1.

[125] S. Yaginuma and T. Nagao, Phys. Rev. B **82**, 045422 (2010).

[126] S. Yaginuma, T. Nagao, J. Sadowski, M. Saito, K. Nagaoka, Y. Fujikawa, T. Sakurai, and T. Nakayama, Surf. Sci. **601**, 3593 (2007), ISSN 0039-6028, URL http://www.sciencedirect.com/science/article/pii/S003960280700739X.

[127] J. Seo, P. Roushan, H. Beidenkopf, Y. S. Hor, and R. J. C. A. Yazdani, Nature **466**, 343 (2010).

[128] A. Narayan, I. Rungger, and S. Sanvito, Phys. Rev. B **86**, 201402 (2012), URL http://link.aps.org/doi/10.1103/PhysRevB.86.201402.

[129] G. Bian, X. Wang, Y. Liu, T. Miller, and T.-C. Chiang, Phys. Rev. Lett. **108**, 176401 (2012), URL http://link.aps.org/doi/10.1103/PhysRevLett.108.176401.

[130] V. Grozovski, S. Kallip, and E. Lust, Surface Science **613**, 108 (2013), ISSN 0039-6028, URL http://www.sciencedirect.com/science/article/pii/S003960281300112X.

[131] G. Boato, P. Cantini, and R. Tatarek, Phys. Rev. Lett. **40**, 887 (1978), URL http://link.aps.org/doi/10.1103/PhysRevLett.40.887.

[132] B. Borca, S. Barja, M. Garnica, M. Minniti, A. Politano, J. M. Rodriguez-García, J. J. Hinarejos, D. Farías, A. L. V. de Parga, and R. Miranda, New Journal of Physics **12**, 093018 (2010), URL http://stacks.iop.org/1367-2630/12/i=9/a=093018.

[133] A. Politano, B. Borca, M. Minniti, J. J. Hinarejos, A. L. Vázquez de Parga, D. Farías, and R. Miranda, Phys. Rev. B **84**, 035450 (2011), URL http://link.aps.org/doi/10.1103/PhysRevB.84.035450.

[134] I. Y. Sklyadneva, G. Benedek, E. V. Chulkov, P. M. Echenique, R. Heid, K.-P. Bohnen, and J. P. Toennies, Phys. Rev. Lett. **107**, 095502 (2011), URL http://link.aps.org/doi/10.1103/PhysRevLett.107.095502.

[135] M. Stiddard, Journal of Crystal Growth **51**, 394 (1981), ISSN 0022-0248, URL http://www.sciencedirect.com/science/article/pii/0022024881904164.

[136] A. Liebsch and J. Harris, Surface Science Letters **111**, L721 (1981), ISSN 0167-2584, URL http://www.sciencedirect.com/science/article/pii/0167258481905028.

[137] J. Perreau and J. Lapujoulade, Surface Science Letters **119**, L292 (1982), ISSN 0167-2584, URL http://www.sciencedirect.com/science/article/pii/0167258482906491.

[138] A. Luntz, L. Mattera, M. Rocca, S. Terreni, F. Tommasini, and U. Valbusa, Surface Science **126**, 695 (1983), ISSN 0039-6028, URL http://www.sciencedirect.com/science/article/pii/0039602883907768.

[139] M. Hernandez, O. Roncero, S. Miret-Artes, P. Villarreal, and G. Delgado-Barrio, The Journal of Chemical Physics **90**, 3823 (1989), URL http://link.aip.org/link/?JCP/90/3823/1.

[140] S. Miret-Artes, J. P. Toennies, and G. Witte, Phys. Rev. B **54**, 5881 (1996), URL http://link.aps.org/doi/10.1103/PhysRevB.54.5881.

[141] V. Celli, G. Benedek, U. Harten, J. Toennies, R. Doak, and V. Bortolani, Surface Science **143**, L376 (1984), ISSN 0039-6028, URL http://www.sciencedirect.com/science/article/pii/0039602884904023.

[142] V. Bortolani, A. Franchini, N. Garcia, F. Nizzoli, and G. Santoro, Phys. Rev. B **28**, 7358 (1983), URL http://link.aps.org/doi/10.1103/PhysRevB.28.7358.

[143] C. Nyeland and J. P. Toennies, Chemical Physics **321**, 285 (2006), ISSN 0301-0104, URL http://www.sciencedirect.com/science/article/pii/S0301010405003757.

[144] D. R. Miller, *Atomic and Molecular Beam Methods* (Oxford University Press, 1983), vol. 1, chap. 2, pp. 14–53.

[145] J. F. Annett and R. Haydock, Phys. Rev. Lett. **53**, 838 (1984), URL http://link.aps.org/doi/10.1103/PhysRevLett.53.838.

[146] K. H. Rieder, G. Parschau, and B. Burg, Phys. Rev. Lett. **71**, 1059 (1993), URL http://link.aps.org/doi/10.1103/PhysRevLett.71.1059.

[147] G. Boato, P. Cantini, C. Salvo, R. Tatarek, and S. Terreni, Surf. Sci. **114**, 485 (1982), ISSN 0039-6028, URL http://www.sciencedirect.com/science/article/pii/0039602882907002.

[148] G. Benedek, G. Brusdeylins, C. Heimlich, J. Toennies, and U. Valbusa, Surf. Sci. **178**, 545 (1986), ISSN 0039-6028, URL http://www.sciencedirect.com/science/article/pii/0039602886903316.

[149] G. Bracco, M. D. Ward, and G. Scoles, J. Chem. Phys. **118**, 8405 (2003), URL http://link.aip.org/link/?JCP/118/8405/1.

[150] J. Lapujoulade, J. Perreau, and A. Kara, Surf. Sci. **129**, 59 (1983), ISSN 0039-6028, URL http://www.sciencedirect.com/science/article/pii/0039602883900948.

[151] S. Daon, E. Pollak, and S. Miret-Artes, J. Chem. Phys. **137**, 201103 (pages 4) (2012), URL http://link.aip.org/link/?JCP/137/201103/1.

[152] B. Gumhalter, Surf. Sci. **347**, 237 (1996), ISSN 0039-6028, URL http://www.sciencedirect.com/science/article/pii/003960289500954X.

[153] A. Šiber and B. Gumhalter, Surface Science **385**, 270 (1997), ISSN 0039-6028, URL http://www.sciencedirect.com/science/article/pii/S0039602897001945.

[154] A. Levi and H. Suhl, Surf. Sci. **88**, 221 (1979), ISSN 0039-6028, URL http://www.sciencedirect.com/science/article/pii/0039602879905776.

[155] G. Benedek, M. Bernasconi, V. Chis, E. Chulkov, P. M. Echenique, B. Hellsing, and J. P. Toennies, J. Phys.: Condens. Matter **22**, 084020 (2010), URL http://stacks.iop.org/0953-8984/22/i=8/a=084020.

[156] S. Krishnaswamy, G. Derry, D. Wesner, T. O'Gorman, and D. Frankl, Surf. Sci. **77**, 493 (1978), ISSN 0039-6028, URL http://www.sciencedirect.com/science/article/pii/0039602878901358.

[157] G. Bian, T. Miller, and T.-C. Chiang, Phys. Rev. Lett. **107**, 036802 (2011), URL http://link.aps.org/doi/10.1103/PhysRevLett.107.036802.

[158] G. Benedek, P. M. Echenique, J. P. Toennies, and F. Traeger, J. Phys.: Condens. Matter **22**, 304016 (2010), ISSN 0953-8984, URL http://stacks.iop.org/0953-8984/22/i=30/a=304016.

[159] J. Kröger, Rep. Prog. Phys. **69**, 899 (2006), URL http://stacks.iop.org/0034-4885/69/i=4/a=R02.

[160] X. Zhu, L. Santos, R. Sankar, S. Chikara, C. . Howard, F. C. Chou, C. Chamon, and M. El-Batanouny, Phys. Rev. Lett. **107**, 186102 (2011), URL http://link.aps.org/doi/10.1103/PhysRevLett.107.186102.

[161] X. Zhu, L. Santos, C. Howard, R. Sankar, F. C. Chou, C. Chamon, and M. El-Batanouny, Phys. Rev. Lett. **108**, 185501 (2012), URL http://link.aps.org/doi/10.1103/PhysRevLett.108.185501.

[162] C. Howard, M. El-Batanouny, R. Sankar, and F. C. Chou, Phys. Rev. B **88**, 035402 (2013), URL http://link.aps.org/doi/10.1103/PhysRevB.88.035402.

[163] Armand, G. and Manson, J.R., J. Phys. France **44**, 473 (1983), URL http://dx.doi.org/10.1051/jphys:01983004404047300.

[164] P. M. Morse, Phys. Rev. **34**, 57 (1929), URL http://link.aps.org/doi/10.1103/PhysRev.34.57.

[165] M. Hernández, S. Miret-Artés, P. Villarreal, and G. Delgado-Barrio, Surface Science **251252**, 369 (1991), ISSN 0039-6028, URL http://www.sciencedirect.com/science/article/pii/003960289191016Q.

[166] R. Martínez-Casado, B. Meyer, S. Miret-Artés, F. Traeger, and C. Wöll, Journal of Physics: Condensed Matter **19**, 305006 (2007), URL http://stacks.iop.org/0953-8984/19/i=30/a=305006.

[167] P. Kraus, M. Mayrhofer-Reinhartshuber, A. Tamtögl, S. Miret-Artés, and W. E. Ernst (in preparation).